Photoluminescence of 2D and quasi-2D perovskites

Zur Erlangung des akademischen Grades

eines Doktors der Ingenieurwissenschaften (Dr.-Ing.)

von der KIT-Fakultät für Elektrotechnik und Informationstechnik
des Karlsruher Instituts für Technologie (KIT)

genehmigte
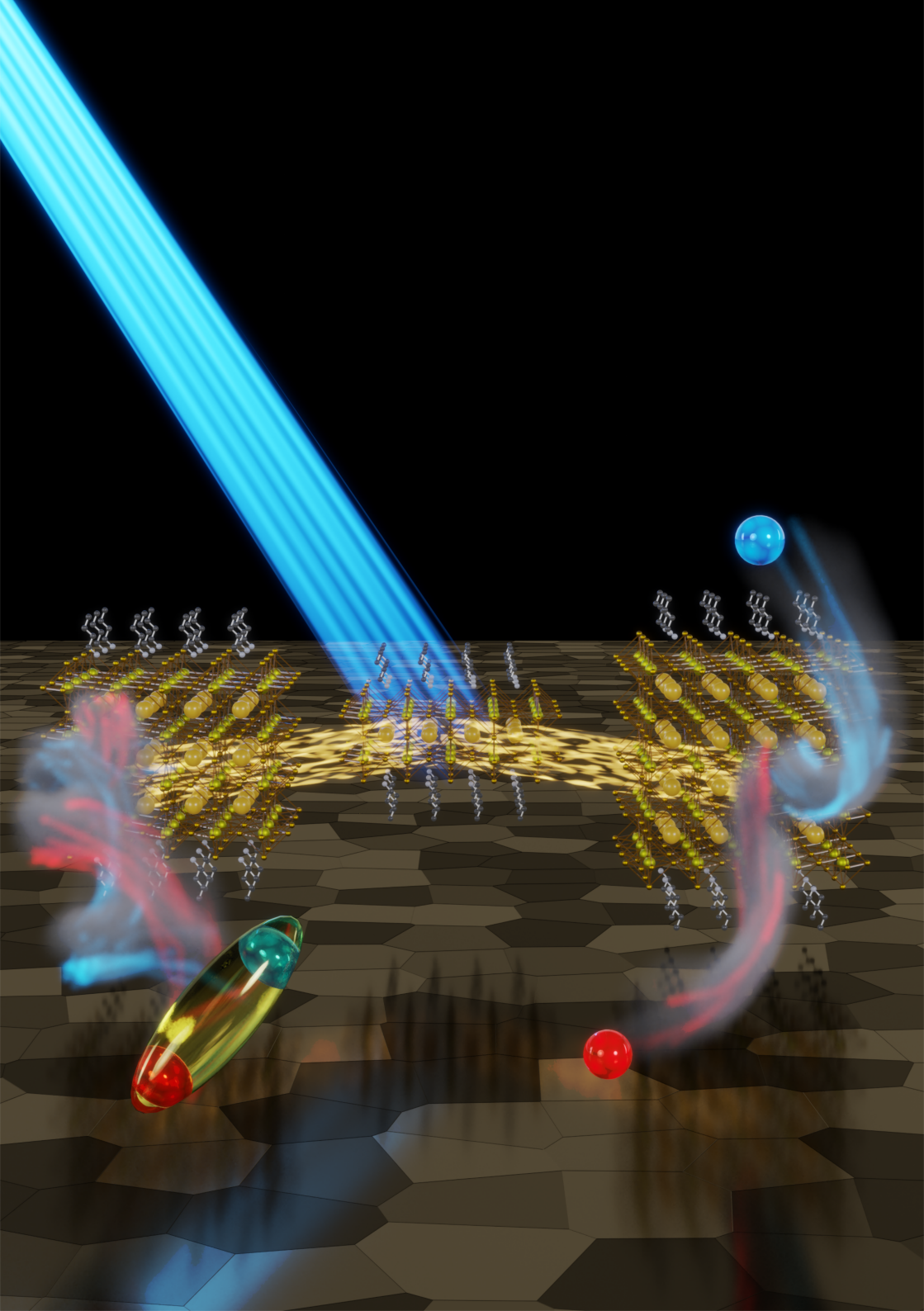
Dissertation

von

M. Sc. Milian Kaiser

"*No problem is too small or too trivial if we can really do something about it.*"

Richard P. Feynman

Contents

vi

Kurzfassung

In den letzten Jahren wurden Perowskite, insbesondere 2D- und Quasi-2D-Perowskite, in Bereichen wie Photovoltaik, Leuchtdioden und Lasertechnik intensiv erforscht. Diese Arbeit soll einen Einblick in die grundlegende Photophysik der angeregten Zustände dieser Materialien nach einer Anregung durch Laserlicht geben und als Anleitung zur Interpretation der emittierten Photolumineszenzspektren dienen. Zunächst werden reine 2D-Perowskite in der Ruddlesden-Popper-Phase unter Verwendung von Phenethylamin (PEA) als Spacermolekül (PEA_2PbI_4) und der Dion-Jacobson-Phase unter Verwendung von 1,4-Phenylendimethanamin bei verschiedenen Temperaturen und mit einer gepulsten und einer Dauerstrich-Laserquelle bei unterschiedlichen Anregungsintensitäten untersucht. Während bei beiden Materialien die exzitonische Emission bei allen gemessenen Temperaturen dominiert, werden für Temperaturen unterhalb von 140 K zusätzliche Peaks in den Emissionsspektren beobachtet. Im Ruddlesden-Popper-Material werden bei 5 K zwei Peaks mit einem Energieabstand von 40.3 meV beobachtet, wobei der Peak mit der höheren Energie den freien Exzitonen und der mit der niedrigeren Energie den gebundenen Exzitonen (gebunden durch ein Fehlstelle) zugeschrieben wird. Bei hohen Anregungsintensitäten dominiert die Emission der gebundenen Exzitonen die Gesamtemission. Dies ist darauf zurückzuführen, dass die Exziton-Exziton-Annihilierung die Emission der freien Exzitonen stark unterdrückt, während die Emission der gebundenen Exzitonen kaum beeinträchtigt wird. Dieser Effekt

x

ist im Dion-Jacobson-Perowskit weniger ausgeprägt. In beiden Materialien kann die Emission von PbI_2-Einschlüssen bei niedrigen Temperaturen beobachtet werden. Anschließend werden die Emissionseigenschaften verschiedener Quasi-2D-Materialien untersucht. Im Gegensatz zu 2D-Perowskiten, deren angeregte Zustände nur aus Exzitonen bestehen, zeigen Quasi-2D-Perowskite Emission von Exzitonen, freien Ladungsträgern oder sogar von beiden. Durch Analyse der zeitaufgelösten Photolumineszenz, der Quanteneffizienz und der anfänglichen Photonenemissionsdichte kann die Mischung der angeregten Zustände bestimmt werden. Die Emissionseffizienz von freien Ladungsträgern nimmt mit der Anregunsintensität zu, während die von Exzitonen abnimmt. Es wird ein einfaches Modell von zwei nicht wechselwirkenden Populationen von Exzitonen und Ladungsträgern in getrennten Teilvolumina des Films vorgestellt, das alle Beobachtungen in dieser Arbeit beschreibt. Die Emissionscharakteristiken hängen stark von dem in der Perowskitlösung verwendeten Spacer-Molekül und dessen Konzentration ab. Hohe Konzentrationen von Butylamin führen zu 100 % Emission von Exzitonen, die auf 7 % Exzitonenemission und 93 % freie Ladungsträgeremission bei Perowskiten mit niedrigen Konzentrationen von 1-Naphthylmethylamin Spacermolekülen zurückgeht. Schließlich wird auf der Grundlage dieser Beobachtungen eine Messtechnik eingeführt, bei der zwei Anregungspulse mit steuerbarer Verzögerung und ein USB-Spektrometer, das die zeitintegrierten Spektren aufzeichnet, verwendet werden, um die Geschwindigkeitskonstanten sowie den Anteil der Emission von Exzitonen und freien Ladungsträgern zu ermitteln. Diese Methode ist wesentlich schneller und kostengünstiger als herkömmliche Zeitaufgelöste-Messmethoden der Photolumineszenz. Die Robustheit und Schnelligkeit dieser Methode ist potenziell sehr interessant für den Einsatz in einer Fertigungslinie für photovoltaische 3D-Perowskit-Absorberschichten und ebnet so den Weg von der Forschung zur Anwendung.

Abstract

In recent years perovskites and in particular, 2D and quasi-2D perovskites have been a highly researched field in areas like photovoltaics, light-emitting diodes, and lasing. This thesis aims to provide insight into the fundamental photophysics of the excited states in these materials after excitation from a laser source as well as act as a guide to interpreting the emitted photoluminescence spectra. First, purely 2D perovskites in the Ruddlesden-Popper phase utilizing phenethylamine (PEA) as a spacer (PEA_2PbI_4) and in the Dion-Jacobson (DJ) phase utilizing 1,4-phenylenedimethanamine are investigated at different temperatures and with a pulsed and a continuous wave laser source at various excitation fluences. While both materials are dominated by excitonic emission at all temperatures measured, additional peaks are observed in the emission spectra at temperatures below $140\,K$. In the Ruddlesden-Popper material at $5\,K$, two peaks with an energy separation of $40.3\,meV$ are observed with the higher energy peak being ascribed to free excitons and the lower one to bound excitons (bound by a trap site). At high excitation fluences, the emissions from the bound excitons dominates the total emission. This is based on exciton-exciton annihilation strongly suppressing the emission from the free excitons and barely affecting the bound exciton emission. This effect is less pronounced in the Dion-Jacobson perovskite. In both materials emission from PbI_2-inclusions can be observed at low temperatures. Second, the emission characteristics of different quasi-2D materials are examined. Unlike in 2D perovskites where excited states only consist of excitons, quasi-2D perovskites show emission from excitons, free charge carriers, or even both. By analyzing the time-resolved photoluminescence,

the quantum efficiency and the initial photon emission density the mixture of excited states can be determined. The emission efficiency of free charge carriers increases with fluence while that for excitons decreases. A simple model of two non-interacting populations of excitons and charge carriers in separate sub-volumes of the film is introduced, which describes all made observations. The emission characteristics are highly dependent on the spacer molecule used in the perovskite precursor and on its concentration. High concentrations of butylamine lead to 100% emission from excitons which goes down to 7% excitons and 93% free carriers for perovskites made with low concentrations of 1-naphthylmethylamine spacer molecules. Lastly, based on these observations a measurement technique is introduced whereby two excitation pulses with a controllable delay and a USB spectrometer are used to record the time-integrated spectra which allows the extraction of the rate constants of the material as well as the fraction of excitonic and free carrier emission. This method is considerably faster and significantly cheaper than traditional time-resolved measurements. The robustness and speed of this technique are potentially very interesting for its use in a fabrication line for 3D-perovskite-based photovoltaic absorber films, thereby paving the pathway from research to application.

Acknowledgements

I would like to express my profound gratitude to Dr. Ian A. Howard for his guidance and support throughout this work. His creativity and vast knowledge of theoretical and experimental work led to consistently productive discussions. I would like to express my sincere gratitude to Dr. Yang Li without whose assistance and guidance in the preparation of materials, my publications and this thesis would not be possible. Along these lines, I would like to thank Prof. Dr. Bryce Richards and Tenure-Track-Prof. Dr. Ulrich Paetzold who used their great experience helping me improve my publications as well as my work as a scientist. I am very thankful for the productive work environment they created.

Furthermore, I would like to thank all my helpful colleagues. Especially Dr. Michael Adams and Dr. Marius Jakoby who introduced me to the laser system used in this work and were always happy to discuss ideas or experimental data which was a great motivator. I would furthermore like to thank Dr. Stephan Dottermusch and Dr. Dmitry Busko for their guidance and help with different optical setups. I am also grateful to my colleagues Sheying Li, Ngei Katumo, David Ritzer, Isabel Allgero and Vinay Kumar for the entertaining conversations and in some cases much welcome diversion. Additionally, I want to thank Dr. Nils Rosemann and Jan Christoph Fischer with whom I spent a lot of time in the lab fixing or trying to fix equipment which was always fun.

Ein besonderer Dank gilt meiner Familie. Insbesondere meinen Eltern Nada und Gagi, welche mich schon immer bedingungslos unterstützt haben und mir stets ein Vorbild waren. Auch meiner Frau Rebecca danke ich für ihre Unterstützung. Ohne sie hätte diese Arbeit kein einziges Komma.

List of Publications

Peer-Reviewed Journals

During the cause of this work three first author and four coauthor publications were accepted for publication in peer-reviewed scientific journals and are listed in the following. One first author and one coauthor publication have been accepted by peer-reviewed journals but are still due to be published.

First author publications

1. M. Kaiser, Y. Li, J. Schwenzer, M. Jakoby, I. Allegro, M. Gerhard, M. Koch, A. Ducinskas, B. S. Richards, M. Graetzel, J. V. Milić, U. W. Paetzold and I. A. Howard, "How free exciton-exciton annihilation lets bound exciton emission dominate the photoluminescence of 2d-perovskites under high-fluence pulsed excitation at cryogenic temperatures," *Journal of Applied Physics*, vol. 129, no. 12, p. 123101, 2021. [Online]. Available: https://doi.org/10.1063/5.0037800

2. M. Kaiser, Y. Li, I. Allegro, B. S. Richards, U. W. Paetzold, and I. A. Howard, "Interpreting the time-resolved photoluminescence of quasi-2d perovskites," *Advanced Materials Interfaces*, vol. 8, no. 24, p. 2101326, 2021. [Online]. Available: https://onlinelibrary.wiley.com/doi/abs/10.1002/admi.202101326

3. M. Kaiser, Y. Li, S. Gharibzadeh, B. S. Richards, U. W. Paetzold, and I. A. Howard, "Charge carrier and exciton dynamics in

perovskites revealed by time-integrated photoluminescence after double-pulse excitation," *Advanced Materials Technologies* (accepted)

Co-author publications

4. Y. Li, I. Allegro, <u>M. Kaiser</u>, A. J. Malla, B. S. Richards, U. Lemmer, U. W. Paetzold, and I. A. Howard, "Exciton versus free carrier emission: Implications for photoluminescence efficiency and amplified spontaneous emission thresholds in quasi-2D and 3D perovskites," *Materials Today*, vol. 49, pp. 35-47, 2021. [Online]. Available: https://www.sciencedirect.com/ science/article/pii/S1369702121001619

5. N. Kiseleva, M. A. Filatov, J. C. Fischer, <u>M. Kaiser</u>, M. Jakoby, D. Busko, I. A. Howard, B. S. Richards and A. Turshatov, "BODIPY–pyrene donor–acceptor sensitizers for triplet–triplet annihilation upconversion: the impact of the BODIPY-core on upconversion efficiency," *Phys. Chem. Chem. Phys.*, vol. 24, no. 6, pp. 3568-3578, 2022. [Online]. Available: http://dx.doi.org/10.1039/D1CP05382E

6. H. Hu, S. Moghadamzadeh, A. Raheleh, Y. Li, , <u>M. Kaiser</u>, J. C. Fischer, Q. Jin, J. Maibach, I. M. Hossain, U. W. Paetzold and B. Abdollahi Nejand, "Sn-Pb Mixed Perovskites with Fullerene-Derivative Interlayers for Efficient Four-Terminal All-Perovskite Tandem Solar Cells," *Advanced Functional Materials*, vol. 32, no. 12, p. 2107650, 2022. [Online]. Available: https://onlinelibrary.wiley.com/ doi/abs/10.1002/adfm.202107650

7. B. A. Nejand, D. B. Ritzer, H. Hu, F. Schackmar, S. Moghadamzadeh, T. Feeney, R. Singh, F. Laufer, R. Schmager, R. Azmi, M. Kaiser, T. Abzieher, S. Gharibzadeh, E. Ahlswede, U. Lemmer, B. S. Richards, and U. W. Paetzold, "Scalable Two-Terminal All-Perovskite Tandem Solar Modules with 19.1% Efficiency," *Nature Energy* (accepted)

1

Introduction

The worldwide energy demand is consistently growing not only due to a rise in the population but also to the economic growth in developing countries. The global energy demand in the year 2019 was approximately 170 PWh of which ∼80% were generated from fossil fuels [1]. The need for energy is expected to grow an additional 10% by 2030 [2]. Not only are fossil fuels a finite resource, but they also emit greenhouse gases which are associated with the rise in global temperature. This causes great harm to a multitude of ecosystems and is potentially detrimental to the living conditions of humanity. In the long run, there is no alternative to phasing out fossil fuels and replacing them with renewable energies.

Generating electricity via photovoltaics is one of the most widely used renewable energy sources, with the first solar cell being produced over 60 years ago [3]. Since solar cells can generate more energy than is required to produce them and since the lifetime of the sun, which coincides with the lifetime of earth, can be considered endless, these devices are highly desirable and may become the most important power source for humanity. By far most of the photovoltaic electricity generation is done via silicon solar cells. These devices are very efficient but do require a lot of energy to be produced due to the used method of chemical vapor deposition. It takes between one and a half and five years for a solar cell to generate as much energy as was needed to produce the solar

cell. For the energy transition of the world, this means a huge energy investment based on fossil fuels is necessary to produce silicon solar cells or a new technology requiring less energy to be produced needs to be found.

While silicon solar cells have been considered commercial standard for decades, three-dimensional organic-inorganic halide perovskites have gathered lots of attention due to the quick improvements in power conversion efficiency (PCE) in perovskite-based photovoltaic devices. From 2009 when $CH_3NH_3PbI_3$ was used as a sensitizer in a dye-sensitized solar cell the power conversion efficiency increased from 3.8% [4] to over 25% in less than 15 years [5]. This improvement over such a short time indicates a remarkable potential for the future of solar cells. It has been suggested that the levelized cost of electricity from perovskite solar cells could be up to 20% cheaper than silicon-based solar cells [6]. Despite the high PCE, there are still some major drawbacks that need to be overcome.

One of the biggest problems with 3D-perovskites is their instability in regards to moisture [7, 8], heat [9], voltage [10] and ultraviolet light exposure [11, 12]. While the properties of 3D-perovskites like the high absorption coefficient, long-range diffusion, and high charge carrier mobility also create interest in research areas like photodetectors [13, 14] and light-emitting diodes (LEDs) their instability is a big concern regarding integration in long-living devices [15, 16]. This challenge still needs to be overcome; however, vast improvements have been made in recent years leading to solar cells being stable for over a year by 2D/3D interface engineering as shown by Grancini et al. [17]. While the efficiency, in this case, was only at 11.2%, solar cells from Jang et al. employing 2D/3D heterostructures have reached efficiencies of over 22% for over 1000 h under various conditions already [18]. Lin et al. showed all-perovskite tandem solar cells reaching 26.4% efficiency, retaining

90% of that after 600 h of illumination with one sun. The quasi-2D material hereby mostly acts as a passivation layer rather than absorbing light itself. For comparison, the efficiency of commercially available silicon solar cells lies at approximately 18%. These devices lose about 1% of their initial efficiency per year and are therefore much more stable than perovskites at the moment. Further improvements may lie in understanding the photophysics of 2D and quasi-2D perovskites.

2D perovskites are much more stable than their 3D relatives but also have a considerably lower PCE [19–21]. While the research on purely 2D perovskites has as of yet not led to similar improvements as for the 3D perovskites, research on quasi-2D perovskites forming the in-between of 2D and 3D lead to a whole new world of potential for these materials. Layered quasi two-dimensional metal-halide perovskites consist of a variety of differently sized crystals acting as quantum wells. The sizes of these quantum wells affect their band gap energies [22, 23]. This leads to excited states being funneled towards the lowest band gap material [24].

Xing et al. showed that this funneling can lead to highly efficient blue color emission from the low band gap material of the film, which improves when the amount of thinner quantum wells can be minimized [25]. Kong et al. showed that smoothing the funneling pathway can further improve the emission efficiency of perovskite light-emitting diodes (PeLEDs) [26]. These astonishing findings of energy transfer between differently sized quantum wells led to a myriad of high impact publications in this field [27–30]. PeLEDs have reached external quantum efficiencies of over 20% emitting at 780 nm and over 15% at roughly 520 nm. This is quite low compared with commercially available LEDs; however, the vast possibilities of tuning the emission wavelengths, especially in the blue region, make PeLEDs highly interesting for future research.

A further interesting research field regarding perovskites is lasing. In 3D perovskites, lasing has been observed by Jia et al. but only at low temperatures of roughly 100 K. Again, quasi-2D perovskites may show more promise compared to their 3D counterpart. In 2020 Qin et al. were able to show continuous-wave lasing at room temperature in quasi-2D perovskite films [31]. They ascribe this emission to exciton recombination in the quantum wells. In this work, the probability of excitons being involved in the emission will be discussed. Since the emission occurs from the low band gap quantum wells, this means that similar to PeLEDs, perovskite lasing at a multitude of emission wavelengths might be possible in the near future.

2D and quasi-2D perovskites are furthermore interesting for applications due to their stability, color purity and high quantum efficiency [29, 32–42]. Despite the drastic improvements over the years the photophysics of 2D and quasi-perovskites 2D has not been fully understood yet. For the successful development of an ideal photovoltaic absorber material as well as for efficient PeLEDs, the photophysics and excited-state dynamics have to be analyzed. If the excited states and their recombination pathways are known, the potential improvements can be assessed. To further this understanding, measurement methods, as well as models describing the observations can be introduced as helpful tools. Kilifaridis et al. found that the enhancement of the photoluminescence quantum yield after excitation from a pulsed laser source depends on the power density of the laser pulse as well as on the repetition rate [43]. This is shown in **Figure 1.1**. Based on this observation they qualify widely used models describing the carrier dynamics like the ABC model and the Shockley-Read-Hall (SRH) model. They conclude that Auger trapping and recombination in combination with the SRH model best describe their findings. Due to the low exciton binding energy in the

used MAPbI$_3$ perovskite, they do not consider excitons in their modeling. The dependence on laser power and repetition rate results in curves not dissimilar to a horse's mane, which are used to identify the recombination pathways. Earlier work from Stranks et al. considers three states that describe the time-dependence of the photoluminescence after pulsed excitation, namely: traps, electrons, and excitons [44]. They found a strong dependence of the photoluminescence lifetime on the initial density of excited states which they can resolve with differential equations for each of the three states. D'Innocenzo et al. found that the involvement of excitons in the absorption process might be advantageous for solar cells as well as for other optoelectronic devices in 3D perovskites [45].
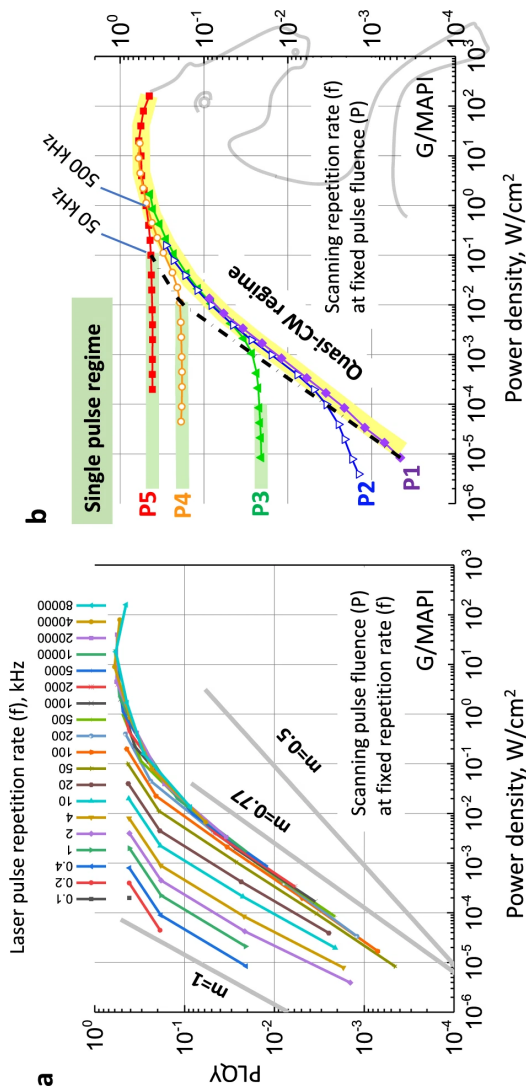
FIGURE 1.1 : a) PLQY(W) dependence plotted in the traditional way (P-scanning) for 19 different pulse repetition rates. The datapoints measured at the same frequency are connected by lines, the sample is MAPbI$_3$ film grown on glass (G/MAPI). The apparent slope of these dependencies (m, PLQY $\sim W^m$) depends on the range of W and the value of f and can be anything from 1 to 0.77 for this particular sample. b) The same data plotted in the form of a PLQY(f, P) map where data points measured at the same pulse energy ($P1$, $P2$, ..., $P5$) are connected by lines (f-scanning). Data points measured at 50 kHz frequencies are connected by a dashed-dotted line. Adapted from Kiligaridis et al. [43].

For quasi-2D perovskites, Spitha et al. discovered that both exciton and free charge carrier characteristics could be found in the emission after pulsed excitation. While they ascribe the emission solely to excitons the dissociation into carriers and reformation by carriers is sufficient to describe their experimental findings [46]. In contrast, Li et al. found that emission either happens via exciton or free charge carrier recombination depending on the molecules used in the quasi-2D perovskite films [47]. There is a variety of models describing excited-state dynamics. If the wrong model is applied to assess the material quality, no reliable predictions about potential improvements and applications can be made. This work aims to provide insight into the excited states within these materials with both experimental data and theoretical simulations and considerations. Fast effects on the picosecond scale like hot carrier cooling as described by Hopper et al. are not considered [48]. The results of this work give insight into the recombination pathways of excited states in 2D and quasi-2D perovskites and enable the assessment of which research strategies are advantageous in the respective applications.

This thesis is organized as follows:

- **Chapter 2:** A brief introduction of the material and its structure, as well as the characteristics of the excited states and their dynamics.

- **Chapter 3:** An introduction to the equipment and methods that are used to measure the experimental data and the fabrication steps that are taken to produce the material.

- **Chapter 4:** Examination of the photoluminescence characteristics of purely 2D perovskites based on temperature and excitation fluence from different laser sources.

- **Chapter 5:** Investigation of the photoluminescence of different quasi-2D perovskites based on the concentration of spacer molecules. A model of the time-dependent excited-state recombination is introduced and discussed.

- **Chapter 6:** Based on the results of the previous chapter a measurement technique is discussed and shown to pose significant advantages in the characterization of photoluminescence compared with more traditional methods.

- **Chapter 7:** The findings of this work are summarized and an outlook for the future is presented.

2

Theoretical background

Semiconductors are materials based between metals and insulators. While metals are always conductive, semiconductors are not conductive at 0 K due to the separation of the valence band and the conduction band by the so-called band gap. At higher temperatures, charge carriers can be excited from the valence band to the conduction band and the material becomes conductive. For high band gaps, the material does not become conductive even at high temperatures and is therefore considered an insulator. There is no clear cutoff between semiconductors and insulators.

2.1 Excited states

In semiconductor materials, the absorption of photons in a specific energy range higher than the band gap leads to the creation of excited states. These states consist of either a bound charge-free electron-hole pair—so-called exciton—or a free electron and a free hole that can move independently from each other through the material—so-called free charge carriers—as depicted in **Figure 2.1**. The negatively charged electron and the positively charged hole attract each other via their coulombic potentials, meaning they are bound by the exciton binding energy. This energy would need to be overcome for the two carriers to dissociate. If the temperature of the material is low, excitons are likely
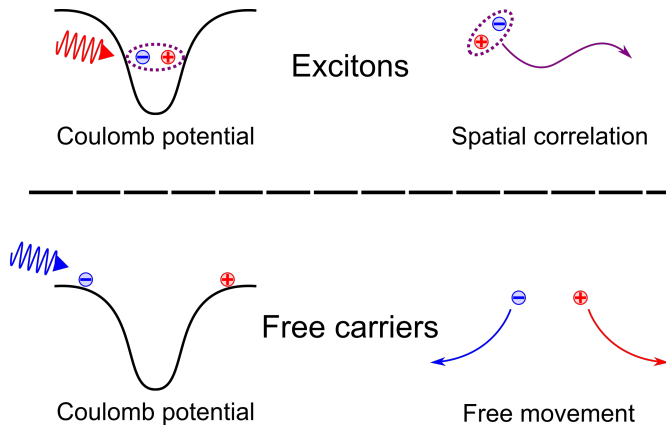
FIGURE 2.1: Schematic illustration of the differences between excitons and free charge carriers

to dominate the excited species while higher temperatures rather lead to free charge carriers being dominant. It is thereby possible to excite excitons with photons whose energy is slightly below the band gap energy. This is not possible for free charge carriers.

Both the free charge carriers and the excitons can recombine either radiatively or nonradiatively and thereby return to their ground state. The characteristics of the light emission and its time dependence can be used to distinguish the two species. In this section, the excited states are introduced and their characteristics in their light emission are explained.

2.1.1 Excitons

The binding energy of excitons depends on how far the involved charges can spatially separate. Strong coulombic interaction between
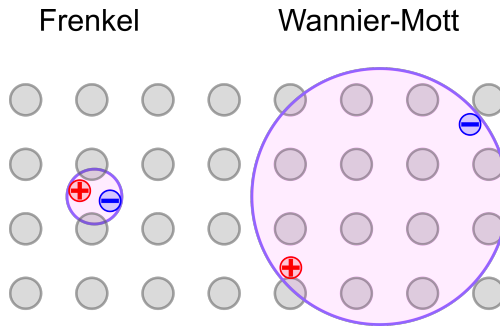
FIGURE 2.2: Schematic illustration of Frenkel and Wannier-Mott excitons

the charges leads to high binding energies and results in those charges being very close to each other. Such excitons are called Frenkel excitons and are the typical excited state species in organic semiconductors. In materials with high dielectric constants as with traditional semiconductors like silicon, the electric fields of the charges are affected by electric field screening which reduces the binding energy and allows higher spatial separation. Excitons with low binding energy and a high radius are called Wannier-Mott excitons. The difference between the two is shown in **Figure 2.2**.

A further influence on the exciton formation is the dimensionality of the material. Quantum confinement can reduce the possibilities for the electron-hole pair to spatially separate [23,49–51]. This can lead to high exciton binding energies due to the spatial confinement and the lack of electric field screening.

Excitons recombine either radiatively or nonradiatively. The recombination rate is thereby proportional to the current density of excitons and can be described by:
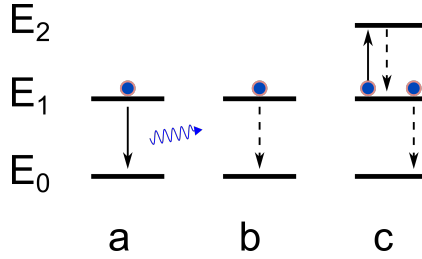
FIGURE 2.3: Exciton recombination pathways: a) radiative, b) nonra-
diative and c) exciton-exciton annihilation (EEA)

$$\frac{dn_x}{dt} = N_0 - k_{x,rad}n_x - k_{x,nrad}n_x, \qquad (2.1)$$

where n_x is the density of excitons with N_0 being the initial density. The
rates $k_{x,rad}$ and $k_{x,nrad}$ are the radiative and the nonradiative rates, respec-
tively. This linear dependence on the density is called monomolecular
recombination. For high exciton densities, two excitons can interact in
a way that one exciton recombines while the other is excited to a higher
state. From this state it relaxes back to the prior excited state, therefore
effectively only one exciton recombines, nonradiatively at that. This is a
form of recombination called Auger-recombination or more specifically
exciton-exciton annihilation (Exciton-Exciton Annihilation (EEA)) and
is illustrated in **Figure 2.3**.

While there are further recombination pathways like biexcitons [52, 53]
and triexcitons [54], the high fluences necessary to observe these phe-
nomenons surpass the fluences used in this work. The exciton density
considering EEA can be described by :

$$\frac{dn_x}{dt} = N_0 - k_x n_x - \gamma_{EEA}(t)n_x^2 \qquad (2.2)$$

a

b
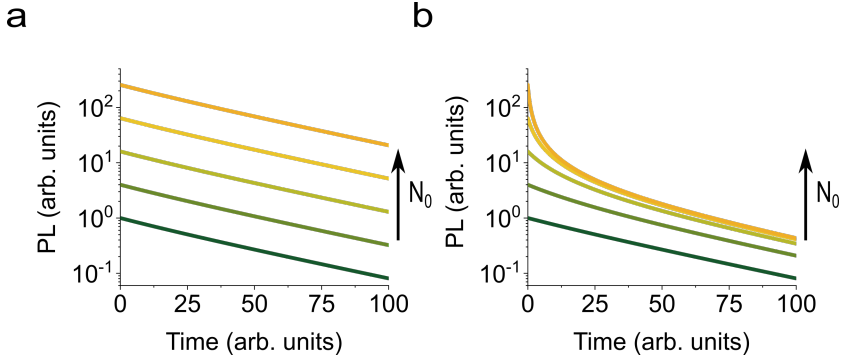
FIGURE 2.4: Differences of the time-resolved photoluminescence a) without exciton-exciton annihilation and b) with exciton-exciton annihilation. The used rates are arbitary and the initial density is increased by a factor of four for each curve.

where γ_{EEA} is the EEA rate and k_x is the combined monomolecular recombination rate. In 2D, quasi-2D and 3D systems excitons can diffuse without constraint, and $\gamma_{EEA}(t)$ is not time-dependent. This dependence of the EEA on the square of the exciton density makes EEA a bimolecular recombination pathway. The clear influence of EEA on the photoluminescence and its lifetime is shown in **Figure 2.4**. The initial emission rate in both cases is perfectly linear and is unaffected by EEA. The lifetime without the effect of EEA does not change with the fluence resulting in a linear curve on a semi-log scale indicating exponential recombination. If EEA does affect the recombination, the curve is linear for low initial densities but greatly reduces as the initial density increases. The quadratic dependence of the EEA on the density means that curves with low initial densities are barely affected with the effect quickly becoming dominant once the initial densities become high enough.

2.1.2 Free charge carriers

When the exciton binding energies are low and temperatures are high
enough, excitons can dissociate into free charge carriers. In semicon-
ductor materials, excitons and free charge carriers form a temperature-
dependent equilibrium which can be described by the Saha equation
[55, 56]. The Saha-equation for semiconductors depends mainly on the
temperature T, the exciton binding energy E_b, and the excited-state den-
sity N. For 3D semiconductors, the fraction of excited states that consist
of electrons x is given by:

$$\frac{x^2}{1-x} = \frac{1}{N}\left(\frac{2\pi\mu k_B T}{h^2}\right)^{\frac{3}{2}} exp\left(-\frac{E_B}{k_B T}\right) \qquad (2.3)$$

where μ is the reduced mass, k_B is the Boltzmann constant and h is
the Planck constant. This equation shows how the equilibrium shifts
towards free carriers for high temperatures, low excited-state densities,
and low exciton binding energies. While this equation generally holds,
it is difficult to apply in real applications as other effects like trapping in-
crease the complexity of the system. It is therefore, necessary to analyze
the emission spectra as well as the Time-Resolved Photoluminescence
(TRPL) to estimate if the Saha equation is applicable. This is particu-
larly true in the case of perovskite materials, where this poses a chal-
lenging task. The recombination pathways of free carriers are often de-
scribed by a rate constant model involving the rates for monomolecular
recombination due to trapping (k_1), bimolecular radiative recombination
(k_2), and Auger recombination (k_3). This is sometimes also called ABC
model. A schematic of the recombination pathways is shown in **Figure
2.5**.
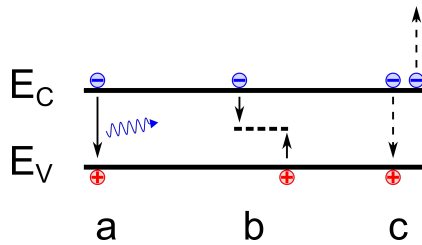
FIGURE 2.5: Free charge carrier recombination pathways: a) radiative (bimolecular), b) nonradiative Shockley-Read-Hall recombination involving a trap state inside the band gap and c) Auger recombination. E_C is the conduction band and E_V is the valence band energy.

The recombination probability of the radiative recombination is dependent on the probability of an electron and a hole meeting which is proportional to the density of electrons timed with the density of holes. In an intrinsic semiconductor where the density of both charge carriers is the same, the radiative recombination rate is dependent on the square of the charge carrier density and is similar to EEA a bimolecular recombination pathway. The Shockley-Read-Hall recombination is due to charge carriers being trapped by states inside the band gap from where they recombine nonradiatively. The likelihood of a carrier being trapped is dependent on the trap density—which typically does not depend on the carrier density—and the carrier density itself resulting in a linear dependence on the carrier density making it a monomolecular pathway. The Auger process for carriers involves either two holes and one electron or two electrons and one hole whereby two carriers of opposite charge recombine and the energy is transferred to the third carrier. This is also a nonradiative pathway that typically only becomes noticeable at high carrier densities. In this thesis, no clear signs of Auger recombination at the excitation intensities used were observed. The charge carrier

a

b
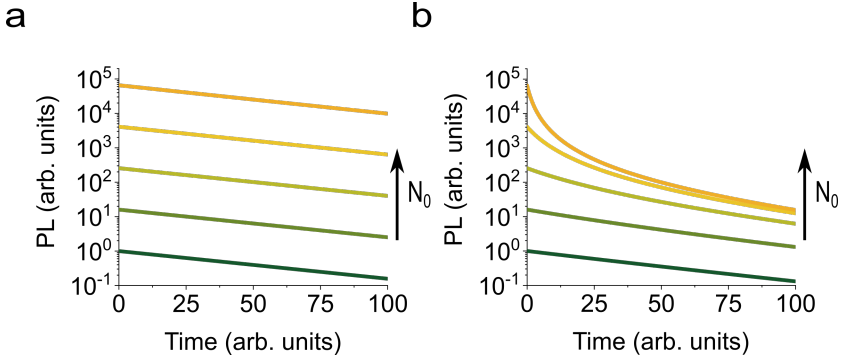
FIGURE 2.6: Differences of the time-resolved photoluminescence a) with strong trapping and weak radiative recombination and b) with strong radiative recombination. The used rates are arbitrary and the initial density is increased by a factor of four for each curve.

density can be given by:

$$\frac{dn_c}{dt} = N_0 - k_{1,c}n_c - k_{2,c}n_c^2 \tag{2.4}$$

where $k_{1,c}$ is the monomolecular rate, $k_{2,c}$ is the bimolecular rate and n_c is the charge carrier density. This equation is very similar to the exciton case, however, the radiative portion is now bimolecular and the nonradiative portion is monomolecular. Typical TRPL for weak and strong radiative recombinations are shown in **Figure 2.6**.

At first glance the TRPL of free carriers and excitons look very similar, however, the initial radiative rate of free carriers is increasing with the square of the initial density and not linearly as in the exciton case. When the radiative recombination pathway becomes dominant, the lifetime starts to decrease. The fast increase in the initial rate and the reduction in lifetime lead to a flash of photons with high intensity.
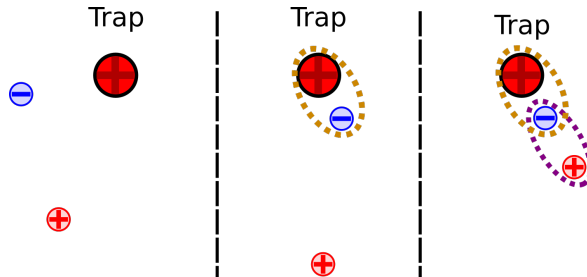
FIGURE 2.7: A charge carrier can bind to a trap site. From there a carrier with the opposite charge can bind to the first carrier resulting in a bound exciton.

2.1.3 Bound excitons

Additionally to the excited states introduced above, there are some states which are only well observable at low temperatures. One of these states is bound excitons. For a bound exciton, a charge carrier becomes trapped by a crystal defect. This carrier then traps a carrier of the opposite charge to itself. The result is a trapped exciton that is incapable of moving through the crystal and bound by a specific energy. This typically low energy has to be overcome for the exciton to be freed. In perovskites, room temperature is typically enough for bound excitons to be freed which is why they are only observable at low temperatures. Similar to bound excitons, excitons can also be trapped by crystal disorder leading to low band gap regions. Excitons bound to such a region are called localized excitons and are typically bound by smaller energy compared to bound excitons. The mechanism by which excitons are bound is depicted in **Figure 2.7**.
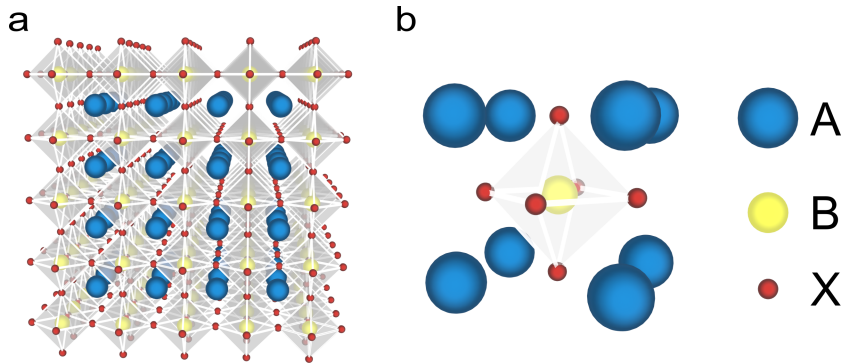
FIGURE 2.8: a) Crystal structure and b) unit cell of a 3D perovskite with the monovalent cation A, the divalent cation B, and the halide anion X

2.2 Perovskite crystal structure

A very interesting group of semiconductors in recent years are called halide perovskites. They are named after the russian mineralogist Lev Perovski and originally represented a calcium titanium oxide ($CaTiO_3$) mineral. Later on, compounds with similar crystal structures were also called perovskites.

2.2.1 3D perovskites

The general chemical composition of 3D-perovskites is ABX_3. Here A is a monovalent cation that can be organic (e.g. methylammonium or formamidinium) or inorganic (e.g. cesium or rubidium). B is a divalent cation (e.g. lead) and X is a halide anion (e.g. bromide or iodide) [57]. The crystal structure is illustrated in **Figure 2.8**.

The stability of these materials is described by the Goldschmidt tolerance factor t:

$$t = \frac{R_A + R_B}{\sqrt{2}(R_A + R_B)} \tag{2.5}$$

where R_A, R_B, and R_X are the ionic radii of the respective ions. The perovskite is most stable when the structure reaches cubic symmetry and t is close to one. Generally, perovskites form for $0.8 < t < 1$ [58]. Given that most studied perovskites use Pb or Sn as the B-site cation and a halide on the X-site the A-site cation needs to be accordingly large. For most perovskites methylammonium (MA) [59, 60], formadinium (FA) [61, 62] or even a mixture of the two are used [63]. Large atoms like Cs which lead to fully inorganic perovskites can also be used and are the mainly used A-site cation in this work [64]. First-principle electronic structure calculations show that the valence band maximum of these structures consists of an antibonding state between the B-site s-orbitals and the X-site p-orbitals while the conduction band minimum consists of a nonbonding state between the B-site p-orbitals and the X-site p-orbitals [65].

The A-site cation mainly stabilizes the crystal structure. A change in the crystal structure by substituting A, B, or X with different atoms, changing the temperature, or applying pressure changes the orbital overlap and with that the band gap of the material. It is therefore important to keep phase transitions in these materials in mind. An increase in the overlap of the B-site s-orbitals and the X-site p-orbitals destabilizes the valence band raising its energy while the B-site p-orbitals and the X-site p-orbitals respond less strongly due to their poorer orbital overlap. Lattice contractions, therefore, decrease the band gap while octahedral tilt increases the band gap [66].

3D perovskites are a promising material for applications like solar cells due to their high absorption coefficient [67] and large charge carrier

diffusion length [68, 69]. Furthermore, solar cells have the potential to become a low-cost alternative to silicon if perovskites reach better stability [6, 70].

The stability of 3D perovskite structures and devices is influenced by a multitude of factors like humidity, UV light exposure, and heat. One of the biggest challenges for devices outside of a lab environment is moisture. Water can hydrate the perovskite and form hydrate phases [71, 72]. This process however is reversible and not solely responsible for degradation but only weakens the bonds. Moisture saturation in the perovskite leads to irreversible changes and therefore degradation [73]. In inorganic perovskites, moisture can lead to an unfavorable phase transition and also degrade the perovskite [74]. UV light can degrade a perovskite in combination with oxygen [75] but it is also possible that UV light introduces defects in the charge transport layers [11, 76]. Heating a perovskite above 85 °C can lead to its degradation [77] which might be connected to the grain boundaries inside the material [78]. There are plenty more factors influencing the stability of perovskites and perovskite devices that go beyond the scope of this work. A possible solution to some of these problems might be low-dimension perovskites.

2.2.2 2D perovskites

2D-perovskites have increased stability compared to their 3D counterparts [19, 79]. In 2D perovskites, the A-site cation is replaced by large spacer molecules separating individual perovskite sheets from each other. The hydrophobicity of these spacer molecules greatly improves the stability against moisture [80]. The separation of the atomically thin perovskite sheets leads to dielectric and quantum confinement. The quantum confinement leads to an increase in the material band gap [81]
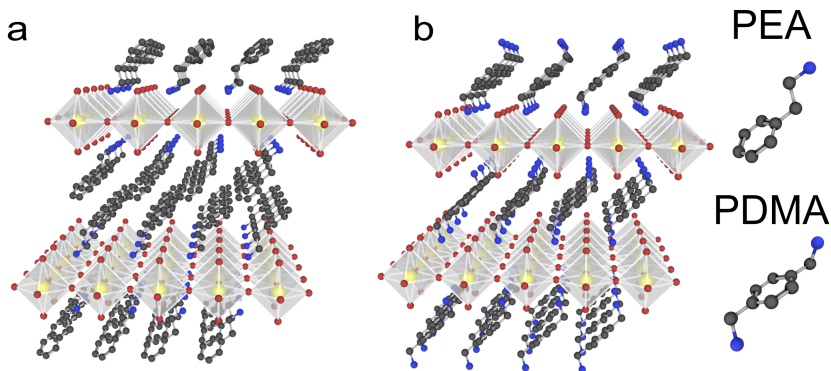
FIGURE 2.9: a) Ruddlesden-Popper and b) Dion-Jacobson phase 2D-perovskites illustrated with exemplary spacer molecules phenethylamine (Phenethylamine (PEA)) and 1,4-phenylenedimethanamine (PDMA)

while the dielectric confinement leads to an increase in the exciton binding energy [49, 82–84]. Additionally, the strong coulombic interaction leads to an increase in absorption [85]. There are mainly two types of 2D-perovskite phases: The Ruddlesden-Popper (RP) phase and the Dion-Jacobson (DJ) phase. The perovskite layers are either separated by two large monocationic spacer molecules (RP) or one dicationic spacer molecule per formula unit (DJ) as shown in **Figure 2.9**. The chemical formulas are: $A'_2 A_{n-1} B_n X_{3n+1}$ (RP) and $A'' A_{n-1} B_n X_{3n+1}$ (DJ). Here A' is the monocationic molecule and A'' is the dicationic molecule [86].

While the Dion-Jacobson might be advantageous for low band gap applications, the Ruddlesden-Popper seems to be more stable in ambient air condition [87]. While the increased stability compared to 3D perovskites makes 2D perovskites interesting, the high band gap makes them an unfavorable material for devices like solar cells and the low

photoluminescence quantum yield makes them unfavorable for PeLEDs [35]. To combine the desirable characteristics of both 2D and 3D perovskites quasi-2D perovskites become interesting.

2.2.3 Quasi-2D perovskites

Quasi-2D perovskites are more stable than 3D perovskites while showing higher photoluminescence quantum yields than 2D perovskites. They have the structure formula $L_2(ABX_3)_{n-1}BX_4$, where L is a large organic cation and n is the number of layers between the spacer molecules. For quasi-2D perovskites n>1, as displayed in **Figure 2.10**. Typically quasi-2D perovskites are not phase-pure, i.e. there is a distribution of differently sized quantum wells inside the film. The quantum, as well as the dielectric confinement depends on the thickness of the quantum well with thicker quantum wells having lower band gap energies as well as lower exciton binding energies [23, 49]. The high absorption coefficient of thin quantum wells means for excitations far above the band gap energy absorption in thin quantum wells should dominate. The excited species then move towards lower energy band gap material where they recombine i.e. the excited species funnel towards the thickest quantum wells [24, 33–35].

This funneling process does not happen in 2D- or 3D-perovskites and therefore makes quasi-2D perovskites a very interesting research topic.

2.2.4 Perovskite solar cells

In this work, the characteristics and the potential use of different materials in solar cells are discussed. Perovskite solar cells are p-i-n (n-i-p) junctions consisting of a hole transport layer (HTL, p-type), an electron transport layer (ETL, n-type), and a metal halide perovskite as an
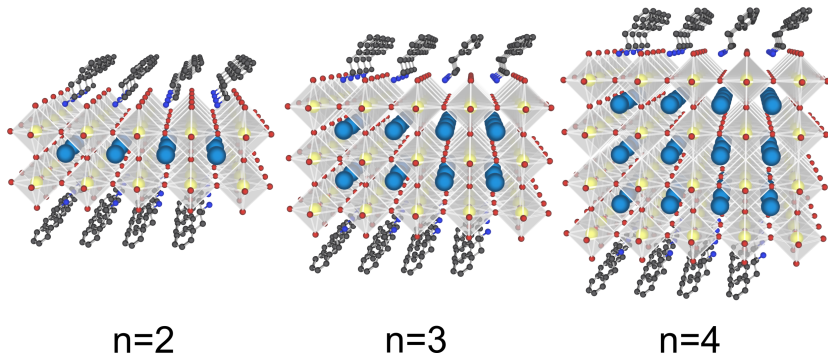
FIGURE 2.10: Differently sized quasi-2D perovskite quantum wells

intrinsic semiconductor. The absorption of light in the perovskite gen-
erates an electron and a hole as introduced in **Section 2.1**. This can be
either in the form of a bound exciton pair or free charge carriers. A
material gathering much interest for its potential use in perovskite so-
lar cells is methylammonium lead iodide ($MAPbI_3$) due to its low band
gap and exciton binding energy of approximately $1.6\,eV$ and $10\,meV$,
respectively [88]. This means that this perovskite can absorb almost all
of the sunlight and the created excitons can easily dissociate at room
temperature. The difference in the work functions of the ETL ad the
HTL results in an electric field applied over the perovskite leading to
electrons moving towards the ETL and holes moving towards the HTL.
This mechanism results in a voltage between the electrons attached to
the respective transport layers if the solar cell is exposed to light. This
mechanism is illustrated in **Figure 2.11**. For the efficient extraction, it
is, therefore, necessary that the excitons can easily dissociate and that
the charge carriers do not recombine before reaching the transport lay-
ers.
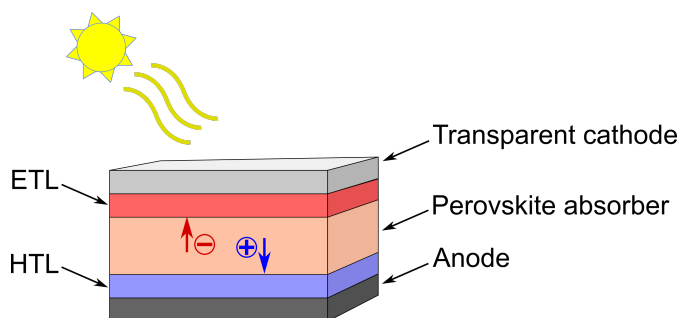
FIGURE 2.11: Illustration of a perovskite solar cell in n-i-p architecture with the electron transport layer (ETL) shown in red and the hole transport layer (HTL) in blue.

2.2.5 Perovskite light-emitting diodes

Similar to solar cells this work also discusses potential uses of different materials for perovskite light-emitting diodes. LEDs are in principle solar cells where instead of a voltage being generated from absorbed sunlight, a voltage is applied and the emission of light occurs. Charge carriers are introduced by the anode and the cathode and travel through the transport layers. Inside the perovskite, they then have the chance to recombine radiatively. Since excitons are charge-free quasi-particles they are not affected by the Coulomb interaction of charged trap sites in the same manner as free carriers are. The trapping of excitons is thereby reduced compared to free carriers. The band gap of the perovskite material determines the emission wavelength. For the efficient emission of light, a material with strong exciton binding energy should be chosen to avoid trapping of free carriers.

3

Characterization and Fabrication

3.1 Fabrication

In this work, samples were produced on a glass substrate, cut from microscope slides. The substrates were cleaned using an ultrasonic bath. Afterward, the substrates were further cleaned with an oxygen plasma. Then the substrates were spin-coated with the perovskite solutions and annealed on a hot plate.

3.1.1 Ultrasonic bath

The ultrasonic bath is a steel basin filled with water. The water transfers the ultrasonic waves coming from high-frequency panel absorbers on the outside of the basin towards a solution-filled beaker containing the samples. The beaker is put on a basket inside the basin so there is no direct contact between the beaker absorbers. A high-frequency generator is used with frequencies higher than $16\,\text{kHz}$. In the low-pressure phase, small gas bubbles are created close to the sample. In the high-pressure phase, the bubbles are compressed. In the next low-pressure phase, the bubbles expand again and grow. After multiple cycles, the bubbles grow to a size at which they are not stable any longer and implode. This implosion leads to very high pressure which cleans the sample and removes persistent contaminations. The glass substrates were
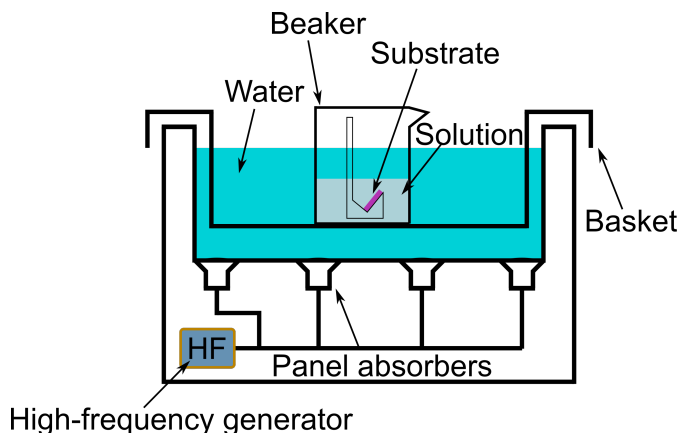
FIGURE 3.1: Schematic illustration of an ultrasonic cleaner

cleaned with acetone and isopropanol for ten minutes each. An illustration of an ultrasonic cleaner is presented in **Figure 3.1**.

3.1.2 Plasma cleaning

An oxygen plasma was used to further clean the substrates which improves the quality of the produced samples. The substrates are put into a chamber which allows the evacuation of air and the simultaneous flow of pure oxygen into the chamber. The low pressure eases the generation of plasma inside. Oxygen is used due to the emission of short wave UV light capable of breaking most organic molecules. Furthermore, the plasma-generated oxygen species are highly reactive binding to the molecule remenants. All substrates were kept in an oxygen plasma for five minutes. A schematic of plasma cleaning is shown in **Figure 3.2**.
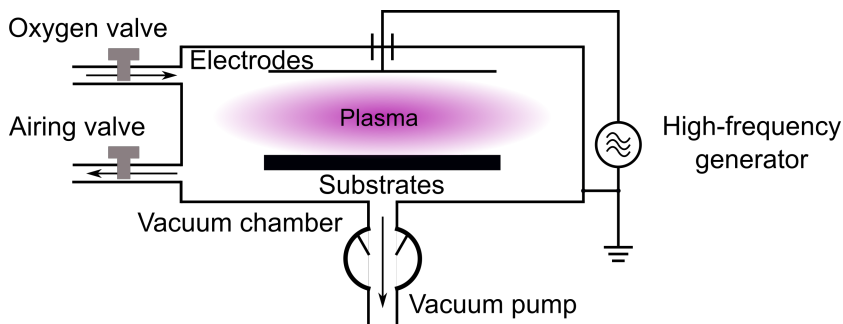
FIGURE 3.2: Schematic illustration of a plasma cleaner

3.1.3 Solution preparation

The 2D Ruddlesden-Popper perovskite utilizing phenethylamine (PEA) as a spacer molecule was prepared by solving PbI_2 in a solvent mixture of dimethylformamide (DMF) and dimethylsulfoxid (DMSO) with the volume ratio DMF/DMSO = 4:1 to reach molarity of $1.2\,M$. Then phenethylammonium iodide (PEAI) was added at a molarity of $2.4\,M$ thereby leading to a structural formula of A'_2BX_4 as introduced in **Section 2.2.2**. This recipe was taken from Milić et al. [89]. For the Dion-Jacobson perovskite utilizing 1,4-phenyl-enedimethanamine (PDMA) as a spacer PbI_2 was dissolved in DMF/DMSO at a ratio of 9:1 at a molarity of $0.4\,M$. Then $PDMAI_2$ was added to reach the same molarity leading to the structural formula $A''BX_4$ as introduced in **Section 2.2.2**. This method was taken from Li et al. [90].

The quasi-2D perovskite samples were prepared from solutions with different spacer concentrations. $5.3\,mg$ of 12-Crown-4 and $239.1\,mg$ of $CsPbBr_3$ were dissolved in $1\,mL$ of DMSO and then heated for 20

minutes at roughly 60 °C which leads to molarity of 0.4 M. The spacers used for the quasi-2D perovskites were butylamine (BA) and 1-naphthylmethylamine (NMA). The spacers were dissolved as BABr or NMABr in DMSO at a molarity of 2.8 M. The desired amount of spacer solution was then added to the $CsPbBr_3$ solution. The combined solution was then shaken at a temperature of 60 °C to ensure proper mixing [47].

3.1.4 Spin coating

Spin-coating onto substrates allows for thin and homogenous layers. The substrate is held by a hole with an applied vacuum in the center of the spinning disk as displayed in **Figure 3.3**. Evaporation of the solvent leads to a smooth solid film on the substrate. The thickness of the layer d depends on the rotational speed ω set on the device with $d \propto \frac{1}{\omega}$. The spin-coating in this work always took place in a nitrogen atmosphere to avoid any reaction of oxygen or water with the solutions or the finished films. The settings for the 2D-perovskites with PEA were 1000 rpm for 10 s with a ramp of 200 rpm s^{-1} and then 4000 rpm for 20 s with a ramp of 2000 rpm s^{-1} [89]. The 2D-perovskite utilizing PDMA was coated at 5000 rpm for 20 s at a ramp rate of 2000 rpm s^{-1} [90]. For the quasi-2D perovskites first at 1000 rpm for 20 s then afterward at 4000 rpm for 40 s both at the same ramp rate of 1000 rpm s^{-1} [47].

3.1.5 Annealing

The annealing of perovskite films after spin-coating improves the agglomeration of nanoparticles and improves the film quality [91]. The annealing temperature for the PEA 2D-perovskite was 140 °C for 10 min [89]; for the PDMA 2D-perovskite 200 °C for 1 min and then 150 °C for
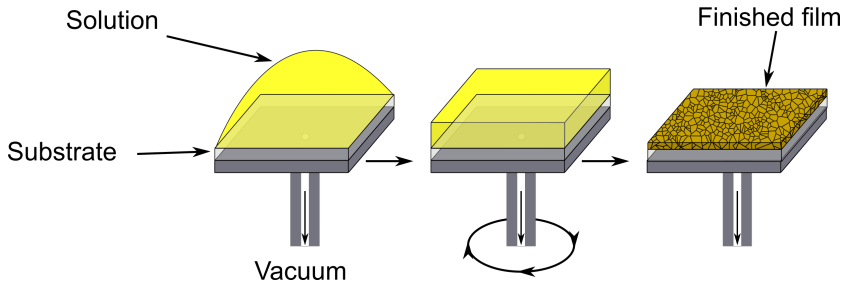
FIGURE 3.3: Schematic illustration of spin-coating

9 min [90]; for the quasi-2D perovskites the temperature was 70 °C for 15 min [47].

3.2 Characterization

3.2.1 Laser sources

In this work, the excitation of samples to analyze the photoluminescence was carried out with either a continuous wave or a pulsed laser source.

Continuous-wave laser emission

A continuous-wave laser emits laser light at constant intensity. Ideally, it has only a single wavelength. For continuous-wave excitation, a basic laser diode was used. These diodes are cost-efficient and can be pumped electrically, omitting the need for an external light source. This makes them a small and reliable tool for basic sample characterizations. Laser diodes typically consist of either two or three semiconductor layers (p-n, or p-i-n-junctions) which are positively doped (p), negatively doped (n), or undoped (i). The active region of these layers is in the boundary

layer for a p-n-junction or in the intrinsic layer for a p-i-n-junction. The output surfaces of the laser diode are polished to achieve partial reflectivity while the surface on the opposing side is polished to achieve high reflectivity. By injecting electrons in the n-doped region and holes in the p-doped region recombination of these charge carriers in the active region takes place leading to the emission of photons. The emitted photons are then either absorbed, reflected by one of the polished surfaces, or pass through the partially reflective surface and leave the device.
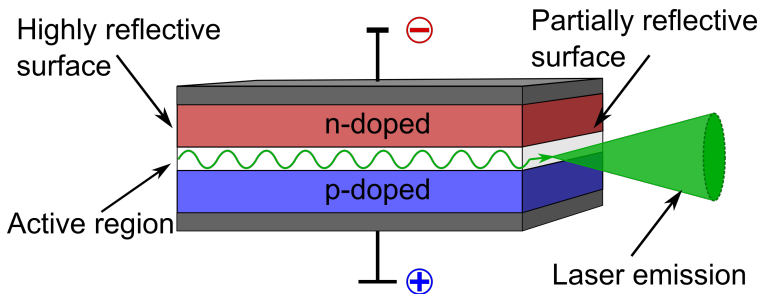
FIGURE 3.4: Schematic of a laser diode

Typically direct band gap materials are used for laser diodes. The band gap of the active region determines the wavelength of the laser emission. This leads to a great variety of laser diode wavelengths. With high densities of charge carriers in the active region, population inversion takes place whereby the stimulated emission of photons becomes more likely than the absorption of a said photon. By increasing the applied current great gains can be generated. The reflective surfaces act as a Fabry-Pérot-resonator. Due to the device setup and form of the active region, the output light has an elliptical beam profile which has to be accounted for by the output optics. Laser diodes have to be temperature controlled to avoid any drift in the wavelength due to temperature

changes which cause the interaction of phonons with the charge carriers. The used lasers were acquired from the company *Thorlabs*.

Picosecond pulsed laser emission

The source for picosecond pulses in this work came from a compact laser system from *InnoLas*, the Innolas picolo-1 MOPA. MOPA stands for master oscillator power amplifier. The system consists of two amplifying stages. The first is a Q-switched neodymium-doped yttrium vanadate (Nd:YVO$_4$) oscillator which provides laser pulses at a fundamental wavelength of 1064 nm. Q-switching is a method whereby the emission light in the cavity is attenuated so that there is no feedback into the gain medium. This means stimulated emission is reduced so that the population inversion resulting from pumping the gain medium can store a high amount of energy before lasing can occur. Once the gain medium is saturated, the attenuation is removed and lasing starts to occur very quickly resulting in a strong pulse with high peak intensity. The repetition rate in this work was typically at 1 kHz. The second stage is an amplifier that increases the pulse energy further. A second or third harmonic crystal can be used to reduce the output wavelength.

Femtosecond pulsed laser emission

In this work, the femtosecond pulsed laser source was a femtosecond laser from *LightConversion* called Pharos. Unlike a continuous-wave laser, the emission of a pulsed laser has a broad frequency bandwidth. The laser resonator might, depending on the gain medium, support a multitude of modes simultaneously. These modes vary in frequency by:

$$\Delta v = \frac{c}{2L} \tag{3.1}$$
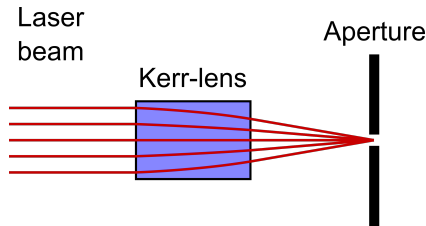
FIGURE 3.5: Schematic of a Kerr lens with a hard aperture

where ν is the frequency, c is the speed of light and L is the length of the resonator. Without any form of mode-locking by which the phases of the supported modes are in a fixed relationship with each other, no pulse generation takes place. In ideal conditions, however, the modes all constructively interfere periodically, thereby creating a short pulse. The broader that bandwidth is and the more modes are supported, the shorter a generated pulse can potentially be. This is described by the Fourier limit also known as energy-time uncertainty. In the pulsed laser source used in this work, this mode-locking is achieved via a Kerr lens. The Kerr effect is nonlinear whereby the refractive index of a material depends on the square of the electrical field applied to it. The working principle of a Kerr lens is shown in **Figure 3.5**. A laser beam inside of a resonator typically shows a gaussian beam profile. The electrical field in the middle of the beam profile is thereby stronger than further outside. If such a beam is passing a Kerr crystal, the refractive index of this crystal changes in a way that the center of the beam experiences a longer beam path than the outside which causes the beam to focus. This is similar to a traditional lens made from glass without the Kerr effect. Once a pulse is created inside the resonator, the self-focusing through the Kerr lens leads it past an aperture while the non-focused light gets blocked. This leads to only the pulse being amplified and only the pulse being able to cause stimulated emission in the gain material, thereby mode-locking

the longitudinal modes in the resonator. After leaving the oscillator resonator, the pulse gets stretched by a transmission grating stretcher before it enters the amplifier resonator via a pulse picker. The stretched pulse can be amplified more than an unamplified pulse. In the amplifier, the gain material is present as in the oscillator. In this laser system, ytterbium-doped potassium gadolinium tungstate (Yb:KGW) was used leading to a wavelength of 1026 nm. The pulse passes the optically pumped gain material multiple times, each time increasing its power. After the pulse is saturated and leaves the amplifier, it gets compressed via the same method as the stretching, thereby creating a very powerful short pulse. The pulse length depends on the compressor settings and is at roughly 260 fs. Since all investigated semiconductors in this work have a much higher band gap than could be excited with this laser, the laser wavelength had to be tuned with an optical parametric amplifier.

Optical parametric amplifier

The used OPA was an Orpheus from *LightConversion*. In the process of optical parametric amplification, two input beams with different wavelengths and a nonlinear crystal are used to amplify one beam and weaken the other. The desired wavelength is called signal while the other is called pump. The pump wavelength should be shorter. In this process, both the energy and the momentum are conserved meaning that additionally to the pump and the signal beam a beam with the energy difference between pump and signal leaves the crystal, also called the idler beam. For applications requiring long wavelengths, typically the idler is used instead of the signal. Since the input pulse in this OPA has a wavelength of 1026 nm it cannot directly be used as a pump. Therefore, the laser input passes a second harmonic crystal. In this crystal second harmonic generation (SHG) takes place, whereby two photons of lower energy are transformed into one photon with twice the energy.
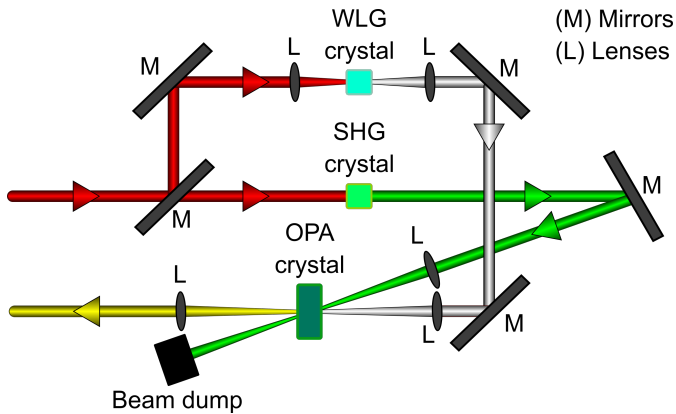
FIGURE 3.6: Schematic of the optical parametric amplifier. The input laser pulse is split into two beams, one passing a second harmonic generation crystal generating the pump pulse and the other a white-light generation crystal for the seed pulse. Both then pass an OPA crystal. Depending on the delay between white-light pulse and the pump pulse, a specific wavelength in the chirped white-light pulse gets amplified.

The resulting wavelength of 513 nm can then be used to pump the optical parametric amplification. A small fraction of the input pulse is deviated and does not pass the SHG crystal, instead, it passes a sapphire crystal generating white light. In this white-light generation, the narrow bandwidth pulse creates a chirped pulse with an extremely broad spectrum. The white light from a sapphire crystal is negatively chirped meaning that the front of the pulse consists of shorter wavelengths than the back of the pulse. This also means that by controlling the delay between the white-light and the pump pulse a specific wavelength can be amplified. This setup allows for the use of a wide range of pulsed wavelengths going from the second harmonic deep into the near-infrared (using the

idler). Directly at the output of the OPA, a second harmonic crystal system called Lyra from *LightConversion* was used to achieve short wavelengths as short as 315 nm as well as to filter the two unwanted beams (pump and signal or pump and idler). Additionally, the pure second harmonic or third harmonic of the input laser could be used by using a different setup involving a system called Hiro from *LightConversion*.

3.2.2 Cryostat

An Optistat Dry TLEX cryostat from *Oxford instruments* which uses a closed-cycle helium process was used. The cryostat utilizes a two-stage Gifford-McMahon refrigeration system. In this method, a compressor is used to supply the refrigeration device with a high- and a low-pressure line. A displacer inside of a cylinder is used to force the gas to either end of said cylinder. Depending on the applied pressure by the supply lines, gas either gets compressed creating heat, or expands cooling down. By synchronously using the displacer in combination with the applied pressures one end of the cylinder is cooled down while the other end is heated. The displacer can additionally act as a regenerator by retaining some of the cooling in between cooling cycles. The sample holder was fitted with a temperature sensor and a heating device so specific temperatures in the sample could be achieved. This cooling system allowed us to reach temperatures as low as 4 K and at a maximum 300 K. The upper limit is due to potential damages to sensors at higher temperatures.

3.2.3 Spectrometers

For time-integrated spectra, a small spectrometer from *Ocean insight* called USB2000+ was used. Streak camera spectra were taken by using a bigger spectrometer from *Princeton Instruments* called Acton SP2300. In these optical spectrometers, light is directed towards a reflective
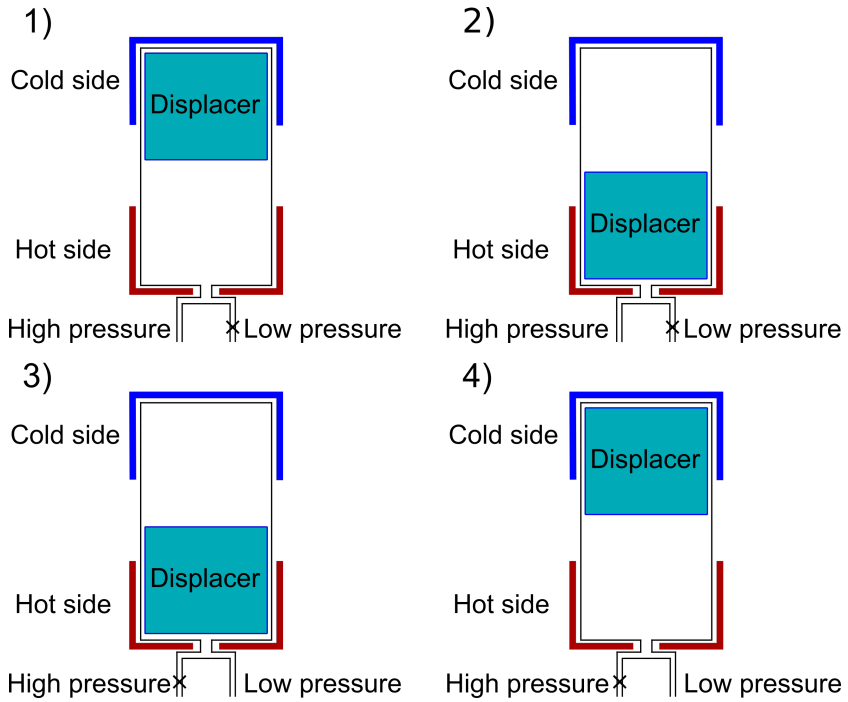
FIGURE 3.7: Schematic of the Gifford-McMahon process. From 1) to 2) the displacer moves downwards pushing the gas towards the cold side while high pressure is applied. From 2) to 3) low pressure is applied and the gas expands, thereby cooling the cold side. From 3) to 4) the displacer moves upwards, pushing the gas downwards. From 4) to 1) high pressure is applied to compress the gas and heat the hot side.

diffraction grating. This grating introduces a path difference between the rays of light depending on the input angle, the output angle, and the grating spacing. If this path difference is an integer multiple of the
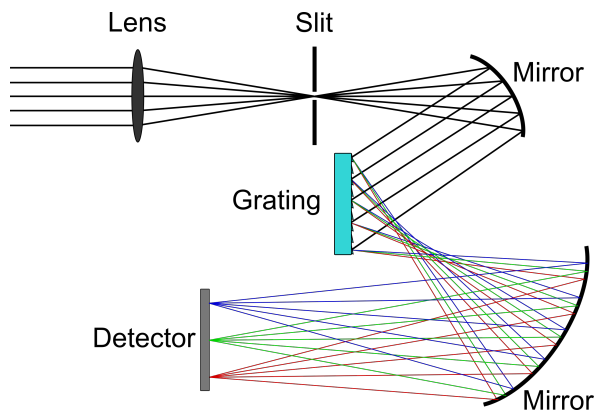
FIGURE 3.8: Schematic of a diffraction grating optical spectrometer

wavelength, the rays interfere constructively. This wavelength depen-
dence leads to each wavelength experiencing a different output angle for
constructive interference. This splitting of the input beam into beams of
specific wavelengths is then imaged onto a detector.

3.2.4 Streak camera

A streak camera is used to measure time-resolved photoluminescence
spectra. The temporal resolution can vary between microseconds and
picoseconds. For the time-resolved spectra, the photoluminescence light
first passes a spectrometer and is then focused into the streak cam-
era input-slit. The used camera was a C10910-02 from *Hamamatsu*.
The input light is focused on a photocathode by the input optics where
electrons are emitted based on the photoelectric effect. The amount
of emitted electrons is proportional to the input light intensity. The
emitted electrons are accelerated via an accelerating electrode and lead
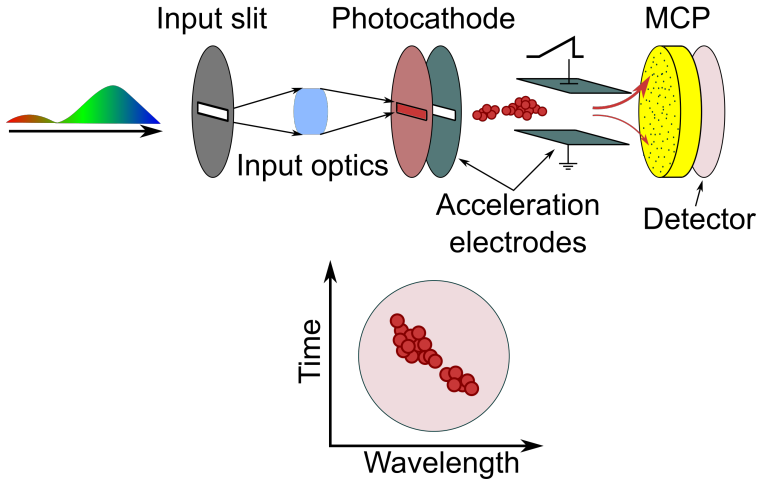
FIGURE 3.9: Schematic illustrating the operation of a streak camera. The input light coming from a spectrometer is focused on a photocathode where electrons are emitted. These electrons pass a capacitor being deviated by the applied sawtooth signal. They pass a microchannel plate (MCP) where secondary electrons are emitted and hit a phosphor screen which then emits light.

into a capacitor which is supplied with a sweeping voltage applied synchronously with the light pulse repetition rate (triggered by the laser system). For the correct timing between the light pulse entering the capacitor and the voltage application, the delay generator DG645 from *Stanford Research* was used. The higher the applied voltage, the more the electrons deviate from their flight pass. In a single sweep unit as used in this work (M10913-11), a sawtooth signal is applied to the sweep capacitor meaning that electrons arriving later get deviated by

the sweep capacitor more than electrons arriving earlier. Behind the capacitor system, the electrons are met by a microchannel plate (MCP). An MCP consists of a lead glass plate with many microscopic channels. Both ends of the plate are metallic with a high voltage applied to them meant to accelerate electrons. The inside of the microscopic channels is made from semiconductor material. The MCP is slightly tilted relative to the electron flight path. If an electron hits the inside of the channels in the MCP, secondary electrons might be emitted which then get accelerated by the applied voltage. This can lead to the secondary electrons hitting the inside of the channel again, thereby emitting further secondary electrons drastically increasing the number of total electrons similar to a photomultiplier. Behind the MCP is a phosphor screen that emits photoluminescence if hit by electrons. This photoluminescence is then detected by a CCD camera. With the camera used in this work time windows between a nanosecond and a millisecond could be measured.

3.2.5 Absorption measurement

Measuring the absorption spectra was done by utilizing a fully integrated system by *PerkinElmar* called LAMBDA 950 UV/Vis/NIR. This system contains two light sources: a tungsten halogen lamp for the visible and near-infrared range and a deuterium lamp for the UV region. The light passes a double monochromator so that only the absorption at a specific wavelength is measured at a time. A reflective chopper splits the light into a reference beam and a sample beam to account for potential intensity fluctuations during the measurement. Both the sample and the reference beam then enter an integrating sphere, although not on the same path. While the sample beam is aimed at the sample holder, the reference beam is aimed to not hit the sample directly but instead hit the inside wall of the integrating sphere first. For the light detection, either a photomultiplier tube for wavelengths between 200 nm to 860 nm
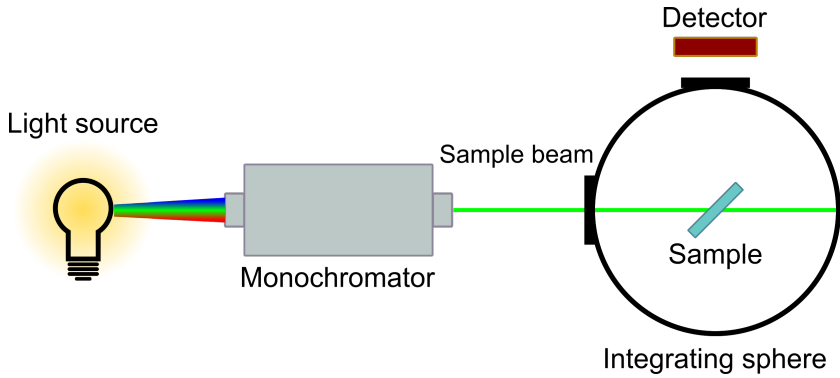
FIGURE 3.10: Schematic illustration of the absorbance measurement setup

or a InGaAs-detector for wavelengths between 860 nm to 2500 nm is used. Two measurements are necessary to extract the absorption spectra, one with the sample in the integrating sphere and one without. The absorbance can then be calculated according to:

$$A = log_{10}\left(\frac{I_{0,s} \cdot I_{0,r}}{I_{1,s} \cdot I_{1,r}}\right),$$ (3.2)

where A is the absorbance, I is the intensity and the indices s and r stand for sample beam and reference beam respectively.

4

Excited State Species in 2D-Perovskites at Cryogenic Temperatures

In this chapter, the excited state species in 2D-perovskites and their PL emission are described. Since these perovskites consist of purely one phase, they are an excellent starting point for the research of emission from quantum-confined perovskite crystals. It is detailed how the PL-spectra of 2D lead iodide perovskites depend on the excited-state density and the temperature. There are two emitting excited-state species in these perovskites: free excitons (Free Excitons (FE)) and bound excitons (Bound Exciton (BE)). Free excitons dominate the emission spectra at room temperature at all measured excited-state densities, however, at cryogenic temperatures and high excited-state densities strong exciton-exciton annihilation (EEA) suppresses the FE-emission to an extent that other emissions like BE-emission or emissions from PbI_2 inclusions become dominant. Both the Ruddlesden-Popper (RP) phase utilizing phenethylamine (PEA) as a spacer (PEA_2PbI_4, PEPI) and the Dion-Jacobson (DJ) phase utilizing 1,4-phenylenedimethanamine (PDMA) were investigated by using both a continuous wave (CW) and a pulsed laser source. At CW excitation FE-emission dominates at all investigated temperatures. For the PEPI femtosecond pulsed excitation and temperatures below $100\,K$ lead to dominant BE-emission redshifted

from the FE emission peak by 40.3 meV. Additionally weak emission from PbI$_2$ inclusions at higher energies than the FE-emission peak by 170 meV is observed under these conditions. The FE-emission first increases with decreasing temperature between 290 K and 140 K and then decreases with decreasing temperature which can be explained by an equilibrium between the FE and BE until BE become stable at low temperatures. The same behavior of a reduction of FE-emission at cryogenic temperatures by EEA is also observed for the DJ-perovskite. The BE-emission, however, is not as pronounced as in the RP-perovskite. In the DJ-perovskite a broad emission redshifted by 390 meV from the FE-emission peak was observed at low temperatures under pulsed excitation leading to high excited-state densities. This emission likely arises from PbI$_2$ inclusions in the material based on the comparison with temperature-dependent measurements of PbI$_2$ films. Potential avenues for the improvement of PL-emission at room temperature are discussed in this chapter.

This chapter is based on my first-author publication *"How free exciton–exciton annihilation lets bound exciton emission dominate the photoluminescence of 2D-perovskites under high-fluence pulsed excitation at cryogenic temperatures"* [92] in the Journal of Applied Physics.

4.1 Motivation

Layered 2D metal halide perovskites are gathering interest from various fields of research including photovoltaics, photon-detectors, light-emitting diodes, and spintronic devices [93]. For the development of application devices the fundamental understanding of charge carrier dynamics and recombination pathways in these 2D materials needs to be

further understood, for example how Rashba splitting [94–98], self-trapped excitons [99–105] , and layer-edge states [106–108], might influence the material's performance. The nature of the excitonic emission lines in these 2D -perovskites is still under investigation. The phase pure RP 2D-perovskite utilizing PEA, as a spacer molecule (also known as PEPI) that is studied is a benchmark 2D perovskite material. Its excitonic PL continues to be investigated in the literature [109]. As of yet, no consensus has been reached on the PL features; in particular, the similarity of the low energy peaks, only visible at cryogenic temperatures, have been ascribed to phonon replica [110,111], biexcitons [52,53,112] triexcitons, [54], and bound excitons [113–115], in the various publications.

As described in **Section 2.1.3**, bound excitons are excitons trapped by defects inside a semiconductor. This leads to reduced emission energy of BE compared to FE. The trapped BE has no kinetic energy, which leads to a narrow linewidth of the PL-emission in traditional semiconductors as the linewidth is usually limited by the distribution of exciton kinetic energies. This linewidth is also temperature-independent. In 2D-perovskites however, the strong exciton-phonon coupling is the dominant effect determining the linewidth leading to broad and temperature-dependent emission peaks [116]. For high excitation densities, the trapping centers become occupied. This leads to an increase in the ratio of FE-emission to BE-emission with increasing fluence as the density of FE increases more than the BE density.

Localized excitons are similar to BE, but unlike excitons being trapped by a defect, they become localized by static disorder in the crystal leading to regions of lower energy material compared to the surrounding material. Localized excitons typically have higher energy emissions than BE but lower energy emissions than FE. As the disorder leads to a distribution of emission energies, the overlap of these emissions leads to

a Gaussian lineshape; therefore emissions with Gaussian lineshape and lower energy emission than FE often get attributed to localized excitons [117, 118].

Two excitons can associate to form a quasi-particle from an energetically stabilized four-particle state which is called a biexciton. The probability of biexciton formation depends on the probability of two excitons meeting which is greatly enhanced with increasing excitation fluence. Biexcitonic emission scales with the square of the excitation fluence. In biexciton recombination, the emitted PL-emission energy is lower than the FE-emission energy, and a single exciton remains. This leads to the exciton emission intensity remaining linear with excitation fluence at low fluences and in the absence of other effects even in the case that biexcitons are formed.

Two different 2D perovskite spacers, phenethylamine (PEA) and 1,4-phenyl-enedimethanamine (PDMA), leading to different crystal phases, Ruddlesden-Popper (RP) and Dion-Jacobson (DJ), are investigated. To best compare the different phases, the spacers were chosen for their strong similarity shown in **Figure 4.1**.

Both continuous wave (CW) and pulsed excitation are used to record the temperature-dependent PL. Surprisingly, the PL below $100\,\mathrm{K}$ differs drastically depending on the excitation source, indicating that the excited-state density in the film influences the processes responsible for different regions of the PL emission spectrum. Intensity-dependent PL measurements at low-temperatures are used to show that the high- and low-energy emission features mainly stem from populations of FE and BE respectively in the RP material, and FE and PbI_2 inclusions in the DJ material. The differences observed in the PL emission spectra depending on CW or pulsed excitation are attributed to a decrease in the FE emission efficiency due to exciton-exciton annihilation (EEA) due to

a

NH2

NH2

b

NH2
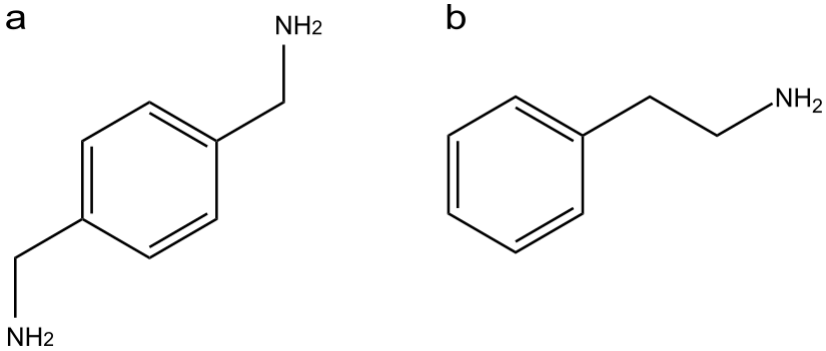
FIGURE 4.1: a) PDMA and b) PEA used as the ligands for the Dion-Jacobson phase and the Ruddlesden-Popper phase 2D perovskite respectively. Adapted from [92], with the permission of AIP Publishing.

the higher excited-state density under pulsed excitation. This decrease in emission efficiency with fluence is not affecting BE and the PbI_2 emission to the same extent. This explains the dominance of FE PL emission for CW excitation and the dominance of BE or PbI_2 emission under pulsed excitation at low temperatures.

4.2 Temperature dependence of PEPI PL under CW and pulsed excitation

The temperature-dependence of the PL emission of RP PEPI thin films under CW and pulsed laser excitation is examined (**Figure 4.2**). The power density for the CW excitation is $165\,mW\,cm^{-2}$ at 405 nm, and the pulsed excitation provides an energy density of $48\,\mu J\,cm^{-2}$ per excitation pulse at 430 nm at a repetition rate of 20 kHz and a pulse duration
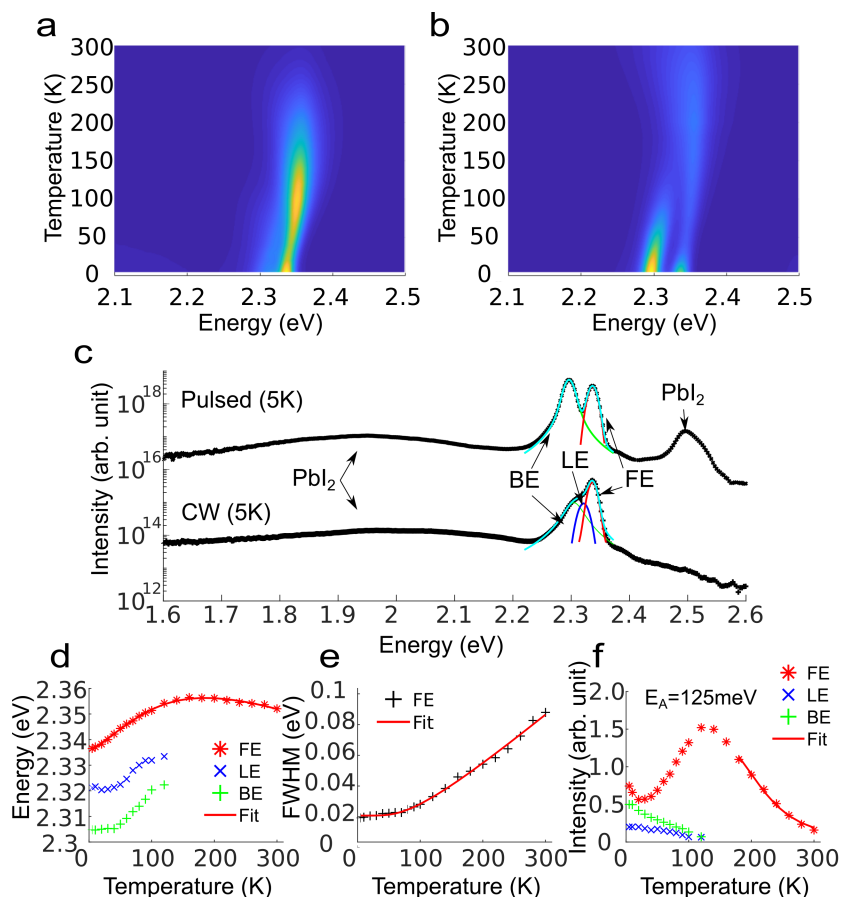
FIGURE 4.2: Temperature-dependent PL spectra for PEPI (PEA$_2$PbI$_4$) for a) CW excitation (165 mW cm^{-2}, 405 nm), and b) pulsed excitation (48 μJ cm^{-2}, 430 nm, 260 fs). c) Comparison of emission spectra showing the effect of PbI$_2$ inclusions, bound excitons (BE), localized excitons (LE), and free excitons (FE) for CW and pulsed excitation at 5 K. Temperature-dependent d) peak positions of the BE, LE, and FE emission under CW excitation with the fit utilizing equation (1), e) full-width half maximum (FWHM) of the FE peaks with the fit utilizing equation (2) and f) PL intensity (peak area) for BE, LE, and FE with an Arrhenius fit. Adapted from [92], with the permission of AIP Publishing.
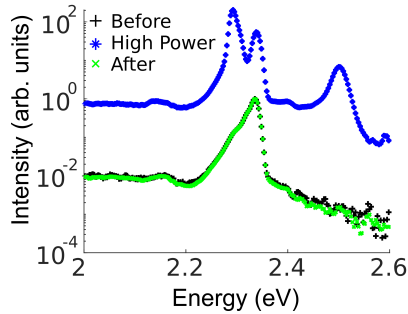
FIGURE 4.3: Spectra at low fluence $(20\,\mathrm{nJ\,cm^{-2}})$ before and after high fluence $(9\,\mathrm{\mu J\,cm^{-2}})$ at $430\,\mathrm{nm}$ and $20\,\mathrm{kHz}$ exposure for two minutes at $5\,\mathrm{K}$ with the PEPI material. There is no change observable at $2.5\,\mathrm{eV}$. Adapted from [92], with the permission of AIP Publishing.

of $260\,\mathrm{fs}$. For comparison, this corresponds to a peak power of approximately $185\,\mathrm{MW\,cm^{-2}}$. The PL spectra under prolonged illumination at a given temperature for both CW and pulsed excitation remained invariant, revealing that the samples are stable and do not degenerate during the measurement process (see **Figure 4.3**). The perovskite film thickness of the PEPI samples $(55\pm2)\,\mathrm{nm}$ is determined with a profilometer and the morphology has an RMS of $2.0\,\mathrm{nm}$ (see **Figure 4.4**). The thickness of the PEPI film is known to affect the energy of the PL emission peak. Reabsorption of the material in thicker films causes a peak shift of up to $30\,\mathrm{meV}$ towards lower energies compared to the true single-layer emission [119].

As apparent immediately upon the comparison of **Figure 4.2a** and **b**, the PL at lower temperatures is different depending on the excitation with CW or pulsed radiation. This difference is inferable from the vast difference in excited-state densities under the respective conditions. Under CW excitation the excited-state density can be estimated utilizing
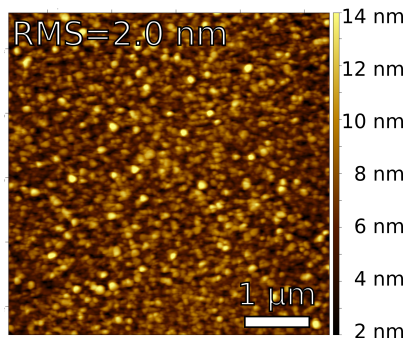
FIGURE 4.4: Exemplary atomic force microscopy image of a PEPI film used in this work showing a smooth surface. Adapted from [92], with the permission of AIP Publishing.

the monomolecular lifetime of 704 ps determined below, to be approximately $1.74 \times 10^{13}\,\mathrm{cm}^{-3}$. The initial excited-state density under the pulsed excitation on the other hand is $7.2 \times 10^{18}\,\mathrm{cm}^{-3}$.

With the CW excitation displayed in **Figure 4.2a**, the apparently single band at approximately 2.34 eV is dominant in the PL at all measured temperatures. This band is assigned to free exciton (FE) emission and will be referred to as such from here on for simplicity's sake. The FE peak energy position shifts with temperature since the band gap of the material is temperature-dependent. Two effects are affecting the band gap: As phonon-coupling decreases with decreasing temperature, the emission peak moves towards higher energies until the temperature of 140 K is reached. After that the contraction of the lattice dominates the energy shifting, causing the band gap to decrease with decreasing temperature. This observation agrees with literature reports [120–123], and is explained in more detail below. Starting at room temperature the intensity of the FE emission increases with temperature until about 120 K,

with further decreasing temperature the emission intensity starts to decrease till around 20 K, and at last, increases again with the temperature reducing towards 5 K. Later on, this unique dependence on temperature will be discussed in terms of a shifting equilibrium between FE and bound excitons, wherein the transition rates from FE to bound and localized excitons and vice versa depend on the temperature, as do the nonradiative rates of the free and bound exciton states.

The PL under pulsed excitation demonstrates two distinguished peaks below 120 K which differs significantly from the observations under CW excitation. The higher energy emission peak is positioned at similar energy as the main emission peak assigned to FE under CW excitation. At low temperatures, however, the lower energy peak starts to dominate the PL emission (as displayed in **Figure 4.2b**. The lower energy peak overlaps with the band attributed to bound excitons under CW excitation, albeit with a slightly narrower linewidth of approximately 20 meV FWHM compared to 35 meV FWHM in the case of CW excitation, and a 40 meV redshift from the center of the FE emission peak as compared to 32 meV in the CW excitation case at 5 K. This lower energy emission peak is assigned to bound excitons (BE) for both pulsed and CW excitation based on the lineshape, lifetime, and intensity-dependence in addition to the similarities to findings in the literature [113, 114]. It should be noted that similar observations of two distinct peaks can be made in 3D-perovskites based on the reabsorption of PL emission by the Urbach tail even though the true emission spectrum only consists of a single emission peak [124]. This effect is not sufficient to explain the observed double peak and its reproducibility and reversibility that arises upon varying the excited-state density in the films described in this work.

For the analysis of the intensity, peak width, and peak position of each spectral component in the presented data in **Figure 4.2a** and **b**, the PL
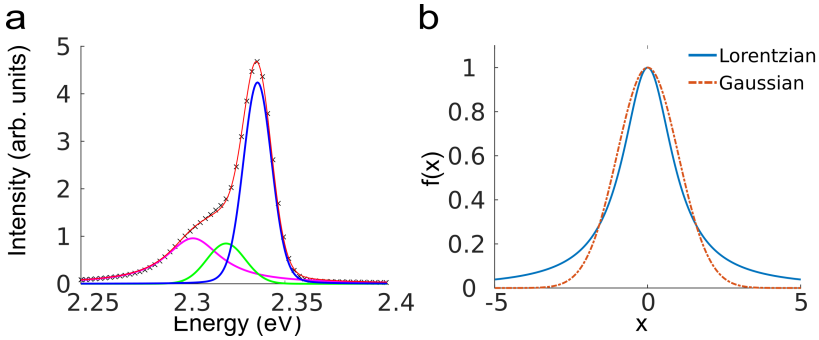
FIGURE 4.5: a) Exemplary three peak fit of the PEPI material at 5 K under CW excitation ($165 \, \mathrm{mW \, cm^{-2}}$, 405 nm) using Voigt profiles to determine if the lineshape is more Gaussian or Lorentzian and b) Difference between these two profiles. Adapted from [92], with the permission of AIP Publishing.

spectra are fitted at each temperature with either one Voigt peak at higher temperatures, and either two (pulsed), or three (CW) Voigt profiles at lower temperatures. It should be noted that an additional peak between the FE and BE peaks is necessary for a fit of the spectra under CW excitation. The lineshape of that additional peak is more Gaussian than the lower energy BE peak (see **Figure 4.5** and **Figure 4.6**) and also is suppressed rather than enhanced at high excited-state densities.

It can be speculated that the emission is due to localized excitons in lower band gap areas of the quantum wells which are affected by the disorder in the lattice. This would explain the Gaussian lineshape and is consistent with the presented evidence below, regarding the mechanism leading to enhanced BE emission at higher excitation densities. However, no definite assignment to localized excitons can be made solely based on our observations and further study of this material is necessary in the future. Furthermore, it should be noted that for temperatures
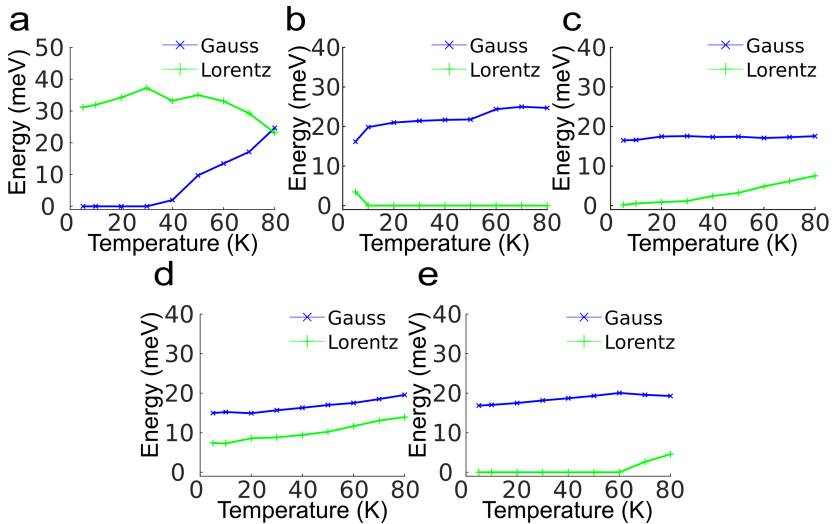
FIGURE 4.6: Temperature-dependence of the Voigt profile widths in the PEPI material under CW excitation (165 mW cm^{-2}, 405 nm) for the a) bound excitons, b) localized excitons and c) free excitons and under pulsed excitation (48 µJ cm^{-2}, 430 nm) d) bound excitons and e) free excitons. Adapted from [92], with the permission of AIP Publishing.

above 120 K a single Voigt profile is used to fit the data. At higher temperatures, the measured PL peak becomes asymmetric with the higher energy side dropping off more quickly than the lower energy side. The asymmetric peak is shown in **Figure 4.7** and can be explained by the partial reabsorption of the high-energy side of the peak at higher temperatures due to the increased FWHM of the FE emission peak [125].

The peak fitting results are presented in **Figure 4.2d** for the data measured with CW excitation and in **Figure 4.8** for the data acquired with pulsed excitation.
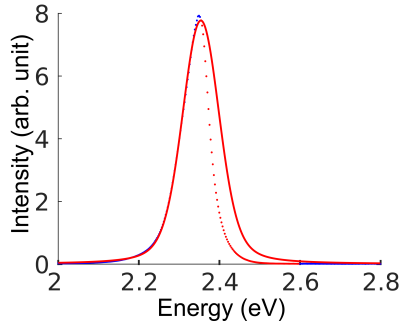
FIGURE 4.7: Asymmetric peak due to reabsorption fitted with a Voigt profile under pulsed excitation ($48\,\mu J\,cm^{-2}$, $430\,nm$, $260\,fs$) at $300\,K$ in the PEPI material. Adapted from [92], with the permission of AIP Publishing.

As mentioned above, the peak position and thereby the band gap of the material is temperature-dependent and is affected by the effects of lattice expansion and electron-phonon coupling. The valence band maximum and the conduction band minimum energies depend on the overlap of the metal s- and halide p-orbitals and the overlap of the metal p- and halide p-orbitals, respectively [126]. Increasing the metal-halide orbital overlap leads to a strong increase in the valence band energy and a less strong increase in the conduction band energy. The band gap energy thereby gets decreased. It follows that lattice expansion due to temperature increase leads to an increase in the band gap energy. The electron-phonon coupling on the other hand leads to band gap renormalization which decreases the band gap energy. Going from low temperatures to high temperatures the band gap first increases due to lattice expansion
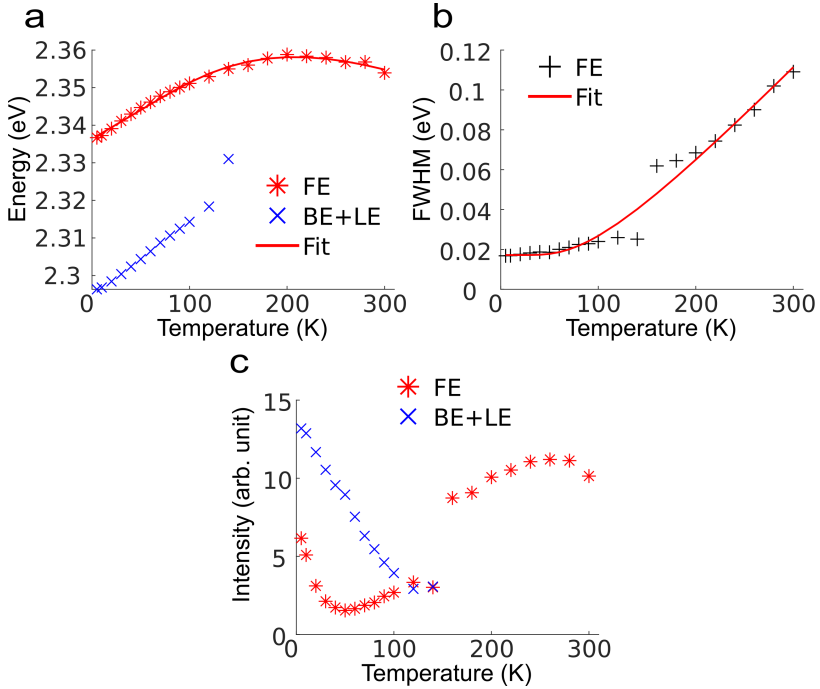
FIGURE 4.8: Temperature-dependent change of the a) peak energy b) FWHM and c) PL of the free (FE), bound (BE), and localized (LE) excitons under pulsed excitation ($48\,\mu J\,cm^{-2}$, 430 nm, 260 fs) in the PEPI material. The peaks become difficult to distinguish at some temperatures due to their overlap. Localized excitons especially are well hidden until temperature reaches below 140 K where the peak is around 2.33 eV. Above 140 K the peaks cannot be distinguished leading to a jump in the PL emission and also in the FWHM. Adapted from [92], with the permission of AIP Publishing.

and then decreases as electron-phonon coupling becomes more dominant. This interaction can be described with **Equation 4.1**:

$$E_g(T) = E_0 + A_{TE}T + A_{EP}\left(\frac{2}{exp(E_{PH}/(k_B T)) - 1} + 1\right), \qquad (4.1)$$

where E_0 is the unrenormalized bandgap, A_{TE} and A_{EP} are the weights of the thermal expansion and electron-phonon coupling respectively and E_{PH} is the average optical phonon energy [120–123]. The FWHM of the emission peaks is also affected by electron-phonon coupling whereby increasing temperatures cause increasing peak widths, which is described by **Equation 4.2**:

$$\Gamma(T) = \Gamma(0) + \frac{\gamma_{LO}}{exp(E_{LO}/(k_B T)) - 1}, \qquad (4.2)$$

where $\Gamma(0)$ is the inhomogeneous broadening, γ_{LO} is the electron-phonon coupling strength for Fröhlich scattering with the longitude optical phonon and E_{LO} is the energy of the phonon [127].

Based on these equations the peak energies and the FWHM of the peaks for CW and pulsed excitations can be fit as shown in **Figure 4.2** and **Figure 4.8**, respectively. The resulting parameters from the peak energy are presented in **Table 4.1**. The parameters for the FWHM fit are

TABLE 4.1: Parameters of the peak-position-fit

Excitation	E_0 (meV)	A_{TE} (meV K^{-1})	A_{EP} (meV)	E_{PH} (meV)
CW	2404 ± 5	0.18 ± 0.005	69 ± 4	-40 ± 2
Pulsed	2430 ± 20	0.154 ± 0.006	100 ± 10	-53 ± 4

shown in **Table 4.2**. The parameters for the FWHM agree well with

those in the literature [127] which are given in the Reference row. The electron-phonon coupling energies were determined to be 22 meV and 24 meV for CW and pulsed excitation, respectively. It should be noted that the pulsed excitation measurement leads to higher uncertainties due to unavoidable fitting imprecisions at temperatures between 100 K to 200 K where the BE and FE peaks are gradually merging. Although the extracted parameters agree within their uncertainties, some systematic differences may be included in the pulsed data due to small peak shifts caused by second-order processes. The parameters extracted from the CW excitation data can be considered more reliable, and compare well with those determined by Zhang et al. [127].

TABLE 4.2: Parameters of the FWHM-Fit

Excitation	S_0 (eV)	γ_{LO} (eV)	$E_{LO}(eV)$
CW	0.01722 ± 0.00006	0.09 ± 0.01	0.022 ± 0.002
Pulsed	0.017 ± 0.002	0.14 ± 0.04	0.024 ± 0.005
Reference	0.03 ± 0.001	0.07 ± 0.009	0.029 ± 0.002

The emission PL intensity of both FE and BE is temperature-dependent under CW excitation. The PL of the FE emission increases steadily as the temperature decreases from 300 K to 120 K, while no BE emission is observed. It is likely that at these relatively high temperatures the thermal energy is enough to free the BE which transition to FE. The equilibrium between the forming of BE from FE and the FE reforming from BE strongly favor FE at high temperatures. The increase in FE emission can be explained by a temperature-activated nonradiative recombination pathway which has an activation energy of approximately 125 meV from an Arrhenius fit of the data in this region, as shown in **Figure 4.2f**. Above 120 K FEs dominate the excited-state population

and PL emission spectra and suffer from a temperature-activated nonradiative rate. The activation energy of the nonradiative pathway is consistent with many vibrational modes of organic molecules. Increasing molecular vibrations might contribute to the nonradiative activation at higher temperatures.

As the temperature decreases (120 K to 30 K), the FE emission under CW excitation begins to decrease, while the BE emission begins to increase with a similar slope to the decrease of the FE emission. This indicates a shift in the equilibrium between FE and bound and/or localized excitonic states. The thermal energy is not enough for the BE states to easily transition toward FE states which changes the equilibrium in favor of the BE states, thereby explaining the decrease in intensity of the FE emission and the increase in the intensity of the BE emission. Finally, at temperatures below 30 K the FE emission starts to increase again, which can be interpreted as being caused by an activation energy necessary for excitons to become bound. So as the temperature increases, the probability of an exciton to be bound first increases and afterward decreases again.

The temperature dependence under CW excitation is now compared to that under intense pulsed excitation (48 μJ cm^{-2}, 430 nm, 260 fs). While the peak energy position of the FE emission is consistent for both excitation types, the intensity of the FE emission shows significantly different behavior with temperature. The total FE emission stays relatively constant with the temperature down to ≈160 K, then decreases as the BE emission begins to dominate below 160 K. The decrease in FE emission and the following increase in BE emission is consistent with the CW data. This is due to a decrease in the FE population and an increase in the BE population as there is no longer sufficient thermal energy for BE to return to the FE population.
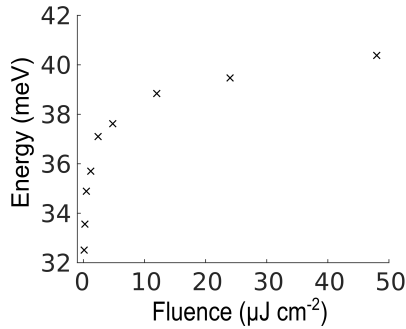
FIGURE 4.9: Fluence-dependent redshift of the bound exciton peak at
5 K under pulsed excitation in the PEPI material. Adapted from [92],
with the permission of AIP Publishing.

There is a slight difference in the peak position of the BE emission under
pulsed excitation compared to CW. The shift in the BE emission peak
depends on the pulsed excitation fluence (**Figure 4.9**, and below). The
BE emission peak agrees well with that observed under CW excitation
at lower pulsed excitation fluences.

Furthermore, an emission band is observed at 2.5 eV under pulsed exci-
tation which is not seen under CW excitation. This feature as well as a
broad emission around 2 eV is also visible in a pure PbI_2 film (**Figure
4.10**).In addition to the similarities in the spectra, the same temperature-
dependence (**Figure 4.11**) and power-dependence (**Figure 4.12**) of the
2.5 eV peak is observed in the perovskite and the pure PbI_2 film.

Based on these findings it can be concluded that the weak emission fea-
tures at high excitation fluences present under pulsed excitation are due
to PbI_2 inclusions in the film. The intense excitation however is not
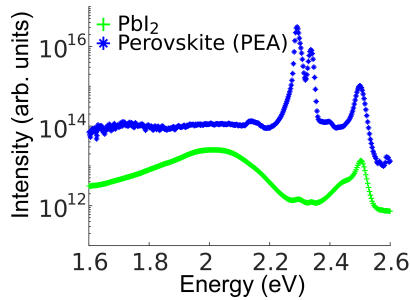
FIGURE 4.10: Comparison of the RP-perovskite (PEA, PEPI) with pure PbI_2 at 5 K under pulsed excitation ($9\,\mu J\,cm^{-2}$, 430 nm). Adapted from [92], with the permission of AIP Publishing.

responsible for the creation of the PbI_2 inclusions as there is no irreversible sample change. The spectrum before and after intense excitation is observed to be the same as shown in **Figure 4.3**.

The broad but weak emission peak that can be seen on the low energy side under both CW and pulsed excitation is assigned to surface defects of the PbI_2 inclusions [128]. This emission decays quickly with rising temperatures similar to the perovskite and the pure PbI_2 films (**Figure 4.13**).

Two important questions arise from these observations: Why is the FE emission relatively constant with the temperature above ≈ 160 K and why is the BE emission stronger than the FE emission at low temperatures for pulsed excitation? Both questions can be answered by considering exciton-exciton annihilation (EEA) of the FE population. EEA reduces the lifetime of the emission significantly at all temperatures under pulsed excitation. The dominant nonradiative recombination pathway at high temperatures is thereby EEA which is not the case under CW excitation. The nonradiative rate therefore only minorly affects the
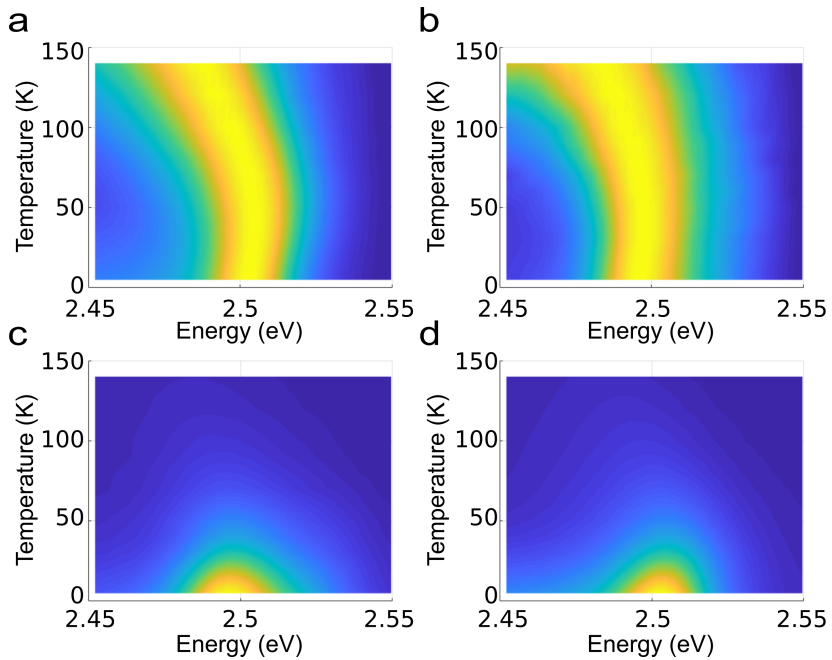
FIGURE 4.11: Temperature-dependent emission at 2.5 eV normalized under pulsed excitation at 430 nm for a) PbI_2 (9 μJ cm^{-2}) and b) RP-perovskite (PEA, PEPI) (9 μJ cm^{-2}) and not normalized c) PbI_2 and d) RP-perovskite (PEA, PEPI). Adapted from [92], with the permission of AIP Publishing.
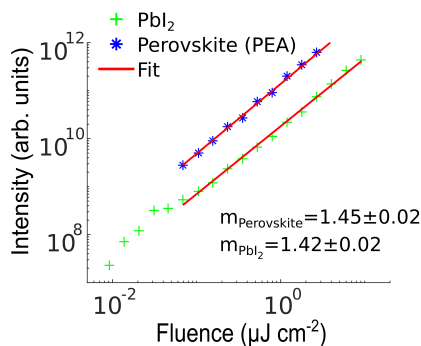
FIGURE 4.12: Fluence-dependent emission at 5 K of the 2.5 eV peak under pulsed excitation at 430 nm for a PbI_2 and an RP-perovskite (PEA, PEPI) film. Adapted from [92], with the permission of AIP Publishing.
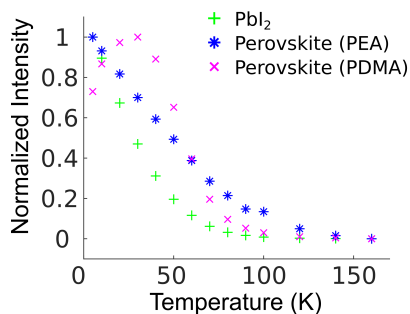
FIGURE 4.13: Temperature-dependence of the normalized low energy emission under pulsed excitation at 430 nm in PbI_2 ($9\,\mu J\,cm^{-2}$), RP-perovskite (PEA, PEPI) ($48\,\mu J\,cm^{-2}$), and DJ-perovskite (PDMA) ($48\,\mu J\,cm^{-2}$). Adapted from [92], with the permission of AIP Publishing.

emission lifetime and thus its intensity under pulsed excitation. At low temperatures, the FE emission is suppressed to such an extent that the BE emission overwhelms the FE emission. To verify that the detailed mechanism of EEA is indeed the source of the described observations, time-resolved, as well as intensity-dependent photoluminescence experiments are carried out.

Further insight into this material can be gained by simply varying the pulse energy from $0.12\,\mu J/cm^2$ to $48\,\mu J/cm^2$ ($430\,nm$, $260\,fs$, $20\,kHz$) while keeping the temperature constant at $5\,K$. These data are shown in **Figure 4.14a**. The peak emission of the FE exceeds that of the BE for fluences until $12\,\mu J/cm^2$. The time-integrated FE emission, however, is sublinear; on the contrary, the BE emission stays linear as presented in **Figure 4.14b**. This leads to the BE emission intensity exceeding the FE emission for all fluences above $12\,\mu J/cm^2$.

These observations based on excitations with various fluences can be explained by the low mobility of the BE as they are not able to move. The BE are significantly less affected by EEA than the FE which makes them more dominant for high excitation fluences. Furthermore, BE can be created from initially produced free charge carriers. BE cannot be exclusively produced by the FE state as this would necessitate that emission from both states decreases in the same manner. It is therefore likely that BEs are formed by the free charge carrier state. A free charge carrier can be trapped by a defect center and subsequently capture another charge carrier of the opposite charge thereby creating a BE. This formation of BE can be further increased by EEA in the following manner: After EEA one exciton returns to the ground state while the other reaches a highly excited, S_n, state that exceeds the energy of band edge free charge carriers. It may then dissociate into free charge carriers akin to those formed upon initial high-photon-energy excitation in a similar way as in organic semiconductors [129]. These free charge carriers can
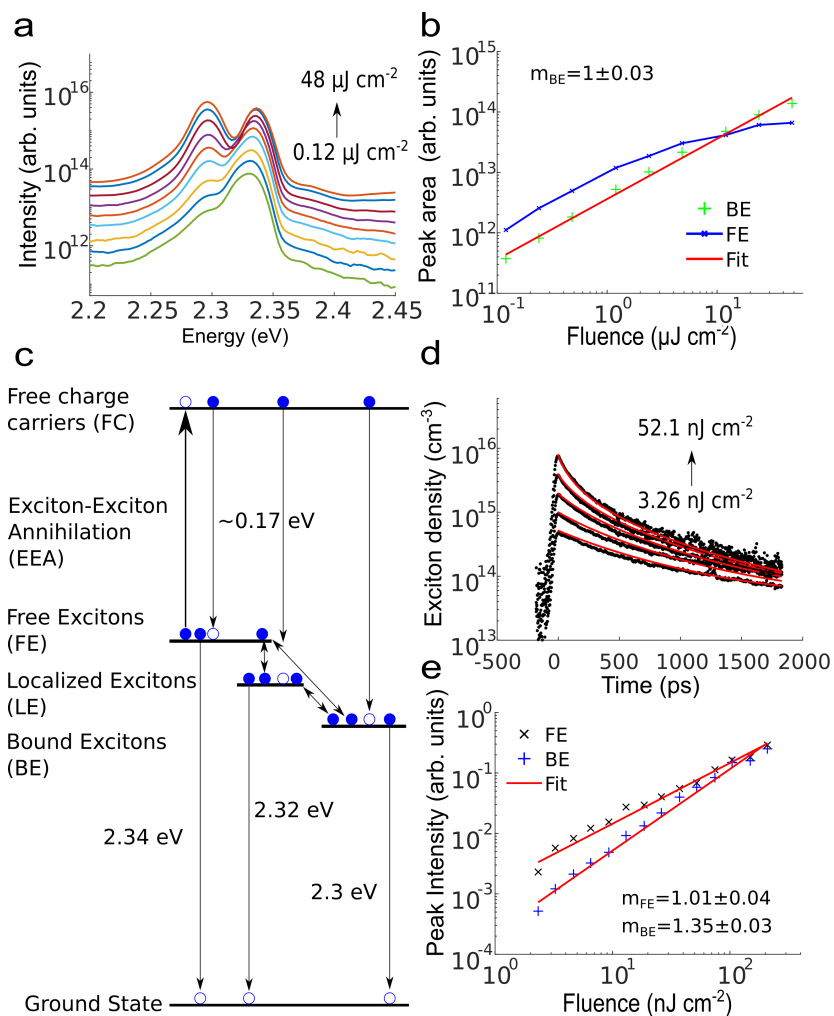
FIGURE 4.14: Fluence-dependence of PEPI (PEA$_2$PbI$_4$) under pulsed excitation (430 nm, 260 fs at 20 kHz) a) of the PL spectra and b) the peak area of the free exciton (FE) and bound exciton (BE) peaks. c) Schematic model of the photophysical pathways discussed in this work. d) Streak camera time-resolved PL transients of the FE emission at various excitation fluences (435 nm, 100 fs at 80 MHz). e) Maximum instantaneous intensity of the time-resolved PL transient for the FE and BE emissions. Adapted from [92], with the permission of AIP Publishing.

form BE again, thereby increasing the probability for BE to be formed shortly after excitation. The initial emission of BE should thereby increase superlinearly with fluence.

Figure 4.14c illustrates a schematic model to summarize the initial formation of free charge carriers, the formation of both FE and BE from free charge carriers, the rate of free to BE transition, the temperature-activated return of a BE to FE, and the fluence-dependent rate of EEA in the FE population leading at least partially to the recreation of free carriers. This model is sufficient to explain the key observations of this work.

To investigate the EEA in this material and how it affects the populations of FE and BE, the time-resolved PL dynamics are analyzed. A streak camera and a Ti:Sapphire oscillator based system (100 fs, 435 nm (second harmonic generated by lithium triborate crystal), 80 MHz) are used at a temperature of 77 K to allow for measurements with the necessary time resolution for the investigation of the FE dynamics over a range that also includes low enough pulse energies to monitor population decay before EEA becomes the dominant recombination pathway.

Some exemplary streak images at various excitation fluences are provided in **Figure 4.15**. By integrating over the wavelength range from 516 nm to 530 nm from these images for each excitation fluence the time-resolved PL intensity of the FE emission can be determined. These data are displayed in **Figure 4.14d**. The FE emission is mostly mono-exponential at the lowest fluences used here. As the excitation fluence increases, the decay becomes faster as a short-lived component becomes dominant. This is a typical sign of EEA taking place.

The population dynamics of the FE state are likely to involve several transitions forming an equilibrium with multiple other states. For simplicity the FE population can be approximated as described in **Section**
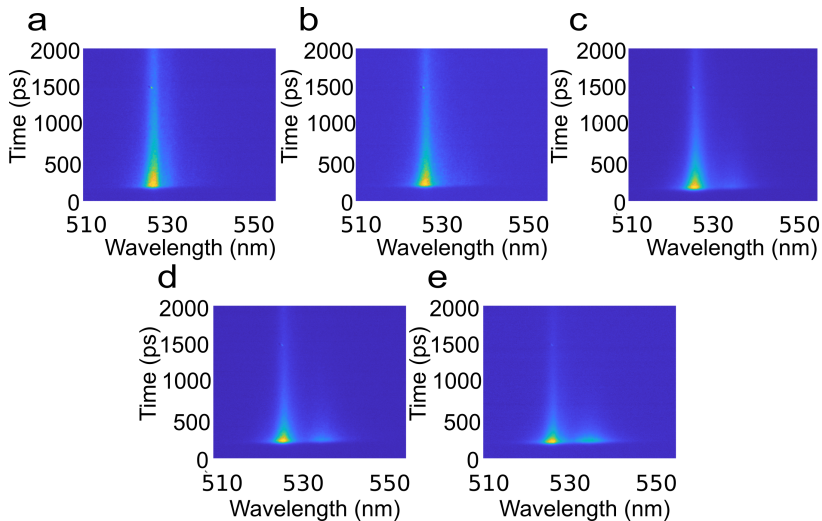
FIGURE 4.15: Exemplary streak images taken for the PEPI material at 77 K (435 nm, 100 fs) with a fluence of a) $3.2\,\mathrm{nJ\,cm^{-2}}$ b) $6.5\,\mathrm{nJ\,cm^{-2}}$ c) $13.1\,\mathrm{nJ\,cm^{-2}}$ d) $26.1\,\mathrm{nJ\,cm^{-2}}$ and e) $52.1\,\mathrm{nJ\,cm^{-2}}$. Adapted from [92], with the permission of AIP Publishing.

2.1.1 by $dn/dt = -k_1 n - k_2 n^2$. The analytical solution can then be used to globally fit the data displayed in **Figure 4.14d** [38]:

$$1/N(t) = [1/N(0) + k_2/k_1]exp(k_1 t) - k_2/k_1, \qquad (4.3)$$

where N is the exciton density and k_1 and k_2 are the respective mono- and bimolecular decay rates, and $N(0)$ is the initial exciton density. The monomolecular recombination rate can be estimated to be $k_1 = (1.42 \pm 0.03) \times 10^9\,\mathrm{s^{-1}}$. For the bimolecular rate, it is assumed that FE can annihilate with all excited states including the BE so that
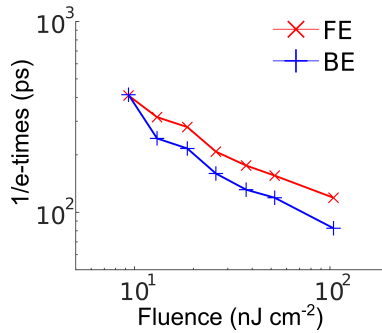
FIGURE 4.16: Fluence-dependent 1/e-times of the PEPI material for free (FE) and bound excitons (BE) at 77 K (435 nm, 100 fs). Adapted from [92], with the permission of AIP Publishing.

$N(0)$ can be approximated based on the total density of absorbed photons (38% in the 55 nm thick film). The resulting bimolecular rate is $k_2 = (1.4 \pm 0.1) \times 10^{-6}\,\mathrm{cm^3\,s^{-1}}$, or $(2.4 \pm 0.2) \times 10^{-1}\,\mathrm{cm^2\,s^{-1}}$ depending on whether volumetric or areal density is considered. The mono- and bimolecular rates that resulted from recent measurements in PEPI single crystals at room temperature were found to be considerably lower at $3.5 \times 10^7\,\mathrm{s^{-1}}$ and $(3.4 \pm 0.2) \times 10^{-4}\,\mathrm{cm^2\,s^{-1}}$ [130]. The material used in this work contains significantly smaller crystal areas relative to single crystals which leads to considerably higher nonradiative rates such as defect-related quenching, and increasing bimolecular rates due to the restriction of diffusion, thereby explaining the much faster rates [131].

For low fluences, the observed lifetimes of FE and BE were found to be identical as displayed in **Figure 4.16**. This is a clear indication that the above-stated conclusion of a formed equilibrium between the excited states is an important factor in determining the temperature-dependence of the FE population.

Even though the BE emission decays more quickly at high excitation fluences as is shown in **Figure 4.17**, its total contribution to the emission increases due to the superlinear increase in the instantaneous emission rate from the BE state (**Figure 4.14e**).
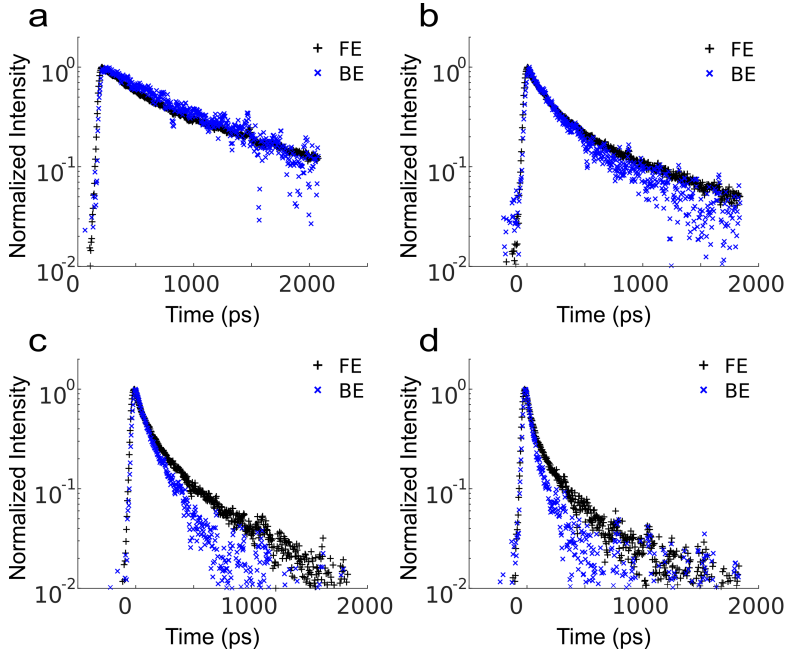
FIGURE 4.17: Comparison of the normalized decay of FE and BE emission of the PEPI material at 77 K (435 nm, 100 fs) with an excitation fluence of a) $13\,\mathrm{nJ\,cm^{-2}}$, b) $19\,\mathrm{nJ\,cm^{-2}}$, c) $104\,\mathrm{nJ\,cm^{-2}}$, and d) $209\,\mathrm{nJ\,cm^{-2}}$. Adapted from [92], with the permission of AIP Publishing.

The acquired data is consistent with the model presented above. BE can

be formed from free carriers. The increase in the formation rate visible in the streak data can be explained by an increase in EEA in the FE population which leads to a superlinear increase in the instantaneous emission. The BEs show a lower quantum yield which is likely due to a faster nonradiative recombination pathway. As the EEA in the FE becomes stronger, the BE are no longer in equilibrium; therefore the faster decay of the BE population is observable until the equilibrium is reestablished. It can be concluded that a temperature-dependent equilibrium between BE and FE and efficient EEA explain the variety of spectra that are observed from PEPI as a function of temperature and excited-state density.

4.3 Temperature dependence of PDMA PL under CW and pulsed excitation

The results for the Ruddelson-Popper PEPI material are now compared to the Dion-Jacobson perovskite utilizing PDMA as the spacer molecules. The results are presented in **Figure 4.18**.

At an initial glance, the spectra look very different with the broad emission around 2 eV with an FWHM of $\approx$350 meV at temperatures less than $\approx$70 K. This emission is just visible in the data from CW excitation but dominates the emission for the data gathered after pulsed excitation. As already explained above, this emission likely comes from surface defects of PbI_2 inclusions in the material. Additionally, the excitonic peak of these inclusions at 2.5 eV is also visible under pulsed excitation (**Figure 4.19**).

The emission peaks of the DJ-perovskite spectra can be fitted using three peaks again. However, they are not as distinguishable as the peaks in the RP-perovskite. A major difference is that the dominant BE emission is
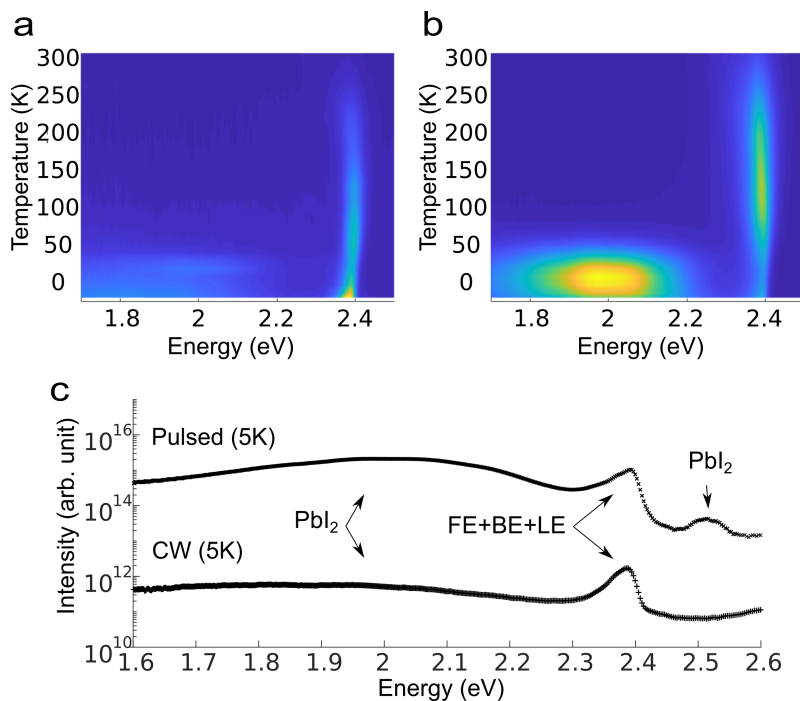
FIGURE 4.18: Temperature-dependent PL spectra for (PDMA)PbI$_4$ (Dion-Jacobson) for a) CW excitation (1.65 mW cm^{-2}, 405 nm), and b) pulsed excitation (48 μJ cm^{-2}, 430 nm, 260 fs). c) Comparison of CW and pulsed excitation at 5 K. Adapted from [92], with the permission of AIP Publishing.
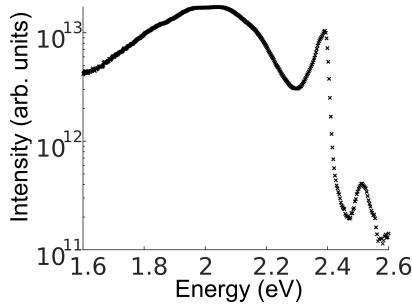
FIGURE 4.19: Emission of the DJ-perovskite (PDMA) at 5 K under pulsed excitation ($48\,\mu J\,cm^{-2}$, 430 nm). Adapted from [92], with the permission of AIP Publishing.

not observed even for the highest fluences used in this work. Furthermore, the FE peak increases monotonically in its intensity with decreasing temperature (**Figure 4.19a**) in contrast to the more nuanced behavior in the PEPI material. These observations are indicative of fewer BE states being present in the PDMA-based perovskite film. This causes the FE emission to be dominant under almost all conditions in this material.

In summary, the FE emission is dominant at room temperature similar to the PEA-based RP-perovskite. At temperatures below ≈ 70 K the FE is affected by EEA reducing the emission. The BE emission does not dominate the spectrum, it seems that the suppressed FE emission efficiency leads to the broad weak low-energy emission from PbI_2 becoming more dominant.

4.4 Discussion

The RP material that is analyzed here, PEPI (PEA_2PbI_4), is a benchmark 2D perovskite that has been scrutinized in the literature. As of yet, no clear consensus has been reached on the PL features, with similar low energy peaks being ascribed to biexcitons, triexcitons, BE, and phonon replica in various reports [22, 52–54, 110–115, 127, 132]. Biexcitons have been shown to exist, though at lower energies than the peaks that are observed and discussed here [114]. Two emission peaks in PEPI under intense pulsed excitation have been observed by Fujisawa *et al.* in 2004, where it was noted that the ratio between the low energy peak intensity and the high energy peak intensity increased with increasing excitation pulse fluence [52]. Thus they concluded that biexcitons are responsible for the low-energy emission peak at 2.31 eV and that the emission at 2.306 eV is due to amplified spontaneous emission from the biexcitons. A biexciton consists of two excitons that associate to form an energetically stabilized four-particle system. The formation probability of a biexciton and hence its emission intensity scales with the square of the excitation fluence. The higher energy peak at 2.35 eV was attributed to FE. The ratio between the low-energy peak and the high-energy peak shifted in favor of the low-energy peak at higher excitation fluences, although both were observed to depend sublinearly on the excitation fluence, thereby not following the linear and quadratic dependence on fluence expected for exciton and biexciton emission, respectively [52]. It was furthermore shown that doping the PEPI material with bismuth leads to an increase of the relative emission strength of the low-energy peak [52], which is consistent with the assignment of the low energy peak to BE.

The two emission peaks of PEPI at low temperatures were also observed

by Gauthron *et al.* in 2010 [110]. The peak positions were found at energies of 2.355 eV and 2.337 eV. It was concluded that the peaks originated from the same excited state (i.e. due to phonon-replica) as they observed that the intensities of the peaks scaled with the same power dependence under CW excitation, albeit over a limited range [110]. Furthermore, exciton localization – the trapping of excitons in a disorder potential – is discussed in their work which is in agreement with our findings.

The temperature and power dependence of the PEPI emission spectrum was revisited by Chong *et al.* in their work considering the challenges of achieving ASE in 2D perovskites [114]. Three peaks were observed, two at around 2.35 eV and 2.32 eV and an additional peak only visible for very high pulse fluences at low energy of 2.27 eV. This low energy peak was ascribed to biexcitons that are not seen up to the most intense pulsed excitation used in this chapter. The other peaks correspond to the FE and BE peaks in this work under strong excitation at low temperatures. The atypical change in the ratio between these two peaks can be explained by EEA reducing the FE emission for increasing excitation fluences. It could be considered unintuitive that the BE emission increases relative to the FE emission as it could be assumed that the BE sites become saturated at higher fluences. However, EEA is the more dominant effect overwhelming the contribution of site saturation reducing the BE emission while simultaneously aiding the formation of further BE.

4.5 Summary

In this chapter the PL of $(PEA)_2PbI_4$ (PEPI, an RP material) and $(PDMA)PbI_4$ (a DJ material) are studied. The temperature-, fluence-

and time-dependent photoluminescence spectra are analyzed to gain insight into the excited states in these materials.

The results for the $(PEA)_2PbI_4$ perovskite are understood in the following framework:

1. An equilibrium between free and bound/localized excitons is established. For temperatures above $\approx 140\,K$, the bound/localized excitons can easily dissociate to FE, so the emission is dominated by the FE. The increasing PL intensity with increasing temperatures from 50 to $140\,K$ support this hypothesis. The rising temperature causes a shift in the equilibrium favoring the FE rather than the BE population.

2. At temperatures below $\approx 100\,K$, the bound/localized exciton population becomes so strong that PL can be observed from these states.

3. EEA is suppressing the emission from FE at all temperatures under pulsed excitation. At temperatures below $\approx 100\,K$ the suppression of FE and the simultaneous enhancement of BE via EEA allows for BE emission to become the dominant emission in the spectra. Additional weak emissions from PbI_2 inclusions become well observable at these high excitation densities.

The DJ-perovskite, $(PDMA)PbI_4$, is much less affected by BE emission. FE emission is also suppressed by EEA at high excitation fluences, although not leading to dominant BE emission but rather to an increase in the relative dominance of emission from PbI_2 inclusions.

For an increase in the quantum efficiency in these materials at room temperature, the effective suppression of nonradiative recombination pathways is essential. Searching for spacer molecules with reduced vibrational degrees of freedom might be a beneficial development route.

At low temperatures, higher quantum efficiencies could be reached by understanding and eliminating sites supporting the BE state. PL spectroscopy at high fluences is also shown to be very sensitive to even small fractions of PbI$_2$ inclusions, especially at low temperatures, and could be used to guide efforts to further optimize the material quality.

5

Interpreting the Time-Resolved Photoluminescence of Quasi-2D Perovskites

Unlike in purely 2D-perovskites in which the exciton binding energy is high, quasi-2D perovskites do not only contain a single crystal size but rather a distribution of sizes. The optical excitation of these materials, therefore, leads to excited state populations of excitons, free charge carriers, or a mixture of both, depending on the type and amount of 2D spacer used. By carefully examining the fluence dependence of the following parameters after pulsed excitation, the mixture of the excited states can be determined:

1. Time-resolved photoluminescence (TRPL)

2. Photoluminescence quantum yield (PLQY)

3. Initial rate of photon emission (PL_0)

A simple model of non-interacting populations of excitons and charge carriers in separate sub-volumes of the film is sufficient to describe the observations made in this chapter. All of the unique features in the presented data, such as the anomalous peak of the PLQY at intermediate fluences, can be explained by this model. As the bimolecular free charge carrier emission gains efficiency with higher fluences,

the exciton-exciton annihilation reduces the exciton emission efficiency. In perovskite films made from high concentrations of butylamine (BA) spacers, the excited state population consists of 100% excitons which go down to approximately 7% excitons, and 93% free carriers for perovskites made with low concentrations of 1-naphthylmethylamine (1-Naphthylmethylamine (NMA)) spacer molecules. The effective bimolecular recombination rate of the free charge carriers and the exciton-exciton annihilation rate in these types of perovskites are high, often on the order of $1 \times 10^{-9} \, \text{cm}^3 \, \text{s}^{-1}$. The excited-state populations and their dynamics as well as their connection to applications and device engineering are discussed.

This chapter is based on my first-author publication *"Interpreting the Time-Resolved Photoluminescence of Quasi-2D Perovskites"* [133] in Advanced Materials Interfaces.

5.1 Motivation

As explained in **Section 2.2.3**, the quasi-2D perovskites are not phase-pure and consist of a distribution of different crystal thicknesses in the film. For the perovskites in this chapter, only spacers forming the Ruddlesden-Popper phase are investigated. Since 2D and quasi-2D perovskites can be considered quantum wells, a typical quasi-2D perovskite that is not phase-pure can be regarded as layered multiple-quantum-wells (MQW). MQW structures are typically more stable than their 3D counterparts while retaining a high quantum efficiency and color purity making them interesting for applications in the fields of photovoltaic and light-emitting applications [29, 32–42]. MQW quasi-2D perovskites based perovskite light-emitting diodes (PeLEDs) have reached external quantum efficiencies (EQE) of 20% [42] utilizing iodide at emission at 800 nm and over 15% utilizing bromide at emission at 520 nm [41].

For the successful engineering of devices, it is important to understand the photophysical properties of MQW structures. As described in **Section 2.2.3**, the thickness of a quantum well directly affects the band gap energy as well as the exciton binding energy [23, 49, 50, 134, 135]. The strong coulombic effects between charge carriers in strongly confined quantum wells increase the absorption coefficient of the free charge carrier (FC) state [85]. Photoexcitation far above the band gap energy should therefore lead to strong absorption from small and strongly confined QWs. The funneling leads to a quick transfer of excited states from thin to thick QWs [24, 33–35]. The emission from quasi-2D perovskite films can be due to excitons, FC recombination, or indeed a mixture of both, as will be shown in this chapter. A simple model is proposed to account for this transition and the mixed nature of the excited-state population in quasi-2D perovskite films. The excited states are funneled towards the local band gap minima in the film. The thickness of these local minima determines whether the excited states are excitonic or FCs. If the thickness of all the minima QWs is below a critical value, the exciton binding is too strong to allow for exciton dissociation into FCs and excitons are the dominant emitting species. If all the minima QWs are thicker than the critical value, the exciton binding energy can be overcome and FCs are the dominant emitting species. If some minima are below the critical thickness and some are above then the photoluminescence is a mixture of dominant exciton emission from some subset of QWs and dominant FC emission from another subset of QWs. A schematic of the proposed photophysical mechanisms is illustrated in **Figure 5.1** and **Figure 5.2**. All experimental data on the varying 2D spacers and their concentrations collected in this chapter can be described consistently and with reasonable accuracy by this simple model considering only two non-interacting pools of excited states.

The analysis presented here is based on the fluence dependence of three
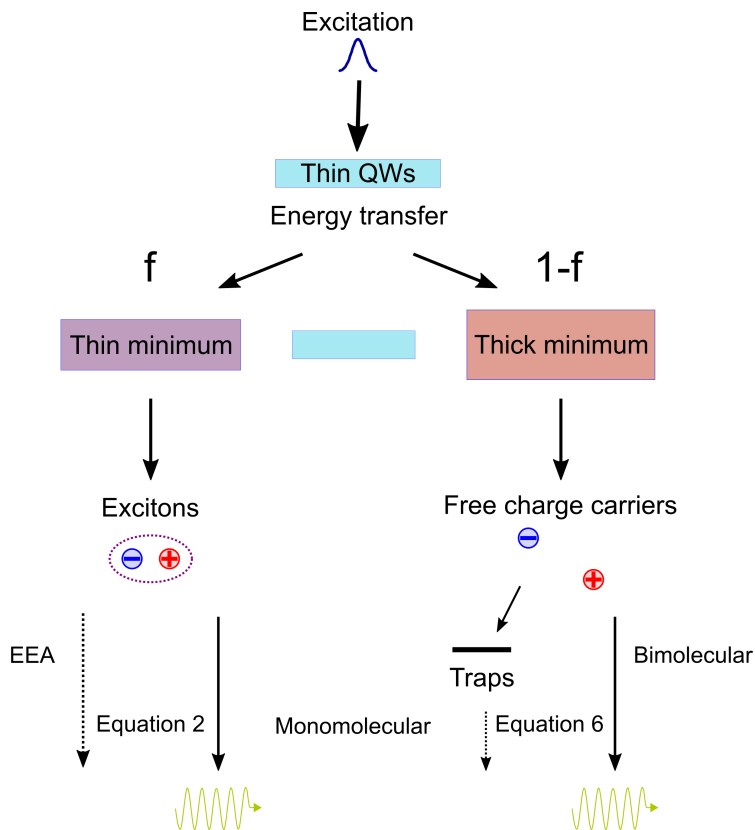
FIGURE 5.1: Schematic representation of how the excited states in a quasi-2D perovskite film responsible for emission can either be excitons, free charge carriers, or a combination of both. Here, f is the fraction of excitonic PL. Reproduced from [133].
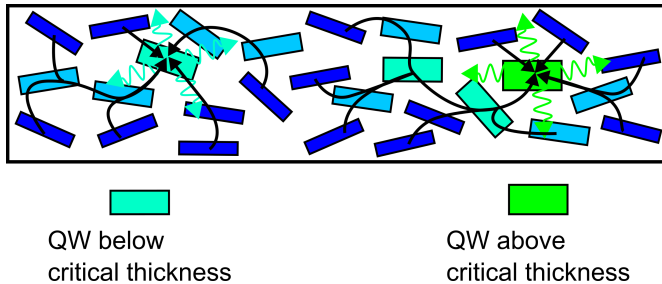
FIGURE 5.2: Schematic illustrating the funneling process of excitons and free carriers into differently sized quantum wells above and below a critical thickness and separated by thin quantum wells prohibiting energy or charge transport between the two pools of radiatively emitting excited states. Reproduced from [133].

observables after pulsed excitation which are: The photoluminescence (PL) decay kinetics, the initial rate of emission (PL$_0$), and the photoluminescence quantum efficiency (PLQY). In this chapter, first, the fluence-dependence of the three mentioned observables is simulated using rate equations and compared for systems supporting either only excitons or only FCs. Then the gathered experimental data for perovskites based on either n-butylamine (BA) or 1-naphthylmethylamine (NMA) spacers with the most distinct differences are analyzed and compared to the previously described simulations indicating purely excitonic PL and PL based solely on FCs in the respective sample films. The sample fabrication is described in **Section 3.1**. The perovskites have the formula CsPbBr$_3$(NMA or BABr)$_y$ where y is varied from 0.4 to 1.0. After establishing the different excited states present in these films the changes in the time-resolved photoluminescence (TRPL) with changing spacer concentrations are displayed for the BA-based perovskites. It is shown that FC recombination begins to play a measurable role alongside the excitonic emission as the concentration is reduced. The same analysis

of the NMA-based perovskites shows that the increase in PL_0 becomes increasingly less quadratic for an increase in spacer concentration despite the PL dynamics being dominated by FC emission. This, however, can not be attributed to an increase in excitonic emission; therefore, it is likely that in this case, exciton-exciton annihilation (EEA) during the funneling processes reduces the initial excited-state density in the band gap minima QWs. At last, the limitations of this and the future challenges that need to be overcome to understand the TRPL transients from quasi-2D perovskites are discussed. Additionally, the impact of this understanding concerning device engineering is investigated.

5.2 Simulation: Excitonic vs. free charge carrier PL

In this section, the model to describe the photoluminescence in quasi-2D perovskites is introduced. This model consisting of two non-interacting pools of excitons and FCs will be used in the following sections to interpret the experimental data. The excited states are funneled into separate regions in the perovskite film due to the inhomogeneity of the local band gap minima QWs. An alternative model considering the transition between excitons and FCs in a more homogenous perovskite film does not explain the displayed observations. The emission at long times and therefore at low excited state densities seem to come primarily from excitons. However, as described in **Section 2.1.2** low excitation densities typically result in the dominance of FCs as opposed to excitons. A shift in the spectrum supporting this transition from excitons to FCs is not observed. It is not suggested that the simplistic model proposed in this chapter covers all photophysical processes, however, it is the most simple model to describe and reproduce all salient features of the gathered

dataset accurately and as such has utility in beginning the interpretation of PL dynamics in quasi-2D perovskites.

As already introduced, the absorption in thin QWs is stronger due to the strong coulombic enhancement of the continuum absorption in these QWs with high exciton binding energies [85]. The excited states in thin QWs after the optical excitation likely consist mainly of excitons. These funnel towards larger quantum wells until they reach a local band gap minimum. These minima are separated by higher band gap material so that no transport between the local-minima QWs is possible. If the band gap minima are below a critical thickness which might depend on the spacer molecule involved in the perovskite fabrication, the excitons remain stable and the emission is based on the recombination of excitons. If the minima are, however, thicker than the critical thickness the excitons dissociate and the resulting emission dynamics in these QWs will be dominated by FC recombination. This mechanism is also described in **Figure 5.1**.

As introduced in **Section 2.1.1**, the exciton density can be described as:

$$\frac{dn_x}{dt} = G_x - k_x n_x - \gamma_{EEA}(t) n_x^2, \tag{5.1}$$

where k_x is the total monomolecular rate constant including radiative and non-radiative contributions, $k_x = k_{x,rad} + k_{x,nrad}$ and γ_{EEA} is the rate constant for bimolecular EEA.

In a quasi-2D perovskite, the excitons can diffuse without constraint, so that the EEA rate can be considered constant with $\gamma_{EEA} = 8\pi DR_{crit}$, related to the exciton's diffusion coefficient, D, and the radius at which two excitons interact, R_{crit}. For the displayed simulations in **Figure 5.3** $\gamma_{EEA} = 2.5 \times 10^{-9} \, \text{cm}^3 \, \text{s}^{-1}$ is used based on the recent literature [130]. For the monomolecular lifetime a value of $k_x = 1.25 \times 10^7 \, \text{s}^{-1}$ is chosen
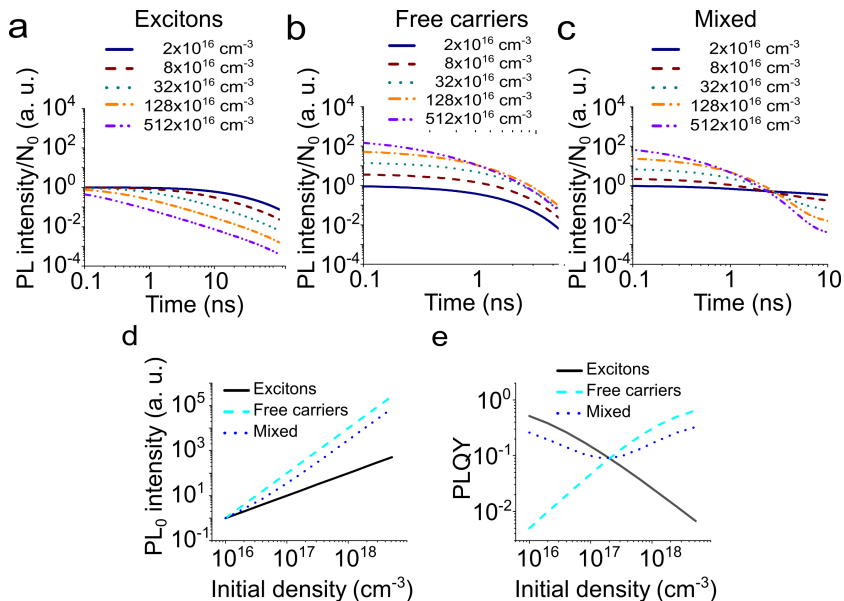
FIGURE 5.3: Simulations to illustrate the PL kinetics divided by the initial excited-state density N_0 of a) excitons, b) free carriers (FCs), and c) a 50/50 mixture ($f = 0.5$) of exciton and FC PL. Simulations of d) the PL_0 and e) PL efficiency of excitons, FCs, and a 50/50 PL mixture dependent on excitation fluence. Adapted from [133].

as this lifetime is similar to those typically measured in quasi-2D perovskites based on phenethylamine (PEA) or BA ligands with high 2D spacer content [130].

In TRPL measurement with a streak camera, the number of photons arriving in a given time window is collected. This number of photons after excitation gives the rate of PL photon emission at that time; i.e., the number of photons emitted divided by the length of the time window is the rate of photon emission at a given time delay after excitation.

From **Equation 5.1** the time-dependent PL emission of excitons can be derived:

$$PL_x(t) = k_{x,rad} n_x(t) = k_x \left(\frac{k_{x,rad}}{k_{x,rad} + k_{x,nrad}} \right) n_x(t)$$

$$= k_x \phi \frac{k_x}{\gamma_{EEA}(exp(k_x t) - 1) + \frac{k_x}{N_0} exp(k_x t)},$$

(5.2)

where ϕ is the radiative fraction of the total decay. For excitons the emitted PL at a given time is directly proportional to the excited-state density. As shown in **Equation 5.2** the excitons density $n_x(t)$ can be derived by integrating **Equation 5.1**, where N_0 is the initial exciton density. This initial density in the QW band gap minima cannot be easily accessed. The volume fraction of the minima QWs cannot be determined without an advanced setup. Since the excited-states funnel into the QW minima and since the volume fraction is unknown, the initial density of excitons cannot be known either. The initial density N_0 will therefore be estimated as the average density of excited states created inside the film as calculated from the excitation fluence, sample absorbance, and film thickness. The actual density N_0 is likely higher than that. This leads to the extracted bimolecular rates being effective parameters rather than the physical parameters from the QWs. As N_0 is underestimated, the actual values for γ_{EEA} are overestimated. If the real densities inside the emitting QWs could be determined, then so could the actual values for γ_{EEA}. This is a general challenge to the interpretation of TRPL transients in these quasi-2D systems due to the funneling process and will be discussed further below. It needs to be mentioned that with **Equation 5.2**, the exciton transport between energy-minima QWs is possible, whereas in the physical model that is not the case. However, as long as the initial densities of excitons in the QW-minima are high—which must be

the case for EEA to be observed—there should not be any differences observable. Taking the role of finite domain sizes into account would necessitate additional parameters such as the domain size, which is not possible to constrain from the current data, therefore a more nuanced model can only be introduced once additional data can be gathered. In this first step analysis, the inaccuracy introduced by this equation allowing transport between all QWs supporting excitons needs to be noted but the analysis will prove the model as presented to be sufficient in approximating the physical processes.

After the initial excitation and under the assumption that no EEA has occurred the initial PL_0 is:

$$PL_x(0) = k_x \phi N_0 \tag{5.3}$$

It is clear from **Equation 5.3** that the initial excitonic PL, PL_0 scales linearly with the initial excited-state density N_0 and thereby the excitation fluence assuming no changes in the absorption. This is, however, only true if EEA in the instrument response time can be neglected. If there is EEA in the instrument response, the resulting TRPL curve is the convolution of the instrument response function and the PL dynamics, which effectively causes a decrease in the measured maximum PL intensity, PL_0. In this case, the maximum PL can be approximated as $PL_{I.R.} = PL(t_D)$, the PL after a delay t_D, which is roughly half the instrument response time.

The third mentioned observable, the PLQY of the excitonic emission is the number of emitted photons divided by the number of initial excitations. The number of photons is the integral of **Equation 5.2**:

$$PLQY_x = \frac{\int_0^\infty k_{x,rad} n_x(t) \, dt}{N_0} = \phi \frac{-k_x}{\gamma N_0} \ln\left(\frac{k_x}{k_x + \gamma N_0}\right) \tag{5.4}$$

FIGURE 5.4: Exciton PLQY simulated based on **Equation 5.4** and approximation both using the same parameters as **Figure 5.3**. Reproduced from [133].

The limits **Equation 5.4** poses are when $N_0 \rightarrow 0$ then $PLQY_x \rightarrow \phi$ and when $N_0 \rightarrow \infty$ then $PLQY_x \rightarrow 0$. For small initial densities, the linear processes are the dominant recombination pathway which means the PLQY is determined by the relative strength of the radiative rate to the nonradiative rate, ϕ. For higher initial densities the nonradiative bimolecular EEA becomes the dominant pathway reducing that efficiency. It should be noted that this agrees with a simplified approximation for the PLQY using the estimation that the rate of annihilation stays at its maximum rate throughout the decay. This leads to the simplified equation $PLQY = \phi \frac{k_x}{k_x + \gamma N_0}$ which underestimates the actual PLQY due to the exaggeration of the bimolecular recombination pathway. This simple approximation and the PLQY calculated via **Equation 5.4** are compared in **Figure 5.4**.

If instead of excitons the optical excitation leads to FCs, the TRPL, PL_0 and the PLQY all have different fluence-dependence. Assuming the investigated perovskite is an intrinsic semiconductor, i.e. the number of

generated electrons in the conduction band will be equal to the number of generated electrons, then the density of electrons in the conduction band can be described by (see also **Section 2.1.2**):

$$\frac{dn_c}{dt} = -k_{1,c}n_c - k_{2,c}n_c^2,$$ (5.5)

where n_c is the electron density, $k_{1,c}$ is the rate of monomolecular non-radiative loss due to charge-trapping, and $k_{2,c}$ is the bimolecular rate of electron-hole recombination leading to photon emission. Auger recombination is not considered as the fluence range is below the excitation densities leading to third-order effects.

The time-dependent photon emission rate for the FCs can be described by:

$$PL_c(t) = k_{2,c}n_c(t)^2 = k_{2,c}\left(\frac{k_{1,c}}{k_{2,c}(exp(k_{1,c}t) - 1) + \frac{k_{1,c}}{N_0}exp(k_{1,c}t)}\right),$$ (5.6)

where N_0 is the initial density of electrons within the band gap minima QWs that support FCs. Again, similar to the case of excitons, the actual density inside the band gap minima QWs is unknown and not possible to be determined without knowledge of the volume fraction making up the minima QWs. The bimolecular rate $k_{2,c}$ is again an effective rate that is higher than the actual rate.

The initial PL emission can be easily formulated based on **Equation 5.6**:

$$PL_c(0) = k_{2,c}N_0^2$$ (5.7)

The initial PL emission, therefore, scales with the square of the initial FC density and equivalently with the excitation fluence.

At last, the PLQY from FC emission is described by:

$$PLQY_c = \frac{\int_0^\infty k_{2,c}n_c(t)^2\,dt}{N_0} = \frac{k_{2,c}N_0 + k_{1,c}\ln\left(\frac{k_{1,c}}{k_{1,c}+k_{2,c}N_0}\right)}{k_{2,c}N_0} \qquad (5.8)$$

The limits of the FC PLQY described in **Equation 5.8** are when $N_0 \to 0$ then $PLQY_c \to 0$ and when $N_0 \to \infty$ then $PLQY_c \to 1$. This means that as long as trapping processes are the dominant recombination factor, the PLQY will be negligible. As the radiative bimolecular recombination channel becomes stronger, the PLQY increases. If the bimolecular pathway is dominant and without the presents of third-order processes, the PLQY will move towards unity. Similar to the case of excitons the PLQY of FC emission can be approximated by assuming that the bimolecular recombination maintains its initial rate throughout the whole decay. This would result in $PLQY = \frac{k_{2,c}N_0}{k_{2,c}N_0+k_{1,c}}$ which overestimates the efficiency due to the exaggeration of the role of bimolecular decay. A comparison of the PLQY as a function of fluence for **Equation 5.8** and the simplification is presented in **Equation 5.5**.

At last, a mixture of excitonic PL and PL based on FC recombination coming from noninteracting populations can be expressed by combining the already established equations. From **Equation 5.2** and **Equation 5.6** using f as the fraction of the band gap minima QWs that support excitons:

$$PL = fPL_x + (1-f)PL_c \qquad (5.9)$$

From **Equation 5.3** and **Equation 5.7** it follows consequently:

$$PL(0) = fPL_x(0) + (1-f)PL_c(0) \qquad (5.10)$$

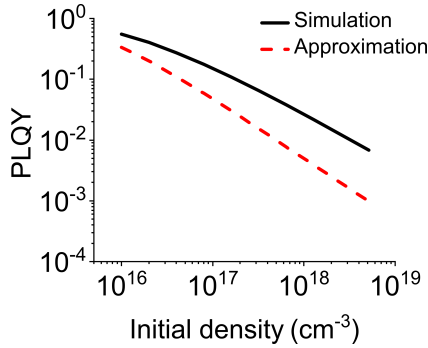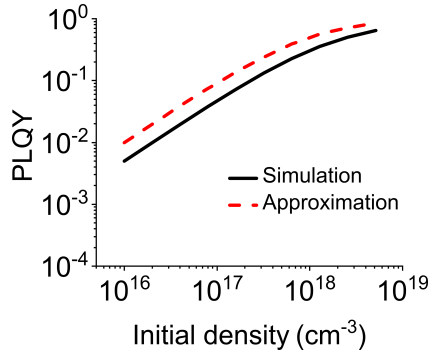FIGURE 5.5: Free charge carrier PLQY simulated based on **Equation 5.8** and approximation both using the same parameters as **Figure 5.3**. Reproduced from [133].

And from **Equation 5.4** and **Equation 5.8**:

$$PLQY = f PLQY_x + (1-f)PLQY_c \qquad (5.11)$$

The initial excited-state density N_0 will be the same for both the excitonic and the FC-based states irrespective of f. Once all states have funneled into the band gap minima, the density will be the same; however, the comments above about the underestimation of N_0 based on the total film volume still apply. With the now established scaling of the PL dynamics, the initial PL at zero-time and the PLQY with the initial excited-state density for the respective populations of excitons and FC, the different characteristics are compared in **Figure 5.3** for some exemplary parameters. For the exciton decay, no nonradiative monomolecular recombination is assumed. The value chosen for the monomolecular rate constant is $1.25 \times 10^7 \text{ s}^{-1}$ based on Delport et al. [109]. The rate of EEA is also chosen by Delport et al. at a value of $2.5 \times 10^{-9} \text{ cm}^3 \text{ s}^{-1}$ which is equivalent to a 100 nm film thickness at the rate of $2.5 \times 10^{-4} \text{ cm}^2 \text{ s}^{-1}$

published in their work [109]. For the illustration of the free charge carrier-based dynamics values close to those acquired below for $NMA_{0.4}$ are chosen: $k_{1,c} = 5 \times 10^8\,\mathrm{s}^{-1}$ and $k_{2,c} = 5 \times 10^{-10}\,\mathrm{cm}^3\,\mathrm{s}^{-1}$. For the simulation, the initial densities of the excited states are varied between $1 \times 10^{16}\,\mathrm{cm}^{-3}$ to $5 \times 10^{18}\,\mathrm{cm}^{-3}$, which for a 100 nm thick film absorbing 30% of the incident photons at a wavelength of 350 nm corresponds to excitation fluences of approximately $0.2\,\mu\mathrm{J\,cm}^{-2}$ to $95\,\mu\mathrm{J\,cm}^{-2}$.

In **Figure 5.3a**, **b**, and **c** the TRPL intensity is divided by the initial density of excited states for the three cases of mainly excitons, free charge carriers, and a mixture of the two. This corresponds to **Equation 5.2**, **5.6**, and **5.9** divided by N_0 in each equation. Dividing the equations by the initial excited-state density poses an advantage over plotting the PL by illustrating the clear differences between the excited states and thereby allowing for the simple distinguishment of the features of excitonic and FC-based emission. If the TRPL curves were normalized to their respective maximum values, the shortening of the lifetime could be observed as well; however, the change in the lifetime might look similar for both excitonic and free charge carrier emission (as illustrated in **Figure 5.6**). The two cases look very different if the TRPL is normalized by the initial excited-state density. For exciton-dominated emission, the normalized TRPL curves all start from the same point, given that there is no higher-order decay in the instrument response time of the system. At low excitation fluences, the curves lie on top of each other as EEA does not affect the decay kinetics. The PL efficiencies of the curves acquired under low excitation are the same (**Figure 5.3e**). In the case of FC-dominated emission, the TRPL curves normalized by the initial excited-state densities do not start at the same point. The quadratic scaling of the initial PL with the excited state density leads to the PL curves starting at higher values which leads to the curves being offset from each other. The initial emission rate is illustrated in **Figure 5.3d** and
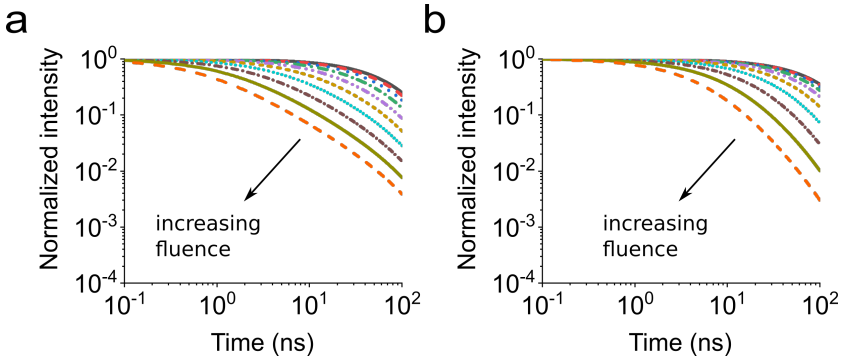
FIGURE 5.6: Comparison of simulated normalized PL dynamics in a) excitons and b) free charge carriers. The rates used in this illustration are chosen to lead to similar PL dynamics and are $k_x = 1.25 \times 10^7\,\mathrm{s}^{-1}$; $\gamma_{EEA} = 2.5 \times 10^{-10}\,\mathrm{cm}^3\,\mathrm{s}^{-1}$; $k_1 = 0.5 \times 10^7\,\mathrm{s}^{-1}$; $k_2 = 0.25 \times 10^{-10}\,\mathrm{cm}^3\,\mathrm{s}^{-1}$. Reproduced from [133].

e alongside the PLQY of each of the two cases. The initial PL (PL$_0$) shows different power-law slopes over the excitation fluence on a log-log scale. While the slope for excitons is one, the slope of the initial PL for free charge carriers is two. The PLQY of the FC emission increases monotonically with excitation fluence while the exciton PLQY decreases monotonically. Now that the differences between excitonic and FC emissions have been examined and can easily be distinguished, the more complex case of two pools of excited states supporting both excitons and FCs in different subvolumes of the film is considered. The case of an even split between excitons and FCs so at $f = 0.5$, where the TRPL intensity divided by N_0 is shown in **Figure 5.3c**. The initial PL increases with increasing excitation fluences; however, the curves do not spread to the same extent as for pure FC emission. Interestingly, there is a very distinct region shortly after the excitation where the TRPL curves

cross, with the curves corresponding to higher excitation fluences moving from above to below curves of lower excitation fluences as time progresses. This behavior is not observed for purely excitonic emission. It can be observed for FC emission at high excitation fluences, however not nearly as dominant as in the experimental data analyzed below. The slope of the initial PL on a log-log scale with the excitation fluence is below two for lower fluences and moves towards two for higher fluences as displayed in **Figure 5.3d**. This is indicative of the low fluence PL being dominant due to the linear dependence on the excited state density. For higher excitation fluences, the PL becomes dominated by FC recombination. This change in the dominant excited state recombination for PL emission is even more pronounced in the PLQY which does not exhibit a monotonic trend on the fluence as illustrated in **Figure 5.3e**. Here, the PLQY first decreases due to EEA affecting the dominant exciton recombination efficiency. As the fluence increases, the bimolecular recombination of FCs becomes the dominant emission species and the PLQY starts to increase again. It is equally possible with different rate constants that the PLQY would first increase due to the efficiency increase in the FC emission and subsequently a drop due to EEA reducing the emission efficiency of excitons.

5.3 Experimental observations of exciton- and FC-dominated PL

The amplified spontaneous emission (ASE) thresholds of quasi-2D perovskites as a function of 2D spacer and content were examined in collaboration with Li et al. [47]. The thresholds found for materials that exhibited an exciton-like emission in the analysis of PL_0 were considerably higher than those found in materials with more FC-based recombination characteristics. In this chapter the same series of quasi-2D materials

made from varying fractions of BA or NMA 2D-spacers is examined again to analyze the photophysics in more detail and to gain an understanding of the excited-states present in the film and how their recombination pathways affect the TRPL. The two samples which show the most analogous characteristics to pure excitonic emission and pure FC-based emission are considered in **Figure 5.7**; these are the perovskite with $y = 0.4$ NMA spacer ($NMA_{0.4}$) and the perovskite with $y = 1.0$ BA spacer ($BA_{1.0}$) respectively. In **Figure 5.7a** the TRPL dynamics for $BA_{1.0}$ divided by the initial excited-state density are presented. It is assumed that the initial excited-state density is proportional to the excitation fluence. The data is additionally divided by the maximum PL of the lowest fluence which leads to the initial point of the lowest fluence TRPL being one. This helps the clarity of the presentation. For all further datasets, the same method will be used to aid the comparisons. The data is presented on a log-log scale therefore the maximum PL is assigned to a time above zero, namely 1.1 ns so that the full dynamics can be displayed. This will be done for all further BA-based perovskite samples. Fluences ranging from $0.5 \, \mu J \, cm^{-2}$ to $11 \, \mu J \, cm^{-2}$ lead to an increasingly faster PL decay with fluence. For fluences above $5 \, \mu J \, cm^{-2}$ additionally to the faster decay, the initial points of the TRPL start to drop relative to lower fluences as well. This effect is further illustrated in **Figure 5.7c**, where the initial PL_0 starts to scale sublinearly rather than linearly with fluence. This deviation from the simulation shown in **Figure 5.6** is simply a result of the finite instrument response of the used streak camera setup (At the time range used the instrument response is approximately 1 ns) since EEA occurs within the instrument response time. The measured PL is made up of the real decay kinetics convoluted with the instrument response. This leads to EEA effectively lowering the measured signal at high fluences which results in the sublinear scaling of PL_0. The opposite behavior is to be expected for FC involvement in the emission, as the initial points at higher fluences will always be
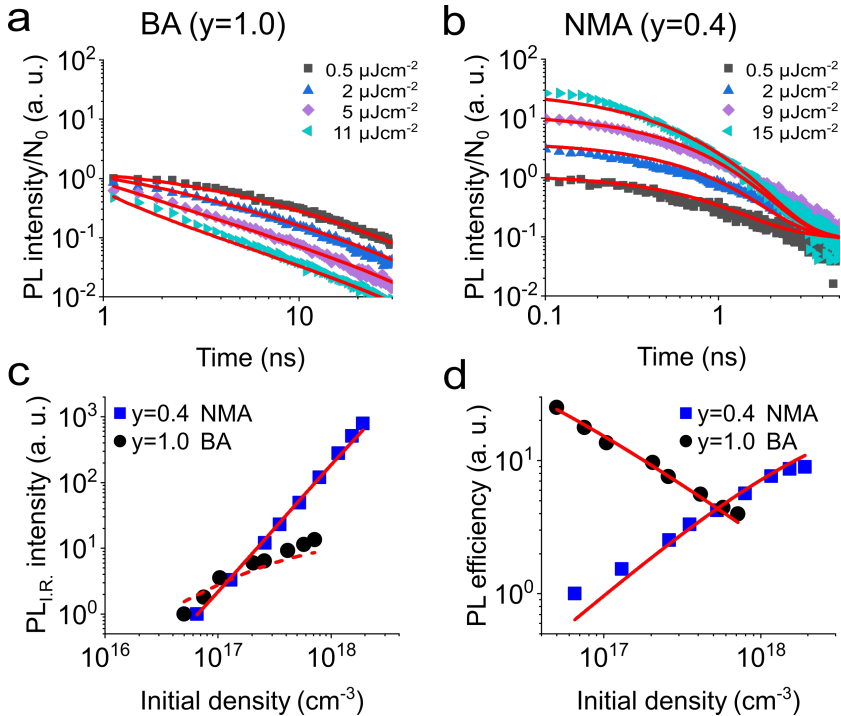
FIGURE 5.7: Time-resolved PL dynamics divided by the initial excited-state density for the a) $BA_{1.0}$ perovskite and b) $NMA_{0.4}$ perovskite at different fluences and fitted with **Equation 5.2** and **Equation 5.9** divided by N_0 respectively. c) $PL_{I.R.}$ (I.R. stands for the instrument response) fitted with **Equation 5.2** and **Equation 5.9** and d) PL efficiency of the $NMA_{0.4}$ and the $BA_{1.0}$ perovskites fitted with **Equation 5.4** and **Equation 5.11** respectively utilizing the same parameters as in a) and b). Reproduced from [133].

above the initial points of lower fluence TRPL curves. As introduced above, the PL values are interpreted as the PL shortly after zero-time. The zero-time is assumed to be roughly half the instrument response (0.68 ns) before the maximum PL signal at 1.1 ns for our model. So instead of using **Equation 5.3** to model PL_0 which is only possible for very short instrument response times relative to the decay lifetimes, the modeled emission rate at the delay time corresponding to the PL maximum in the measured data is used. Taking the finite instrument response into account rather than using PL_0, an "effective" version of PL_0 is used, which is labeled as $PL_{I.R.}$ for the sake of clarity. As shown in **Figure 5.7a** and **c** accounting for the instrument response allows for a good estimation of the TRPL dynamics and the slope of $PL_{I.R.}$. Looking at **Figure 5.7d**, the monotonic decrease of the PLQY with increasing excitation fluences can be observed for $BA_{1.0}$. These observations are all in complete accordance with the expectations based on the simulations of the excitonic decay. The data are fitted with **Equation 5.2** (normalized by N_0). In **Figure 5.7a** it is demonstrated how the model which only considers excitons fits the data very well over almost two orders of magnitude. The rate constants extracted from the fitting are: $k_x = 2.7 \times 10^7 \, s^{-1}$ and $\gamma_{EEA} = 6 \times 10^{-9} \, cm^3 \, s^{-1}$. As discussed above, the rate constant for EEA is considered to be an effective rate. The real rate of EEA should be lower as the exciton density inside the emitting QWs is higher. However, the encounter and annihilation rates remain the same since they result from the product of the density with the rate constant; i.e. the effective rate is higher while the uniformly distributed density is lower and the real rate is lower while the real density inside the QWs is higher. Additionally to the TRPL data, both the PL efficiency and the PL_0 are well reproduced with the same parameters as displayed in **Figure 5.7d**.

Now, turning toward the data for the $NMA_{0.4}$ perovskite shown in **Figure 5.7b**, a clear increase in PL_0 divided by N_0 can be observed as the excitation fluence increases. Since the TRPL of the NMA perovskites is much shorter lived, the maximum of the PL was chosen to be at 0.1 ns for all the NMA data to ease the visualization on a log-log scale. As demonstrated in **Figure 5.7c**, the slope of PL_0 is almost exactly two, indicating that the recombination of FCs dominates the PL at early times. The monotonically increasing efficiency with increasing excitation fluence shown in **Figure 5.7d** further confirms this assessment of FC-dominated PL. The PL characteristics of the $NMA_{0.4}$-perovskite are in stark contrast to the $BA_{1.0}$-perovskite sample which shows that the dominant excited-state species strongly depends on the material.

To fit the long tail in the TRPL data of the $NMA_{0.4}$-perovskite, it is necessary to include a small contribution from excitonic PL in **Figure 5.7b**. As mentioned above the NMA sample exhibits a shorter PL lifetime, therefore the axis of the two samples are different. It is therefore estimated that the long-lived component in the mainly FC-dominated dynamics of the NMA-based perovskite is due to excitons that remain after the FCs have decayed. The dynamics of the $NMA_{0.4}$-based perovskite are therefore modeled utilizing **Equation 5.9**. This results in a fraction of 93% of FCs and 7% of excitons. In this estimation for simplicity's sake, no nonradiative monomolecular exciton decay is assumed. The exciton emission is thereby overestimated. The extracted rate constants for the FC decay are $k_1 = 7.4 \times 10^8 \, s^{-1}$ and $k_2 = 4.7 \times 10^{-10} \, cm^3 \, s^{-1}$. Again, k_2 is an effective rate constant with the real one being likely considerably lower since the true N_0 is much higher in the emitting QWs. While the real density cannot be easily assessed, the recombination rate, i.e. the product of density and rate constant, can be accurately determined. The trapping rate, k_1, of the FCs is very fast with a lifetime of only 1.35 ns, which is consistent with the fast TRPL decay

at low excitation fluences. Efficient FC emission occurs when $N_0 > \frac{k_1}{k_2} =$
$1.6 \times 10^{18}\,\mathrm{cm}^{-3}$, which is a very high density. These results are consistent with the increasing efficiency of the PL even at these considerably high excitation densities illustrated in **Figure 5.7d** wherein the extracted parameters from the TRPL data fit the PLQY as a function of excitation fluence well. The extracted rates for the small fraction of excitonic emission are $k_x = 6 \times 10^7\,\mathrm{s}^{-1}$ which is about twice as high as for the BA-based perovskite, although still in reasonable agreement. The EEA could not be a reasonable fit due to its low influence on the decay dynamics due to the low fraction of excitons. The rate constant γ_{EEA} was, therefore, constraint to be zero for this case. The extracted parameters are all summarized in **Table 5.1**.

To summarize, in this section the clear differences in the PL emission of the $BA_{1.0}$- and the $NMA_{0.4}$-perovskites are analyzed with the PL characteristics of the former being due to the recombination of excitons and the emission behavior of the latter mainly being attributed to FC recombination. The differences in the PL emission depending on the spacer material have a large impact on the understanding and engineering of perovskite-based devices. Despite both materials being quasi-2D perovskites, they must be considered completely different in regards to the excited-state dynamics and their use in device engineering.

5.4 Alteration of the excited-state population with BA concentration

In the previous section, it was established that the dominant excited-state species and therefore the PL dynamics in quasi-2D perovskites are strongly dependent on the nature of the used 2D spacer. In this section,

the influence of the spacer concentration in the perovskite precursor on the excited-state species is examined.

The PL dynamics dependent on the concentration of the BA spacer molecules in the perovskite film are displayed in **Figure 5.8a**. For high contents of BA ($BA_{1.0}$, $BA_{0.8}$) the initial points of the TRPL data normalized by the initial excited-state density N_0 stay the same or decrease with increasing excitation fluence, which, as explained above, is due to EEA in the instrument response time. This PL behavior is a clear sign that the excited-state population is dominated by excitons. For lower concentrations of BA spacer molecules ($BA_{0.6}$, $BA_{0.4}$) the initial points of the TRPL curves normalized by N_0 increase with increasing excitation fluence, which indicates the involvement of FC emission in these materials. Additionally, the curves corresponding to different excitation fluences illustrated in **Figure 5.8a** show a pronounced crossing behavior with the higher excitation fluence curves starting above and ending below lower fluence curves. TRPL curves based purely on excitonic emission do not cross at all, while pure FC emission shows much more subtle crossing behavior at very high excitation fluences. Thus, the observation of crossing TRPL curves is evidence that as the BA content is decreased and therefore the emitting QWs grow larger on average, the excited state population responsible for the PL characteristics shifts from exciton-dominated towards a mixture of excitons and FCs. This is direct evidence that the nature of the excited-state populations in quasi-2D perovskites not only depends on the chosen spacer molecule but also on its concentration in the perovskite precursor and therefore the amount present in the film.

The PL dynamics of the $BA_{1.0}$-perovskite have been modeled in the previous section. Now, the dynamics of all other BA-perovskites with different spacer concentrations are fitted with a model considering both

FIGURE 5.8: a) PL divided by the initial excited-state density of samples with different BA-spacer concentrations fitted with **Equation 5.9** and below, b) PL efficiencies and c) $PL_{I.R.}$ shortly after PL_0 of the same samples using **Equation 5.9** and **5.11** with the same parameters as in a) Adapted from [133].

excitons and FCs as presented in **Equation 5.9**. The extracted parameters are summarized in **Table 5.1**. The fraction of excitonic emission gradually decreases from 77% to 52%, and then 42% as the spacer concentration changes from $BA_{0.8}$ to $BA_{0.6}$ and $BA_{0.4}$, respectively. Another trend observed in the BA series is that the effective rate constants of the bimolecular recombination, i.e. γ_{EEA} and k_2, both decrease as the BA concentration is decreased. This behavior can be explained as follows: At high concentrations of BA, there is a large fraction of small QWs in the film. This leads to only a small fraction of the initial excited states being funneled towards the small volume fraction of larger QWs from where the emission occurs. It follows that the excited-state densities within the energy minima QWs are significantly underestimated by taking the average excited-state density across the whole film and consequently the effective bimolecular rates are also significantly higher than the real microscopic rates inside the QWs. On the other hand, when the BA concentration is low, only a small volume fraction of the perovskite film is made up by small QWs and the emission comes from a greater volume fraction of larger QWs. The averaged N_0 over the whole film, therefore, does not underestimate the actual densities in the QWs to the same extent and the observed effective bimolecular rate constants may be much closer to the real rates. An additional effect is that the small emitting QWs for high concentrations of BA experience stronger confinement, which causes a small blueshift in the emission spectrum as illustrated in **Figure 5.9**. This does contribute to the higher bimolecular rate constants; however, the N_0 increase is assumed to be the dominant effect. Further work is necessary in the future to check this hypothesis.
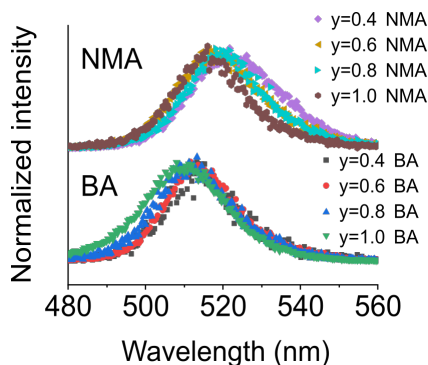
FIGURE 5.9: Normalized PL spectra of the different perovskites using BA and NMA. All spectra were taken at the highest excitation fluences used in this chapter. Adapted from [133].

5.5 Effect of NMA concentration on photophysics

In a similar analysis to the previous section, the change in the TRPL dynamics based on the amount of NMA in the perovskite is examined. The data is displayed in **Figure 5.10a**. On first inspection, the observations seem exactly analogous to the BA series shown in **Figure 5.8**. For increasing concentrations of NMA, the initial points of the TRPL data normalized by the initial excited-state density become less spread out. The initial points for high concentrations do not increase as much with fluences as for lower concentrations. This observation could suggest that similar to the BA-perovskites, an increasing amount of excitons contribute to the PL emission. This, however, necessitates an increased contribution of the longer-lived exciton emission. By comparing the TRPL-curves of the $NMA_{0.4}$- and the $NMA_{1.0}$-based perovskites, it is immediately clear that the longer-lived emission does not increase with the concentration of NMA. On the contrary, the long-lived signal of
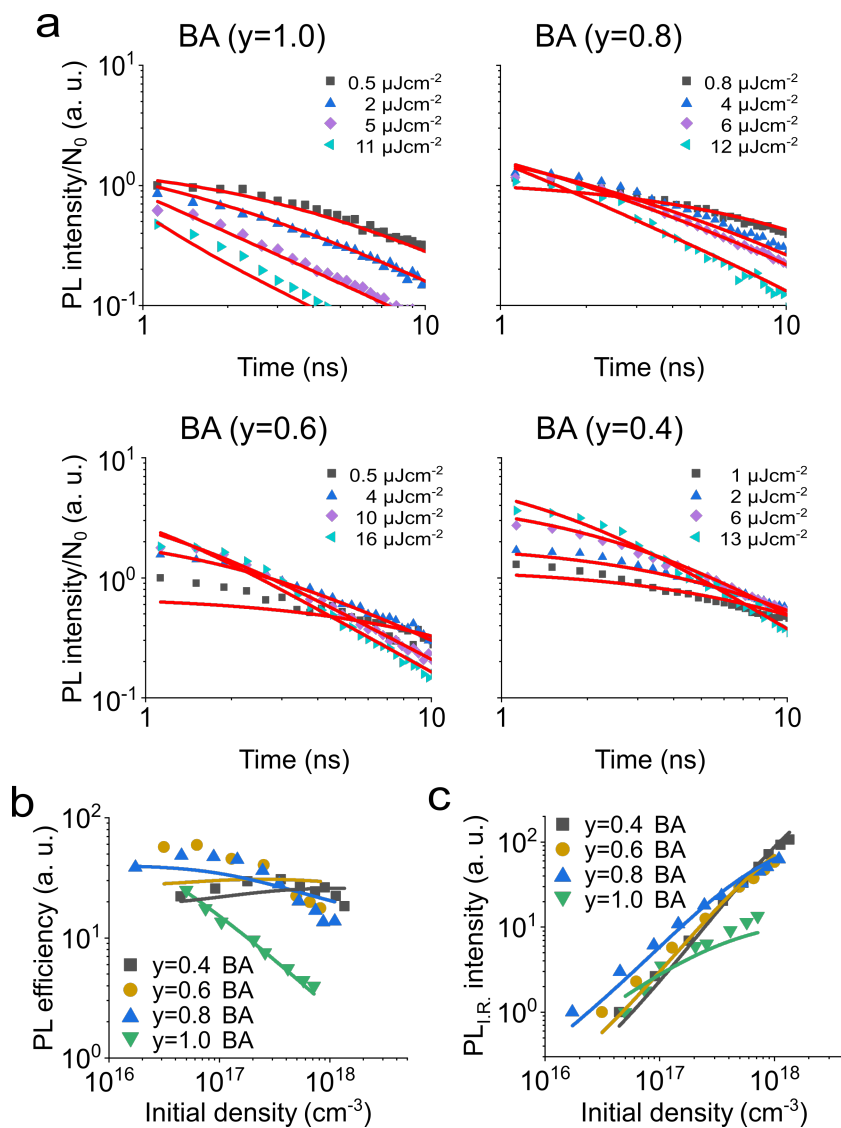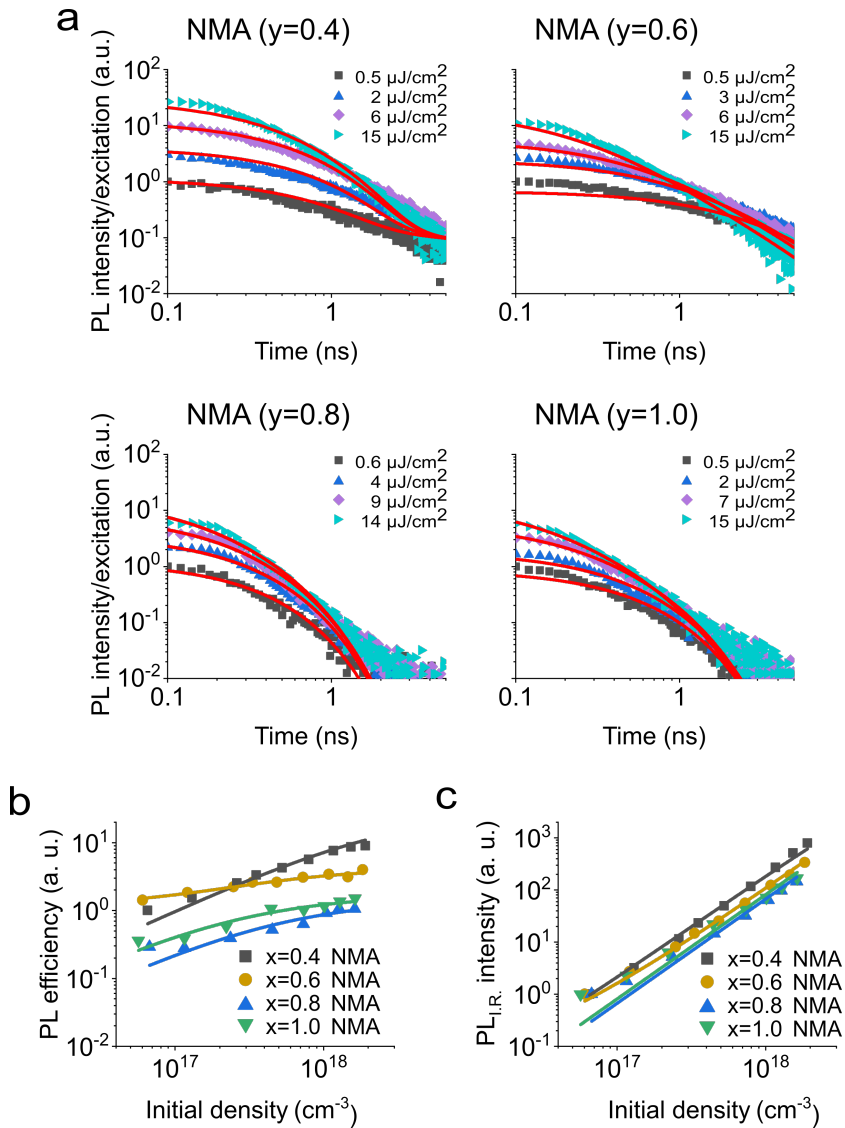
FIGURE 5.10: a) PL divided by the initial excited-state density of samples with different NMA-spacer concentrations and below b) PL efficiencies of the same samples and c) $PL_{I.R.}$ shortly after PL_0 of the same samples using **Equation 5.9** and **5.11** with the same parameters as in a). The initial densities for y=0.8 and y=1.0 are corrected as described in the text. Adapted from [133].

$NMA_{1.0}$ seems to decay even faster than for $NMA_{0.4}$ despite the initial points decreasing much less with increasing excitation fluence. This means that the NMA-series cannot be simply fitted using **Equation 5.9**. Only the two perovskites with $NMA_{0.4}$ and $NMA_{0.6}$ can be fit accurately by **Equation 5.9**, resulting in an exciton fraction of 7% and 22%, respectively. Trying to fit the $NMA_{0.8}$- and $NMA_{1.0}$-perovskites with an increasing PL contribution from excitonic emission to account for the decreasing slope of PL_0 leads to a significant overestimation of the longer-lived PL resulting in an inadequate fit of the data.

This poses the question of how it is possible for the initial emission, PL_0, to not depend on the square of the excitation fluence as is the case for FC emission despite excitonic emission not playing a significant role in the PL data. A possible answer to this observation relates to the increasingly fast effective rate constants for bimolecular processes described for the BA-series in the previous section. The larger volume fraction of smaller QWs in the perovskite film for higher concentrations of BA leads to higher excited-state densities in the sparser energy-minima QWs due to the strong funneling of excitons. It follows that an initial exciton will take more time to funnel into one of these sparser emitting energy-minima QWs. This increases the chance of EEA during the funneling process. In that case, the initial excited-state density in the emitting QWs would not scale linearly with the excitation fluence as EEA during the funneling would increasingly affect N_0. This effect could also affect the BA series and might contribute to the explanation of why the PL_0 slope for $BA_{1.0}$ is lower than one and those for the higher concentrations of NMA are much lower than two.

The feasibility of this explanation is demonstrated by comparing the excited-state population derived from the maximum PL, of the $NMA_{0.8}$- and $NMA_{1.0}$-perovskites with the initial excited-state density derived from the excitation fluence, which is revealed in **Figure 5.11**. To es-
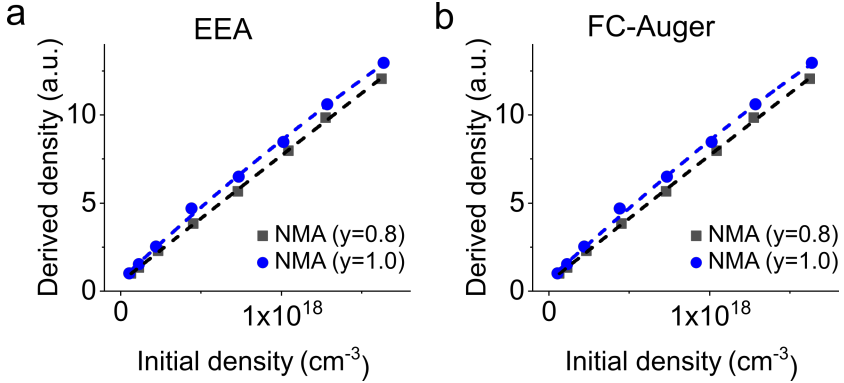
FIGURE 5.11: Initial densities derived from the maximum PL of the NMA$_{0.8}$- and NMA$_{1.0}$-perovskites, presuming mainly bimolecular radiative emission with a) parabolic and b) cubic fit to account for losses during the excited-state funneling process. Adapted from [133].

timate the initial excited-state density from the maximum PL, purely bimolecular radiative recombination is assumed. The density $N_{0,D}$ is then simply proportional to the square root of the PL, $N_{0,D} \propto \sqrt{PL_{max}}$. Taking EEA during the funneling process into account the initial density can be described by:

$$N_{0,D} = A \times N_0 - B \times N_0^2 + D, \qquad (5.12)$$

where A, B, and D are constants. The constant D accounts for exciton contributions at low fluences. Another potential loss mechanism is Auger recombination involving three free charge carriers. This can be described by:

$$N_{0,D} = A \times N_0 - C \times N_0^3 + D, \qquad (5.13)$$

where A, C, and D are constants. Fits based on these equations are shown in **Figure 5.11a** and **b**, respectively. Both equations lead to good
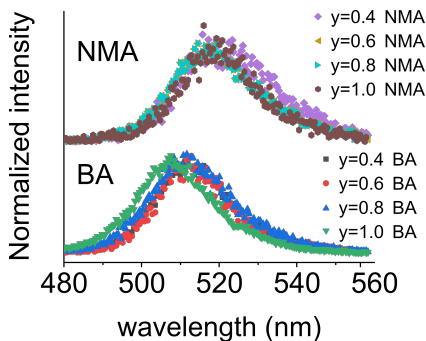
FIGURE 5.12: Initial densities derived from the maximum PL of the NMA$_{0.8}$- and NMA$_{1.0}$-perovskites presuming mainly bimolecular radiative emission with a) parabolic and b) cubic fit to account for losses during the excited-state funneling process. Adapted from [133].

fits of the observed losses. The high absorption coefficient in combination with the high exciton binding energy of low-dimensional QWs, as described in this chapter, means that the initial excited states are likely dominated by excitons. FCs only become relevant once the excited states have reached the energy-minima QWs. Therefore, the loss mechanism due to EEA during the funneling process is much more probable. The extracted constants from the fits in **Figure 5.11** are: $A_{0.8} = 7.3 \times 10^{-18}$; $A_{1.0} = 8.6 \times 10^{-18}$; $B_{0.8} = 7.4 \times 10^{-38}$; $B_{1.0} = 67 \times 10^{-38}$; $D_{0.8} = 0.52$; $D_{1.0} = 0.62$.

In some of these materials, ASE can be observed for much higher fluences than the ones used in this chapter. No ASE features like spectral narrowing are observable in the spectra taken at the highest fluences in this chapter, as can be seen in **Figure 5.12**. Transparency cannot explain these observations, therefore it is likely that the FC-based PL is dominant for all NMA-perovskites and the decrease of the PL$_0$-slope can be attributed to the increasingly strong EEA during the funneling process

towards the band gap-minima QWs where the emission occurs. For the fits of the $NMA_{0.8}$- and $NMA_{1.0}$-perovskites in **Figure 5.10** the initial densities N_0 are corrected using the fits from **Figure 5.11**. For the lowest fluence the derived and calculated initial densities are assumed to be the same. The extracted parameters show a small spread in the trapping rate $k_{1,c}$ which is on the order of the inverse of a couple of nanoseconds for the NMA-based perovskites as is displayed in **Table 5.1**. This fast trapping is consistent with the increasing PL efficiency even at the highest fluences used in this chapter as shown in **Figure 5.10b**. Similar to the BA-series there is a considerable increase in the bimolecular rate constant from $5 \times 10^{-10} \, cm^3 \, s^{-1}$ to $50 \times 10^{-10} \, cm^3 \, s^{-1}$ going from $NMA_{0.4}$ to $NMA_{1.0}$. Again, this is attributed to the decrease in the emitting volume fraction at higher concentrations. Assuming that the microscopic bimolecular rate constants stay the same, this result would indicate that the emitting volume fraction decreases by an order of magnitude as the concentration of NMA increases.

5.6 Discussion

The results of the analysis in the previous sections suggest that the PL characteristics in quasi-2D perovskites based on the BA-spacer are more likely to be dominated by excitonic emission, with FCs only playing a role for low concentrations of BA. FCs seem to dominate the emission for the quasi-2D perovskites made using NMA at all used concentrations. This would suggest that the emitting QWs of the NMA films should be slightly larger and therefore exhibit a lower band gap (due to less confinement). As can be seen in **Figure 5.9** and **Figure 5.12**, the emission from NMA-based perovskites is lower in energy at all used concentrations than the emission from the BA-based perovskites. This is consistent with the emission in NMA-perovskites occurring from larger

TABLE 5.1: Extracted parameters of the fits demonstrated in **Figure 5.8, 5.9 and 5.11**. ***constraint to allow for sensible fits**

Quasi-2D Perovskite	$f\,(\%)$	k_x $\times 10^7$ (s^{-1})	γ_{EEA} $\times 10^{-10}$ $(\mathrm{cm}^3\,\mathrm{s}^{-1})$	$k_{1,c}$ $\times 10^7$ (s^{-1})	$k_{2,c}$ $\times 10^{-10}$ $(\mathrm{cm}^3\,\mathrm{s}^{-1})$
$\mathrm{NMA}_{0.4}$	7 ± 3	6 ± 3	0^*	74 ± 2	4.7 ± 0.2
$\mathrm{NMA}_{0.6}$	22 ± 1	27 ± 2	2.4 ± 0.3	36 ± 2	13.0 ± 0.4
$\mathrm{NMA}_{0.8}$	0^*	-	-	141 ± 4	31 ± 2
$\mathrm{NMA}_{1.0}$	0^*	-	-	86 ± 2	50 ± 1
$\mathrm{BA}_{0.4}$	42 ± 1	2.6 ± 0.2	0.75 ± 0.05	4.9 ± 0.7	3.7 ± 0.2
$\mathrm{BA}_{0.6}$	52 ± 2	3.9 ± 0.2	1.7 ± 0.1	7 ± 1	8.4 ± 0.5
$\mathrm{BA}_{0.8}$	77 ± 2	4.7 ± 0.2	4.8 ± 0.2	6 ± 4	19 ± 2
$\mathrm{BA}_{1.0}$	100^*	2.7 ± 0.1	60 ± 1	-	-

QWs. The redshift observed for the BA-series with decreasing concentration is also in line with the increasing PL contribution from larger band gap-minima QWs and the associated emission of FC recombination.

As mentioned in the respective sections, the effective rate constants of the bimolecular recombination processes in these quasi-2D perovskites increase with the increase of the spacer molecule concentration. The

microscopic rates inside the emitting QWs increase due to stronger confinement as the average QW size may decrease for higher spacer concentrations. However, some fraction of the change in the rates is likely due to the smaller emitting volume fraction in the film. For higher concentrations, there are fewer band gap-minima QWs, meaning that excited states funneled into these sparse QWs lead to very high densities. These are considerably higher than the estimation of N_0 resulting from averaging the excited-state densities over the whole film. This estimation becomes increasingly erroneous as the volume fraction of emitting QWs decreases. For lower concentrations of the spacer molecules, the excited state densities are also underestimated; however, the estimation will be much closer in this case. The comparison of the effective rates is of merit and can be used to gain insight into the material. A better understanding of the exact mechanisms inside the emitting volume fractions after photoexcitation would be of great interest for the development of a more detailed model describing the photophysics. From the current experimental work, it is not obvious how this information could be gained. Further material and method development in this area are necessary in the future.

As for the device understanding, the following salient points have been established: The excited-state species in a quasi-2D perovskite needs to be considered carefully. The results of this chapter suggest that assuming excitons will always dominate in these materials is incorrect. Depending on the spacer molecule and its concentration, the excited-state population can vary between excitons, free charge carriers, or even a mixture of the two.

Quasi-2D perovskites utilizing the BA spacer have been shown to exhibit high external quantum efficiencies of 10.1% in PeLEDs [136]. Even small concentrations of BA lead to smoother surfaces and increase

the radiative resulting in higher EQEs [137]. The increase of the molar ration of BA in a MAPbBr$_3$ perovskite has been demonstrated to enormously improve the quantum yield from 0.2% at y=0 up to 40.1% at y=0.4 with faster radiative than nonradiative recombination even at low current densities [138]. Based on the results in this chapter, the excited state population at these concentrations is likely made up of both excitons and FCs. The higher contribution of excitons could increase the efficiency by reducing the trapping [139]. An increase in the BA concentration has, however, also been shown to increase shunt paths [137]. Smoothing the energy transfer between the differently sized QWs and thereby improving the funneling process has been demonstrated to greatly increase the EQE up to 20.5% for 0.3<y<0.4 [26]. Increasing the fraction of excitons in the excited-state population while avoiding shunt losses and losses during the funneling process could lead to highly efficient PeLEDs for low current densities.

In photovoltaic applications the separation of charges is necessary, therefore the NMA-based perovskites would be favorable. In recent work quasi-2D perovskites utilizing NMA as a spacer molecule have been used as an absorber material, albeit at very low concentrations leading to large QWs and using an organic cation and iodide. The introduction of NMA in the film leads to an increase in the thermal stability of the perovskite [140]. For solar cells with this material the open-circuit voltage also increases which leads to a higher power conversion efficiency [141]. It has also been suggested that the conjugated structure of NMA improves the charge transfer between the perovskite layers [142]. NMA is suggested to decrease the trapping in perovskites [140], however, based on the results in this chapter the increase of the concentration beyond y=0.6 is not suggested. An increase in the NMA concentration while avoiding the fast trapping might lead to highly efficient and stable solar cells.

5.7 Summary

In this chapter has been demonstrated that the time-resolved PL charac-
teristics of quasi-2D materials are significantly different depending on
the used 2D-spacer molecule (BA or NMA) and the concentration of the
given spacer. It is not possible to describe the TRPL dynamics using a
model considering only excitons or only free charge carriers. A simple
model is proposed that consistently explains all the data of this chapter
and involves two independent pools of excited states, an FC pool, and an
exciton pool. This model is sufficient to describe the TRPL-dynamics,
the initial PL rate (PL_0) and the PLQY. At high concentrations of NMA
in the film, this model has to be slightly augmented to allow for high-
order population losses before the emission occurs.

For perovskites based on BA the monomolecular exciton recombina-
tion constants extracted range from $\mathbf{2.6 \times 10^7} \mathrm{s}^{-1}$ to $\mathbf{4.7 \times 10^7} \mathrm{cm}^3 \mathrm{s}^{-1}$.
For changes in the molar ratio between y=0.4 and y=1.0, the rates are
essentially unaffected. The effective rate constants for EEA, however,
continuously increase from $\mathbf{0.75 \times 10^{-10}} \mathrm{cm}^3 \mathrm{s}^{-1}$ to $\mathbf{60 \times 10^{-10}} \mathrm{cm}^3 \mathrm{s}^{-1}$
with the BA concentration. The effective rate is calculated by assum-
ing that the initial excited state density is uniform across the entire per-
ovskite film. A large part of the change in the effective rates is ascribed
to a decrease in the validity of this assumption as the BA concentra-
tion increases. While the changes in the diffusion rate or exciton radius
might also contribute to that, this effect is likely to be less dominant.
The amount of emitting QWs making up only a small volume fraction
of the film, unfortunately, cannot easily be ascertained, therefore the
true rates of EEA inside the QWs cannot be determined. This open
question regarding the real rates requires further experimental consid-
eration and novel approaches to provide the necessary data for more
detailed answers. For low BA contents, FCs significantly contribute to
the PL emission. The FC population has been observed to be much

shorter-lived than the exciton population which is consistent with the observations for the NMA-based perovskites. The effective bimolecular rates for the FC recombination vary from 3.7×10^{-10}cm^3 s^{-1} to 19×10^{-10}which is higher than the typically observed values for 3D-perovskites [143]. These rates do also increase with the spacer concentration which again is consistent with the explanation given for the EEA rates.

For the NMA-based perovskites, the effective bimolecular rates range between 4.7×10^{-10}cm^3 s^{-1} and 50×10^{-10}cm^3 s^{-1}, increasing with the NMA concentration. This is contributed to the same mechanism as with the BA-perovskites. The fast trapping on the order of 10^{-9}s^{-1} leads to efficiencies increasing even at high excitation fluences as radiative recombination becomes more dominant. The absence of long-lived PL at high NMA concentrations in combination with a power-law slope below two for the initial PL (PL$_0$) makes it very likely that a higher-order loss mechanism during the funneling process occurs rather than an increase in the excitonic PL. The TRPL can be reasonably fitted by only considering FCs, meaning that excitonic PL only plays a minor role for NMA-based quasi-2D perovskites.

To summarize, it has been shown that the TRPL of quasi-2D perovskites is not trivial and can be due to excitons, free charge carriers, or a mixture of the two, depending on the used spacer molecule and its concentration. It has been demonstrated that a simple model considering two independent pools of excitons and free carriers can explain all made observations. Further insight into the photophysics of the emitting QWs and the funneling process are interesting topics for research and potential device improvements in the future.

6

Excited State Dynamics Revealed by Time-Integrated Photoluminescence after Double-Pulse Excitation

The decay kinetics of excited states like free charge carriers or excitons can be described by the rate constants of a perovskite material. These constants are typically determined by recording the time-dependent photoluminescence on the nanosecond scale with highly specialized detectors. In this chapter a method is applied that allows for the extraction of the rate constants with the use of two excitation pulses with a variable delay between them and an inexpensive detector recording the quasi-steady state photoluminescence. The rate constants for exciton-exciton annihilation, monomolecular exciton decay, bimolecular free charge carrier recombination, and monomolecular trapping of free charge carriers can be extracted based on how the time-integrated photoluminescence varies as a function of the delay time between the two excitation pulses. The method is demonstrated on a variety of perovskites starting with quasi-2D perovskites as they are known to exhibit excited-state populations that can be exciton dominated, free charge carrier dominated, or a mixture of the two. The unique curves resulting from the

method allowed for accurately extracted parameters in all cases. Additionally, the method is demonstrated with a 3D perovskite showing the potential for its use in a wide field of applications. The detector used in this method does not need high temporal resolution, which opens the path to the spatial mapping of excited-state dynamics using standard cameras which would be attractive for quality control of photovoltaic layers.

This chapter is based on my first-author manuscript that has been accepted for publication in *Advanced Materials Technologies* but has as of the submission of this work not yet been published. The manuscript is titled *"Charge carrier and exciton dynamics in perovskites revealed by time-integrated photoluminescence after double-pulse excitation"*.

6.1 Motivation

This chapter expands on the ideas and results from **Chapter 5**. In quasi-2D perovskites both excitons, free charge carriers or a mixture of the two can make up the excited-state population. The excited-state species has been found to depend on the spacer molecule and its concentration in the perovskite film. With a simple two-pool model of independent excitons and free charge carriers, the TRPL characteristics can be modeled. The nature of the excited-state population and the rate constants of these states are fundamental in understanding the materials used for device fabrication. This is of special relevance for quasi-2D perovskites as both excitons and free carriers can be supported; however, the quality of a 3D-perovskite film can also be assessed from the extracted free carrier rate constants. A widely used method to extract the rate constants is by observing the time-resolved photoluminescence (TRPL). Unfortunately, this method relies on expensive and sensitive hardware, e.g. a streak camera or a time-correlated single photon counting setup. Furthermore,

measurements usually take hours, meaning they are not suitable for in-line characterization in a device fabrication line.

In this chapter will be demonstrated that the excited-state dynamics of perovskites can be determined via the measurement of the time-integrated photoluminescence (TIPL) after the impulsive excitation from two short optical pulses whose intensities are controlled, as is the delay time between them. Similar approaches have been used in past publications for the analysis of photogenerated carriers [144], as well as in the study of graphene layers on femto- and picosecond timescales [145,146] and in the investigation of emission for nanowire lasing [147]. A simple USB spectrometer is used to detect the TIPL. The excitation pulses can be generated from a couple of Q-switched lasers with a delay generator set between them. The setup is illustrated in **Figure 6.1**.
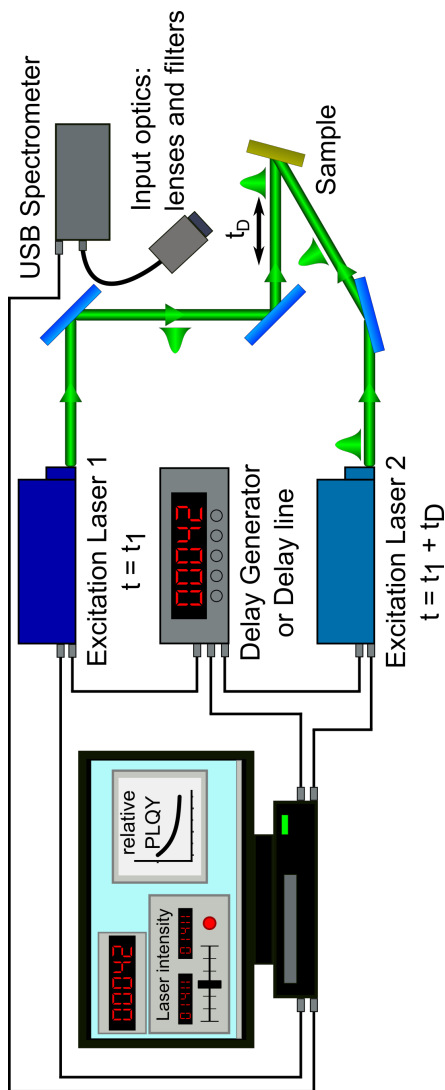
FIGURE 6.1: Experimental setup for determining the decay constants of the excited-state populations through double-pulse excitation (e.g., at 530 nm). A computer sets a digital delay generator to specify the delay between two Q-switched laser pulses (with a repetition rate of, e.g., 1 kHz). The time-integrated photoluminescence (TIPL) is measured of the two-pulse train with the given delay over a collection window that is long compared to the repetition rate of the lasers (i.e. the quasi-CW PL is recorded for a given pulse delay). The delay is then altered, and the PL measured for a train with a different delay between the pulses. This is repeated for the desired set of time delays. To extract the rate constants, the PL measured per excitation photon is normalized to the PL per excitation photon when only a single pulse is present and plotted as a function of the delay time.

The TIPL varies depending on the delay between the two pulse trains. This change in the total emission depends on the dominant emissive excited-state species. For materials dominated by excitons, the TIPL decreases as the delay time is decreased, due to an increased amount of exciton-exciton annihilation (EEA) and the resulting lower photoluminescence quantum yield (PLQY). Measuring the PLQY is not trivial and requires an integrating sphere. Instead, the change in the PL emission and therefore the change in the PLQY is measured. If the material supports free charge carriers rather than excitons, the TIPL increases for a smaller delay between the pulse trains. This is due to the increase in the radiative bimolecular recombination for the higher excited-state densities which become more dominant relative to the monomolecular trapping and therefore lead to more PL emission. It will be shown in this chapter that the rate constants for exciton-exciton annihilation, monomolecular exciton decay, bimolecular free charge carrier recombination, and monomolecular trapping of free charge carriers can be extracted from an analysis of the change in the PLQY after excitation with the double-pulse sequence relative to excitation with a single pulse as a function of the time delay between the pulses. Finally, the huge potential advantages that this method allows, i.e. fast extraction of the rate constants over a whole surface by "imaging" with robust detectors in a fabrication line, are discussed.

The following sections describe how the rate constants of different perovskite materials can be extracted utilizing a sequence of intensity-controlled double pulse excitations with different delay times in between them and measuring the TIPL. First, the model presented in the previous chapter is expanded to simulate the TIPL for excitons and free charge carriers respectively depending on the delay time between the pulses. Then the distinct features in the relative PLQY are examined

and a method to extract the relevant rate constants is demonstrated. Afterward, the method is applied to real data as a test case on quasi-2D perovskite films where the excited state population can be varied by adjusting the spacer molecule and its concentration. First, only a pure exciton and a pure free carrier population are compared, then a mixture of the two is analyzed. Finally, the same method is also applied to a 3D-perovskite to show the validity for potential photovoltaic applications. In all cases, the model allows for the extraction of the relevant rate constants.

6.2 Simulation

6.2.1 Excitonic Photoluminescence

Similar as in the previous chapter the simulation starts with the equation introduced in **Section 2.1.1**:

$$\frac{dn_x}{dt} = -k_x n_x - \gamma_{EEA}(t) n_x^2, \tag{6.1}$$

n_x is the exciton density, k_x is the total monomolecular rate constant including radiative and non-radiative contributions, $k_x = k_{x,rad} + k_{x,nrad}$ and γ_{EEA} is the rate constant for the nonradiative exciton-exciton annihilation. The diffusion of excitons in 2D, quasi-2D, and 3D perovskites is not constraint meaning the EEA rate can be considered time-independent. It is clear from this equation that EEA plays a minor role for low densities of excitons, resulting in most excitons recombining via the monomolecular rate. For higher densities EEA becomes the dominant recombination pathway due to its nonlinear dependence. Since EEA is a nonradiative pathway, the efficiency of emission decreases as the excitation fluence increases. This is further described in the previous chapter (**Section 5.2**) and illustrated in **Figure 5.4**. A double-pulse

experiment implies that the PL emission for short temporal delays between the pulse trains where the exciton densities reach higher values will be lower than for the emission at longer delays. For the quantitative analysis of the PL emission depending on the temporal delay, the relative PLQY is introduced. This value describes the TIPL divided by twice the TIPL for a single pulse train if both pulse trains contain the same excitation fluence. For pulse trains with different excitation fluences, another approach is also possible by dividing the TIPL with the PL emission at a sufficiently large delay where the excited states have decayed completely before the next excitation pulse arrives.

This principle is illustrated in **Figure 6.2a** where the PL emission intensity over time for both a single and a double-pulse excitation at a short temporal delay is shown. The TIPL observed in the experiments is directly proportional to the area under these curves. The relative PLQY is determined by simply dividing the measured TIPL under double-pulse excitation by twice the TIPL that is recorded when one excitation laser is blocked. Of course, for long delay times, the relative PLQY values have to move towards unity. For short temporal delays, however, it drops below unity as the excited state density of the first pulse has not decayed yet when the delayed second pulse arrives. This leads to a higher maximum exciton density relative to a single pulse excitation and increases the amount of nonradiative decay due to EEA. The overall emission thereby is lower than two single pulse excitations. In **Figure 6.2b** it is demonstrated how the curve of the relative PLQY depends on the initial exciton density generated by the excitation pulses N_0. For this simulation, the rate constants are based on the experimental results below and are: $k_x = 30 \times 10^7 \, \mathrm{s}^{-1}$; $\gamma_{EEA} = 1 \times 10^{-10} \, \mathrm{cm}^3 \, \mathrm{s}^{-1}$.

The equations for the derivation of the relative PLQY quickly become bloated. They are presented in this work for the interested reader who
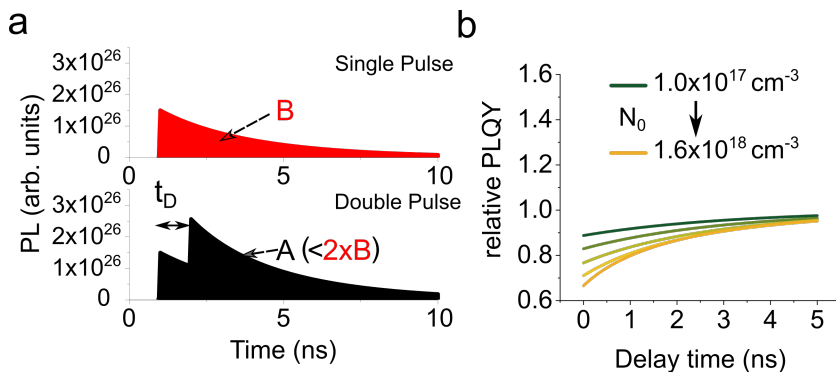
FIGURE 6.2: a) Simulation of the time-dependent exciton PL of a single and a double-pulse excitation wherein both pulses generate the same initial density ($N_0 = 5 \times 10^{17}$ cm^{-3}). For a "short" delay t_D (1 ns, bottom) the residual exciton population from the first pulse pushes the total exciton population after the second pulse to higher values and thus decreases the PLQY relative to the PLQY of a single pulse (top) due to increased exciton-exciton annihilation. b) the relative PLQY can be defined as the number of photons observed per total excitation photons in the double-pulse normalized to the number of PL photons per excitation photon for a single pulse only. At long time delays, the relative PLQY approaches the limit of unity. For additional information, the curves are shown for changing pulse fluence (the exciton density created by a single pulse is carried from 10^{17} to 1.6×10^{18} cm^{-3}).

might use or adapt them for their modeling and can be skipped for readers more interested in the results. For the derivation of the relative PLQY the analytical solution for the time-dependent PL can be found from **Equation 6.1**:

$$
\begin{aligned}
PL_{x,1}(t) &\propto k_{x,rad)}n_x(t) \\
&= k_x \left(\frac{k_{x,rad}}{k_{x,rad} + k_{x,nrad}} \right) n_x(t) \\
&= k_x \phi \frac{k_x}{\gamma_{EEA}(\exp(k_x t) - 1) + \frac{k_x}{N_0}\exp(k_x t)},
\end{aligned}
\tag{6.2}
$$

where N_0 is the initial exciton density and ϕ is the PLQY without any EEA. As in **Chapter 5**, the initial density is averaged over the whole film volume. The quantum yield of the PL emission can then simply be derived from **Equation 6.2**:

$$
\begin{aligned}
PLQY_{x,1} &= \frac{\int_0^\infty k_{x,rad}n_x(t)dt}{N_0} \\
&= \phi \frac{k_x}{\gamma_{EEA}N_0} \ln\left(\frac{k_x + \gamma_{EEA}N_0}{k_x} \right).
\end{aligned}
\tag{6.3}
$$

Considering two excitation pulses with a temporal delay of t_D between them, the excited states of the first pulse will have decayed partially when the second pulse gets absorbed. The initial excited states of the second pulse will therefore be slightly higher than for the first pulse. The initial density N_1 of the second pulse can be calculated from the

time-dependent excited-state density given in **Equation 6.2**:

$$
\begin{aligned}
N_{1,x} &= N_{0,B} + n_x(t_D) \\
&= N_{0,B} + \frac{k_x}{\gamma_{EEA}(\exp(k_x t_D) - 1) + \frac{k_x}{N_{0,A}}\exp(k_x t_D)},
\end{aligned}
\tag{6.4}
$$

where $N_{0,A}$ and $N_{0,B}$ are the initial excited-states generated by the first and second pulse, respectively. To observe any change in the PL emission dependent on t_D, the excited states must not have decayed completely before the second pulse arrives; otherwise, **Equation 6.3** simplifies to $N_{1,x} = N_{0,B}$. For a delay time of $t_D = 0$ the equation simplifies to $N_{1,x} = N_{0,B} + N_{0,A}$. The time-dependent PL from a double-pulse excitation can directly be calculated from the initial excited states:

$$
\begin{aligned}
PL_{x,2} &\propto k_{x,rad} n'_x(t) \\
&= \begin{cases} k_x\phi \, \frac{k_x}{\gamma_{EEA}(\exp(k_x t)-1)+\frac{k_x}{N_{0,A}}\exp(k_x t)}; & t < t_D \\ k_x\phi \, \frac{k_x}{\gamma_{EEA}(\exp(k_x(t-t_D))-1)+\frac{k_x}{N_{1,x}}\exp(k_x(t-t_D))}; & t \geq t_D \end{cases}
\end{aligned}
\tag{6.5}
$$

In these cases, the excitation pulses are considered to be very short compared to the excited-state lifetimes so the excitation can be assumed to be instantaneous. Similar to the case of the single pulse excitation, the PLQY for the double-pulse excitation can be derived by integrating

Equation 6.5:

$$
\begin{aligned}
PLQY_{x,2} &= \frac{\int_0^\infty k_{x,rad} n_x'(t)\,dt}{N_{0,A} + N_{0,B}} \\
&= \frac{k_x \phi}{(N_{0,A} + N_{0,B})\gamma_{EEA}} \left(\ln(k_x \exp(k_x t_D) - \gamma_{EEA} N_{0,A} \right. \quad (6.6) \\
&\qquad\qquad + \gamma_{EEA} N_{0,A} \exp(k_x t_D)) - k_x t_D - \ln(k_x) \\
&\qquad\qquad\qquad\qquad \left. + \ln\left(\frac{k_x + \gamma_{EEA} N_{1,x}}{k_x} \right) \right)
\end{aligned}
$$

For a simple sanity check the PLQY for long delays is determined. For $t_D \to \infty$ this equation becomes:

$$
\begin{aligned}
PLQY_{x,2} &\to \frac{PLQY_{x,1}(N_{0,A}) \times N_{0,A} + PLQY_{x,1}(N_{0,B}) \times N_{0,B}}{N_{0,A} + N_{0,B}} \\
&= \frac{\phi \frac{k_x}{\gamma_{EEA}} \left(\ln\left(\frac{k_x + \gamma_{EEA} N_{0,A}}{k_x} \right) + \ln\left(\frac{k_x + \gamma_{EEA} N_{0,A}}{k_x} \right) \right)}{N_{0,A} + N_{0,B}}.
\end{aligned} \quad (6.7)
$$

When $N_{0,A} = N_{0,B}$, this equation further simplifies to $PLQY_{x,2} = PLQY_{x,1}$. For no delay, $t_D = 0$, the PLQY has a minimum depending on the strength of the EEA relative to the monomolecular recombination rate. If the EEA is relatively low, this minimum will be close to the PLQY at long delay times. The relative PLQY introduced above is calculated by dividing the PL from a double-pulse excitation by the PL at a long time delay. Alternatively, if $N_{0,A} = N_{0,B}$, the PL of the double-pulse excitation can simply be divided by twice the PL of a single-pulse excitation. For the interested reader the more general solution is derived:

$$rPLQY_x(t_D) = \frac{PLQY_{x,2}(t_D)}{PLQY_{x,2}(t_D \to \infty)} \tag{6.8}$$

$$= \frac{\frac{k_x \phi}{(N_{0,A}+N_{0,B})\gamma_{EEA}} \left(\begin{array}{c} \ln(k_x \exp(k_x t_D) - \gamma_{EEA}N_{0,A} + \gamma_{EEA}N_{0,A} \exp(k_x t_D)) \\ -k_x t_D - \ln(k_x) + \ln\left(\frac{k_x+\gamma_{EEA}N_{1,x}}{k_x}\right) \end{array} \right)}{\left(\frac{\phi \frac{k_x}{\gamma_{EEA}} \left(\ln\left(\frac{k_x+\gamma_{EEA}N_{0,A}}{k_x}\right) + \ln\left(\frac{k_x+\gamma_{EEA}N_{0,A}}{k_x}\right) \right)}{N_{0,A}+N_{0,B}} \right)}$$

$$= \frac{\left(\begin{array}{c} \ln(k_x \exp(k_x t_D) - \gamma_{EEA}N_{0,A} + \gamma_{EEA}N_{0,A} \exp(k_x t_D)) \\ -k_x t_D - \ln(k_x) + \ln\left(\frac{k_x+\gamma_{EEA}N_{1,x}}{k_x}\right) \end{array} \right)}{\ln\left(\frac{k_x+\gamma_{EEA}N_{0,A}}{k_x}\right) + \ln\left(\frac{k_x+\gamma_{EEA}N_{0,B}}{k_x}\right)}$$

Since the radiative process is linear and negative values are not possible, the relative PLQY must be between 0 and 1 for excitonic emission.

To summarize in simple terms, the area under the curves illustrated in **Figure 6.2a** represents the TIPL. The shorter the delay times the higher the number of residual excited states from the first pulse exists as the second pulse is absorbed, resulting in a higher excited-state density, $N_{1,x}$. This leads to an increase in the nonradiative EEA. The grey curve represents the TIPL of a double-pulse excitation and the red curve represents a single-pulse reference whereby one laser is blocked. The relative PLQY at a given delay time is calculated by dividing the grey area by twice the red area. The relative PLQY is shown in **Figure 6.2b**. The delay time is the relative delay time between the two pulse trains. The two pulses are concurrent at a delay time of 0, with negative delay times meaning that the second pulse precedes what was previously considered, the first pulse. The function for the relative PLQY is symmetric on the y-axis, i.e. negative and positive delays lead to the same value of the relative PLQY. Furthermore, the relative PLQY curves are shown for

different excitation fluences of both pulses ranging between 10^{17} and $1.6 \times 10^{18}\,\mathrm{cm}^{-3}$. At short time delays, the relative PLQY has a minimum due to EEA being most dominant in that region. For increasing delay times between the pulse trains, the relative PLQY moves towards unity. A single relative PLQY curve—given that it is not constant—as shown in **Figure 6.2b** contains enough information to extract both rate constants. This would not be possible by simply measuring the steady-state PLQY on its own using an integrating sphere; since the temporal information would be lost. A gedankenexperiment to demonstrate this: if both rate constants were doubled, the PLQY would not change. In the relative PLQY, however, the curves would move towards unity at shorter delays. The uniqueness of the relative PLQY curves and the capability of extracting the rate constants is demonstrated by fitting noisy data at different initialization points in **Figure 6.3**

It is well possible to fit a single relative PLQY curve resulting from an experiment to accurately determine the rate constants. As the curve must not be constant, the excitation fluence must be high enough for EEA to occur. The right excitation fluence is therefore chosen according to prior knowledge about the investigated material or via trial and error.

6.2.2 Free Charge Carrier Photoluminescence

If the excited-state population is dominated by free charge carriers rather than excitons, the photoluminescence from a double-pulse excitation is vastly different. The monomolecular rate, in this case, is associated with the trapping of charge carriers which is a nonradiative process while the radiative process is bimolecular, i.e. nonlinear. This is the exact opposite as for excitons where the nonlinear process is nonradiative and the monomolecular is radiative. As described in **Section 2.1.2**, the rate equation for the free charge carrier density after pulsed excitation can

a

b
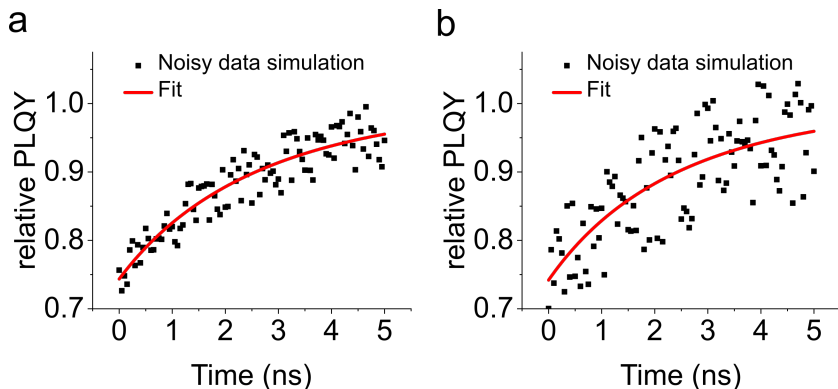
FIGURE 6.3: Illustration of the unique extracted parameters by simulating noisy data by multiplying simulated points with a random number between a) 0.95 and 1.05 and b) 0.9 and 1.1. The parameters used are: $k_x = 3 \times 10^8 \, \text{s}^{-1}$; $\gamma_{EEA} = 1 \times 10^{-10} \, \text{cm}^3 \, \text{s}^{-1}$ and $N_0 = 5 \times 10^{17} \, \text{cm}^{-3}$. The fitting results did not change with different initial fitting points and are a) $k_x = (3.1 \pm 0.1) \times 10^8 \, \text{s}^{-1}$; $\gamma_{EEA} = (1.1 \pm 0.1) \times 10^{-10} \, \text{cm}^3 \, \text{s}^{-1}$ and b) $k_x = (3.3 \pm 0.3) \times 10^8 \, \text{s}^{-1}$; $\gamma_{EEA} = (1.2 \pm 0.3) \times 10^{-10} \, \text{cm}^3 \, \text{s}^{-1}$

be written as:

$$\frac{dn_c}{dt} = -k_{1,c}n_c - k_{2,c}n_c^2, \tag{6.9}$$

where n_c is the carrier density, $k_{1,c}$ is the free charge carrier trapping rate constant associated with non-radiative decay, and $k_{2,c}$ is the bimolecular radiative recombination rate constant. At low fluences most generated charge carriers will recombine nonradiatively. For increasing excitation fluences, the bimolecular recombination becomes more dominant and the emission efficiency increases. Once all charge carriers recombine radiatively, the PLQY can increase no further. At some point, nonradiative third-order Auger processes start to become significant and the PLQY starts to decrease again. In this chapter, the excitation fluence was

kept low enough that no Auger recombination could be observed. The dependence of the PLQY on the excitation fluence is further described in **Section 5.2** and illustrated in **Figure 5.5**. For the double-pulse excitation, this implies that at short temporal delays where the residual carrier density from the first pulse gets pushed to a higher value by the second pulse the PLQY will be higher than for longer delays, so the exact opposite as for excitons. The relative PLQY can again be calculated by dividing the TIPL of a double-pulse excitation at a certain delay time with either twice the TIPL of a single pulse excitation when both pulses have the same fluence or the TIPL at a very long delay. For long delay times, again, the relative PLQY approaches unity as this is the same as two individual single pulse excitations. For short delay times, however, the relative PLQY will exceed unity and increases with a decrease in the delay as the emission becomes more efficient due to the increased carrier density. Due to the bimolecular radiative behavior, the relative PLQY must not exceed two. This principle is displayed in **Figure 6.4**. The rate constants for this simulation are based on my previous work [133]: $k_{1,c} = 70 \times 10^7 \, \text{s}^{-1}$ and $k_{2,c} = 5 \times 10^{-10} \, \text{cm}^3 \, \text{s}^{-1}$.

In a) the simulated time-dependent PL for both single pulse and double-pulse excitation is illustrated when free charge carriers are the dominated excited-state species. Again, the derivations are meant for the interested reader only and can otherwise be skipped. For the derivation of the relative PLQY in the case of dominant emission from free charge carriers the analytical solution for the time-dependent PL can be found from **Equation 6.9**:

$$PL_{c,1}(t) = k_{2,c)}n_c(t)^2$$
$$= k_{2,c} \left(\frac{k_{1,c}}{k_{2,c}(\exp(k_{1,c}t) - 1) + \frac{k_{1,c}}{N_0} \exp(k_{1,c}t)} \right)^2, \quad (6.10)$$
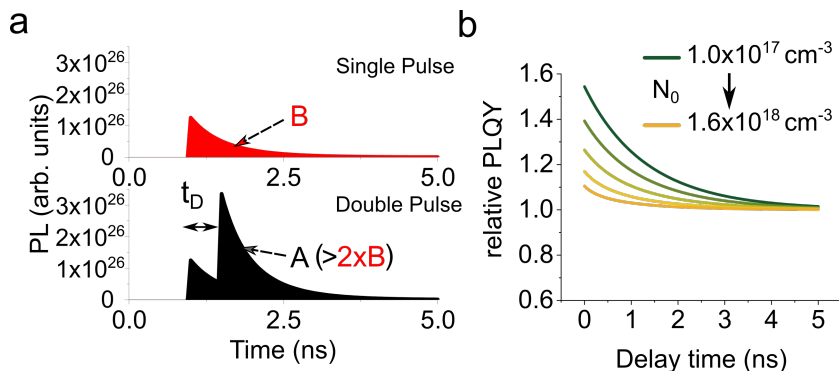
FIGURE 6.4: a) Simulation of the time-dependent free carrier PL of a single and a double-pulse excitation wherein both pulses generate the same initial density ($N_0 = 5 \times 10^{17} \, \text{cm}^{-3}$). For a "short" delay t_D (0.5 ns, bottom) the residual free carrier population from the first pulse pushes the total free carrier population after the second pulse to higher values and thus increases the PLQY relative to the PLQY of a single pulse (top) due to increased bimolecular radiative recombination. b) the relative PLQY can be defined as the number of photons observed per total excitation photons in the double-pulse normalized to the number of PL photons per excitation photon for a single pulse only. At long time delays, the relative PLQY approaches the limit of unity. For additional information, the curves are shown for changing pulse fluence (the free carrier density created by a single pulse is carried from 10^{17} to $1.6 \times 10^{18} \, \text{cm}^{-3}$

where N_0 is the initial free carrier density. As in the case of excitons the initial density is averaged over the whole film volume. The quantum yield of the PL emission can then be derived from this **Equation 6.10**:

$$
\begin{aligned}
PLQY_{c,1} &= \frac{\int_0^\infty k_{2,c} n_c^2(t) dt}{N_0} \\
&= \frac{\left(k_{2,c} N_0 + k_{1,c} \ln\left(\frac{k_{1,c}}{k_{1,c}+k_{2,c}N_0}\right)\right)}{k_{2,c} N_0}.
\end{aligned}
\tag{6.11}
$$

Equivalently to the case for excitons from the time-dependent PL, the density of charge carriers after the delay time t_D can be calculated from **Equation 6.11**:

$$
\begin{aligned}
N_{1,c} &= N_{0,B} + n_c(t_D) \\
&= N_{0,B} + \frac{k_c}{k_{2,c}(\exp(k_c t_D) - 1) + \frac{k_c}{N_{0,A}} \exp(k_c t_D)},
\end{aligned}
\tag{6.12}
$$

where $N_{0,A}$ and $N_{0,B}$ are the initial excited-states generated by the first and second pulse, respectively. The time-dependent PL for a double-pulse excitation can be described equivalently to the excitonic PL but with the quadratic dependence on the excited state dependence:

$$
\begin{aligned}
PL_{c,2} &= k_{2,c} n_c'^{\,2}(t) \\
&= \begin{cases}
k_{2,c} \left(\dfrac{k_{1,c}}{k_{2,c}(\exp(k_{1,c}t)-1)+\frac{k_{1,c}}{N_{0,A}}\exp(k_{1,c}t)} \right)^2 ; & t < t_D \\[3ex]
k_{2,c} \left(\dfrac{k_{1,c}}{k_{2,c}(\exp(k_{1,c}(t-t_D))-1)+\frac{k_{1,c}}{N_{1,c}}\exp(k_{1,c}(t-t_D))} \right)^2 ; & t \geq t_D
\end{cases}
\end{aligned}
\tag{6.13}
$$

Again, the excitation is considered instantaneous. By integrating **Equation 6.13** the PLQY for the double-pulse excitation is found to be:

$$PLQY_{c,2} = \frac{\int_0^\infty k_{1,c} n_c'^2(t)\,dt}{N_{0,A} + N_{0,B}} \tag{6.14}$$

$$= \frac{\left(\exp(k_{1,c}t_D)\left(\frac{k_{1,c}^2}{k_{2,c}} + N_{0,A}k_{1,c}\right) - t_D\exp(k_{1,c}t_D)\left(\frac{k_{1,c}^3}{k_{2,c}} + N_{0,A}k_{1,c}^2\right) + N_{0,A}k_{1,c}^2 t_D \right)}{(N_{0,A} + N_{0,B})(k_{1,c}\exp(k_{1,c}t_D) - N_{0,A}k_{2,c} + N_{0,A}k_{2,c}\exp(k_{1,c}t_D))}$$

$$+ \frac{-\left(\begin{array}{c}(k_{1,c}\ln(k_{1,c}\exp(k_{1,c}t_D) - N_{0,A}k_{2,c} + N_{0,A}k_{2,c}\exp(k_{1,c}t_D))) \\ + (k_{1,c} + N_{0,A}k_{2,c} + k_{1,c}\ln(k_{1,c})) \end{array} \right)}{(N_{0,A} + N_{0,B})k_{2,c}}$$

$$+ \frac{\left(k_{2,c}N_{1,c} + k_{1,c}\ln\left(\frac{k_{1,c}}{k_{1,c}+k_{2,c}N_{1,c}}\right) \right)}{(N_{0,A} + N_{0,B})k_{2,c}}$$

For $t_D \to \infty$ this equation simplifies vastly to:

$$PLQY_{c,2}$$
$$\to \frac{PLQY_{c,1}(N_{0,A}) \times N_{0,A} + PLQY_{c,1}(N_{0,B}) \times N_{0,B}}{N_{0,A} + N_{0,B}}$$
$$= \frac{\left(N_{0,A} + k_{1,c}\ln\left(\frac{k_{1,c}}{k_{1,c}+k_{2,c}N_{0,A}}\right)\right) + \left(N_{0,B} + k_{1,c}\ln\left(\frac{k_{1,c}}{k_{1,c}+k_{2,c}N_{0,B}}\right)\right)}{N_{0,A} + N_{0,B}}$$

$$\tag{6.15}$$

Calculating the relative PLQY from **Equation 6.14** and **Equation 6.15** by simply dividing the results leads to:

$$rPLQY_c(t_D) = \frac{PLQY_{c,2}(t_D)}{PLQY_{c,2}(t_D \to \infty)} \tag{6.16}$$

$$= \frac{\left(k_{2,c} \times \frac{\left(\begin{array}{c} \exp(k_{1,c}t_D)\left(\frac{k_{1,c}^2}{k_{2,c}} + N_{0,A}k_{1,c} \right) \\ - t_D \exp(k_{1,c}t_D)\left(\frac{k_{1,c}^3}{k_{2,c}} + N_{0,A}k_{1,c}^2 \right) + N_{0,A}k_{1,c}^2 t_D \end{array} \right)}{(k_{1,c}\exp(k_{1,c}t_D) - N_{0,A}k_{2,c} + N_{0,A}k_{2,c}\exp(k_{1,c}t_D))} - \left(\begin{array}{c} (k_{1,c}\ln(k_{1,c}\exp(k_{1,c}t_D) - N_{0,A}k_{2,c} + N_{0,A}k_{2,c}\exp(k_{1,c}t_D))) \\ + (k_{1,c} + N_{0,A}k_{2,c} + k_{1,c}\ln(k_{1,c})) \\ + \left(k_{2,c}N_{1,c} + k_{1,c}\ln\left(\frac{k_{1,c}}{k_{1,c}+k_{2,c}N_{1,c}} \right) \right) \end{array} \right) \right)}{k_{2,c}\left(N_{0,A} + k_{1,c}\ln\left(\frac{k_{1,c}}{k_{1,c}+k_{2,c}N_{0,A}} \right) \right) + k_{2,c}\left(N_{0,B} + k_{1,c}\ln\left(\frac{k_{1,c}}{k_{1,c}+k_{2,c}N_{0,B}} \right) \right)}$$

There is a stark contrast in the PL emission behavior from free charge carriers compared to excitons. The emission becomes stronger rather than weaker when the delay time decreases. The relative PLQY for free carriers dependent on the time delay is displayed in **Figure 6.4b**. What is immediately apparent is that the relative PLQY is consistently above unity and only approaches unity for long delay times. Interestingly, the relative PLQY decreases as the initial density of carriers increases. This is due to the nonlinear radiative recombination pathway becoming dominant. Once all carriers recombine radiatively, further increase in the fluence will not increase the PLQY and therefore also lead to a constant relative PLQY at unity. The same goes for the case with excitons: the relative PLQY curves are unique, meaning that a single curve is
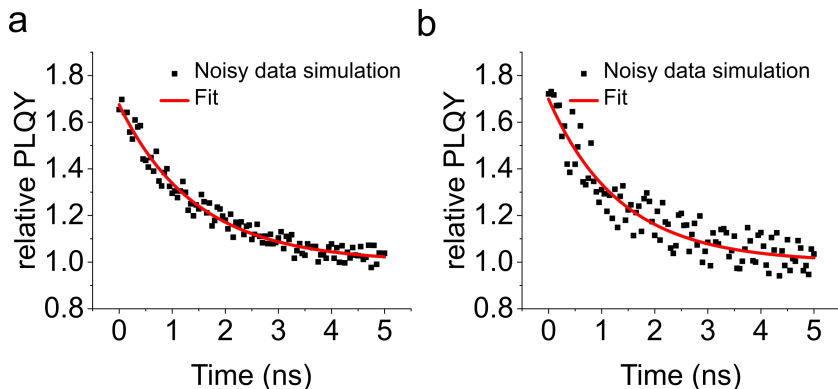
FIGURE 6.5: Illustration of the unique extracted parameters by simulating noisy data by multiplying simulated points with a random number between a) 0.95 and 1.05 and b) 0.9 and 1.1. The parameters used are: $k_{1,c} = 70 \times 10^7 \, \text{s}^{-1}$; $k_{2,c} = 5 \times 10^{-10} \, \text{cm}^3 \, \text{s}^{-1}$ and $N_0 = 5 \times 10^{17} \, \text{cm}^{-3}$. The fitting results didn't change with different starting points and are a) $k_{1,c} = (67 \pm 2) \times 10^7 \, \text{s}^{-1}$; $k_{2,c} = (5.2 \pm 0.2) \times 10^{-10} \, \text{cm}^3 \, \text{s}^{-1}$ and b) $k_{1,c} = (72 \pm 4) \times 10^7 \, \text{s}^{-1}$; $k_{2,c} = (5.0 \pm 0.5) \times 10^{-10} \, \text{cm}^3 \, \text{s}^{-1}$

enough to extract the rate constants when the initial excited-state density is known. Similar to the exciton case, this principle is shown in **Figure 6.5**.

Since exceedingly high excitation fluences lead to a constant relative PLQY at unity or even to Auger recombination which is not accounted for in this model, care has to be taken to choose a suitable excitation fluence. It has to be high enough to reach a good signal to noise ratio but not so high that the relative PLQY becomes time-independent or Auger recombination starts to become significant. A good initial estimate should be where the bimolecular recombination and the trapping are equal. This allows for a good signal and at the same time is low enough so clear changes in the PLQY can be observed.

6.2.3 Exciton and Free Charge Carrier Photoluminescence

In the previous **Chapter 5**, it was established that both excitons and free carriers can simultaneously contribute to the PL emission in quasi-2D perovskites. While this is a special case; the investigation via double-pulse excitation can still be applied. The PL emission is simply a linear combination of the two cases as established in the previous chapter:

$$PL = fPL_x + (1-f)PL_c, \tag{6.17}$$

where f is the fraction of excitonic PL emission. For the PLQY it simply follows that:

$$PLQY = fPLQY_x + (1-f)PLQY_c, \tag{6.18}$$

For the interested reader the masterequation which combines both excitonic and free carrier recombination is given here:

$$rPLQY(t_D) = \frac{f \times PLQY_{x,2}(t_D) + (1-f) \times PLQY_{c,2}(t_D)}{f \times PLQY_{x,2}(t_D \to \infty) + (1-f) \times PLQY_{c,2}(t_D \to \infty)} \quad (6.19)$$

$$= \frac{\left(\begin{array}{l} f \times \left(\frac{k_x \phi}{\gamma_{EEA}} \left(\begin{array}{l} \ln(k_x \exp(k_x t_D) - \gamma_{EEA} N_{0,A} + \gamma_{EEA} N_{0,A} \exp(k_x t_D)) \\ \quad - k_x t_D - \ln(k_x) + \ln\left(\frac{k_x + \gamma_{EEA} N_{1,x}}{k_x}\right) \end{array} \right) \right) \\[2em] + (1-f) \times \\[1em] \left(\begin{array}{l} \frac{-\left(\exp(k_{1,c} t_D) \left(\frac{k_{1,c}^2}{k_{2,c}} + N_{0,A} k_{1,c} \right) - t_D \exp(k_{1,c} t_D) \left(\frac{k_{1,c}^3}{k_{2,c}} + N_{0,A} k_{1,c}^2 \right) + N_{0,A} k_{1,c}^2 t_D \right)}{(k_{1,c} \exp(k_{1,c} t_D) - N_{0,A} k_{2,c} + N_{0,A} k_{2,c} \exp(k_{1,c} t_D))} \\[2em] - \frac{\left(\begin{array}{l} (k_{1,c} \ln(k_{1,c} \exp(k_{1,c} t_D) - N_{0,A} k_{2,c} + N_{0,A} k_{2,c} \exp(k_{1,c} t_D))) \\ + (k_{1,c} + N_{0,A} k_{2,c} + k_{1,c} \ln(k_{1,c})) \\ \quad - k_{2,c} N_{1,c} - k_{1,c} \ln\left(\frac{k_{1,c}}{k_{1,c} + k_{2,c} N_{1,c}}\right) \end{array} \right)}{k_{2,c}} \end{array} \right) \end{array} \right)}{\left(\begin{array}{l} f \times \left(\phi \frac{k_x}{\gamma_{EEA} \left(\ln\left(\frac{k_x + \gamma_{EEA} N_{0,A}}{k_x}\right) + \ln\left(\frac{k_x + \gamma_{EEA} N_{0,B}}{k_x}\right) \right)} \right) + (1-f) \\[2em] \times \left(\left(N_{0,A} + k_{1,c} \ln\left(\frac{k_{1,c}}{k_{1,c} + k_{2,c} N_{0,A}}\right) \right) + \left(N_{0,B} + k_{1,c} \ln\left(\frac{k_{1,c}}{k_{1,c} + k_{2,c} N_{0,B}}\right) \right) \right) \end{array} \right)}$$

This monster of an equation is not meant to give an overview of the method but rather for the interested reader to incorporate into their work. The method is demonstrated experimentally below on quasi-2D perovskites which were also used in **Chapter 5** that adds unique data further supporting the conclusions from the previous work. Most perovskite films do not support both excited state species and either support excitons or free charge carriers. To illustrate the validity of the method,

additionally, TRPL utilizing a streak camera is compared to the intro-
duced method, leading to very similar results.

6.3 Experimental data

To demonstrate the use of the double-pulse technique, a variety of dif-
ferent quasi-2D perovskites is analyzed regarding their photophysical
behavior. As these materials have already been intensively studied in
Chapter 5, the gained knowledge is used in advancing the analysis
technique. For the measurements, the same kind of perovskites as in
the previous chapter are used consisting of $CsPbBr_3$ with the addition
of either butylamine bromide (BABr) or 1-naphthylmethylamine bro-
mide (NMABr) added to the precursor, resulting in a perovskite struc-
ture formula of $CsPbBr_3(BABr)_y$, where y is between 0.4 and 1.0. In
the previous chapter, it was shown that high concentrations of BA lead
to the dominance of excitons while low concentrations of BA lead to a
mixture of noninteracting pools of excitons and free carriers while using
NMA as a spacer molecule leads to the dominance of free charge car-
riers. This conclusion is consistent with previous work on perovskites
in the Dion-Jacobson phase utilizing p-xylylenediamine spacers [148]
In this section, it will be demonstrated how the rate constants which de-
scribe the photophysics of the excited-states can be extracted with the
double-pulse technique from highly complex systems, as is the case for
quasi-2D perovskites. Not only is this possible when excitons or free
carriers are dominating the kinetics, but also in the peculiar case when
both species contribute to the PL emission. The technique is thereby in-
teresting for a wide range of potential applications involving perovskite
structures.

The excited-state lifetimes in the quasi-2D perovskites examined in this
section are very short and typically below 10 ns. Rather than using a
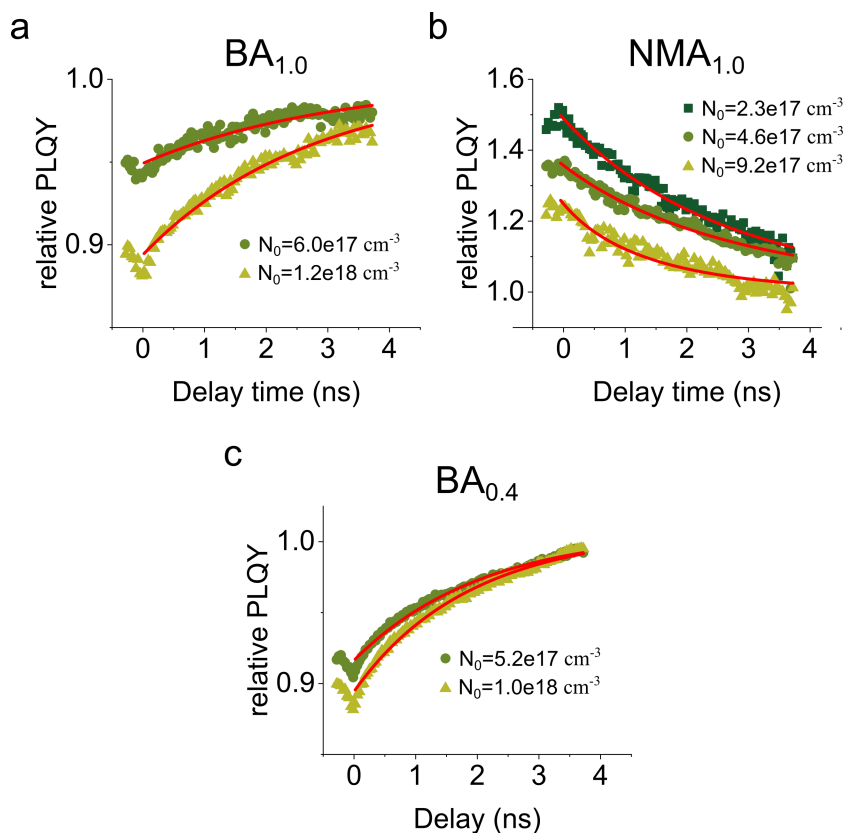
FIGURE 6.6: Relative PLQY curves for the a) $BA_{1.0}$ b) $NMA_{1.0}$ and c) $BA_{0.4}$ perovskites at different fluences.

delay generator as illustrated in **Figure 6.1**, a linear translation stage with an attached retroreflector to control the delay is used which allows for delays up to 4 ns. For 3D perovskites with much longer lifetimes, a delay generator is sufficient.

To calculate the relative PLQY during the measurements the TIPL after a double-pulse excitation is divided by the TIPL of a single-pulse excitation. This is possible since both pulses are set to contain the same fluence. The chosen repetition rates for the pulse trains are 1 kHz for the perovskites made with the NMA spacer and 100 Hz for the ones with the BA spacer. Choosing these low repetition rates ensures that all excited states created by a given pulse pair will have recombined before the next excitation pair arrives after 1 ms or more later [43]. The integration time for the CCD used to record the TIPL is set at 80 ms with ten averages taken of the quasi-steady state per data point. The fitting of the relative PLQY curves is done using **Equation 6.19**. The excitation wavelength of the laser pulses is 430 nm.

6.3.1 Exciton Excited State Population

The clear differences in the TIPL results for the perovskites utilizing either BA or NMA spacers are in complete agreement with the conclusions of the previous chapter, where NMA-perovskites support the dominance of free charge carriers and BA-perovskites either consist of mainly excitons or a mixture of excitons and free carriers depending on the spacer concentrations. The relative PLQY curves are displayed in **Figure 6.6**. As with the simulations in the previous section, the analysis of the experimental data is first done on the quasi-2D perovskite in which excitons dominate the excited-state population which is the $BA_{1.0}$ perovskite. In the previous chapter, this perovskite is found to only support excitons and no free charge carriers. For this reason, the fraction f of QWs supporting excitons is kept at 100% during the fitting process. The relative PLQY, depending on the delay between the pulse trains, is depicted in **Figure 6.7**.
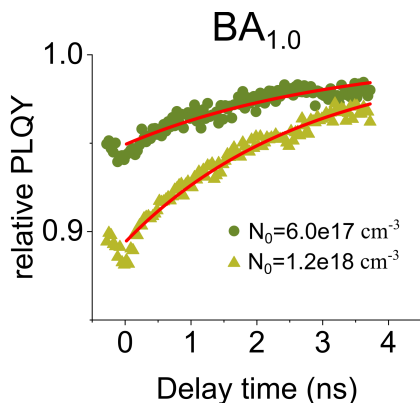
FIGURE 6.7: Relative PLQY over the time delay between the two excitation pulses for the $BA_{1.0}$ perovskite at different excitation fluences. The extracted parameters are $k_x = (33 \pm 2) \times 10^7 \, \text{s}^{-1}$ and $\gamma_{EEA} = (0.8 \pm 0.1) \times 10^{-10} \, \text{cm}^3 \, \text{s}^{-1}$

This result is very similar to the simulation for excitons from the previous section. With higher densities and shorter time delays, the relative PLQY is low. With increasing time delays, the relative PLQY moves back towards unity. Time delays leading to a relative PLQY of one indicate that the excited state species of the first pulse have fully recombined when the second pulse gets absorbed. The curves are individually fitted with the initially excited state density calculated from the absorption, film thickness, excitation fluence, and wavelength. The extracted parameters are the mean values from these fittings with statistical errors. The fitting considering only excitons is shown in red in **Figure 6.7** and works with the measured data, leading to the mean extracted parameters from the two curves of: $k_x = (33 \pm 2) \times 10^7 \, \text{s}^{-1}$ and $\gamma_{EEA} = (0.8 \pm 0.1) \times 10^{-10} \, \text{cm}^3 \, \text{s}^{-1}$ with statistical errors.

To examine if it is valid for the fraction f to be constrained at 100%,
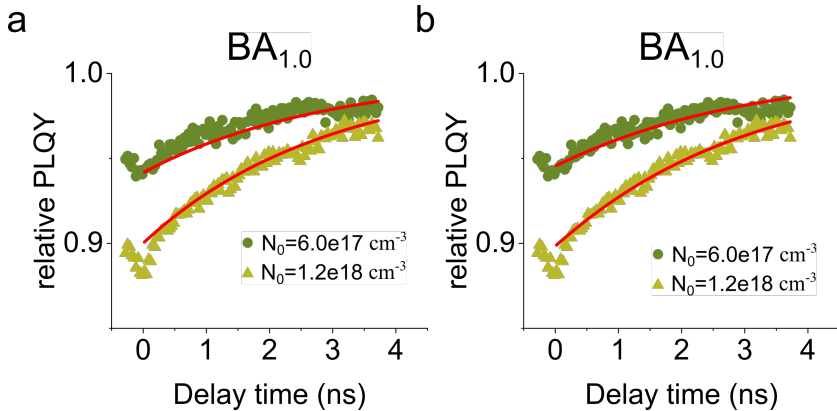
FIGURE 6.8: Relative PLQY curves and global fitting (for comparability) considering a) only excitons and b) f as a free parameter. As derived in **Equation 6.19**, the fit of the mixed relative PLQY depends on the ratio of nonradiative and radiative exciton recombination. The reduced χ^2 is within a factor of two (2.6×10^{-5} for a) and 1.9×10^{-5} for b)), indicating that the fit with more parameters is only potentially marginally better. It should be noted that these reduced χ^2 values are significantly under unity as the unknown uncertainty for each data point of the relative PLQY was considered to be unity. Therefore the relative change in reduced χ^2 can be meaningfully considered but the absolute values are not meaningful. The fit in b) leads to an exciton fraction of 83%; however, the fit leads to unreasonable fitting uncertainties which are: $k_{1,c} = (20 \pm 100) \times 10^7 \, \text{s}^{-1}$; $k_{2,c} = (10 \pm 100) \times 10^{-10} \, \text{cm}^3 \, \text{s}^{-1}$; $k_x = (33 \pm 5) \times 10^7 \, \text{s}^{-1}$; $\gamma_{EEA} = (2 \pm 7) \times 10^{-10} \, \text{cm}^3 \, \text{s}^{-1}$ and $f = 0.8 \pm 1$. Therefore, the change in fitting is ascribed to the increased number of free parameters and there is no reason to favor the more complicated mixed fit over the simple exciton-only fit shown in a).

an additional fit with f as a free parameter is compared to the fit with
constrained f. As the fit involving both species contains a significantly
higher amount of parameters instead of fitting the relative PLQY curves
individually, a global fit is used. In this case, all parameters except the
initial density of states are shared. These fits are displayed in **Figure 6.8**.
The extracted value for k_x is noticeably higher than the values observed
for previously examined quasi-2D BA samples, which is likely due to
batch-to-batch variations in the quality of the perovskite films. Despite
this slight difference in the monomolecular recombination parameter,
the results are clear evidence that the double-pulse method works well,
both qualitatively and quantitatively, to extract the parameters describ-
ing the excited-state dynamics in the case of excitonic dominance.

6.3.2 Free Charge Carrier Excited State Population

As concluded in the previous chapter and mentioned above, the domi-
nant excited-state species in NMA-based quasi-2D perovskites is made
up of free charge carriers. To compare the experimental data with the
simulations for free carriers, a perovskite-based on $NMA_{1.0}$ is used for
the double-pulse method. In the overview in **Figure 6.6** as well as in
Figure 6.9 compared with **Figure 6.8** above, the clear differences be-
tween the excited-state species can be observed.

The most obvious difference between the NMA- and BA-based per-
ovskites is how the relative PLQY of the $NMA_{1.0}$ perovskite starts well
above unity for short delay times instead of below unity in the case of
BA. However, for both cases, the relative PLQY moves towards unity
as the delay time increases. With increasing fluence, the offset from
unity decreases for the NMA-perovskite. This observation agrees very
well with the simulations in the respective section. These significant dif-
ferences between the exciton and free carrier-based emission behavior
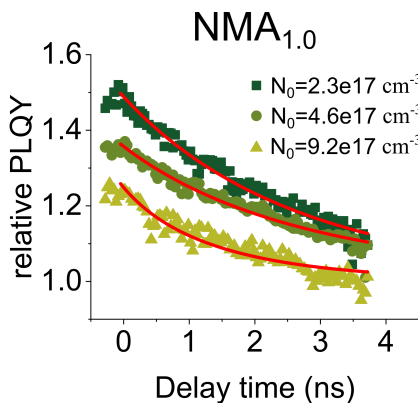
FIGURE 6.9: Relative PLQY over the time delay between the two excitation pulses for the $NMA_{1.0}$ perovskite. The extracted parameters are $k_{1,c} = (38 \pm 6) \times 10^7 \, s^{-1}$ and $k_{2,c} = (14 \pm 2) \times 10^{-10} \, cm^3 \, s^{-1}$

demonstrate the great suitability of this technique in terms of the obvious qualitative differences in the experimental data allowing the revelation of the dominant excited state species as well as the extraction of the rate parameters.

The data is fitted in the same manner as in the previous section. The fraction of the exciton supporting QWs is constrained at 0% which leads to the mean extracted parameters of: $k_{1,c} = (38 \pm 6) \times 10^7 \, s^{-1}$ and $k_{2,c} = (14 \pm 2) \times 10^{-10} \, cm^3 \, s^{-1}$. Again this fit is compared with a fit leaving the exciton fraction as a free parameter. These global fits are presented in **Figure 6.10**. The quality of the fit only slightly improves.

The extracted parameters are well within an order of magnitude agreement with those determined in the previous chapter. The differences in the parameters are again likely due to the considerable batch-to-batch
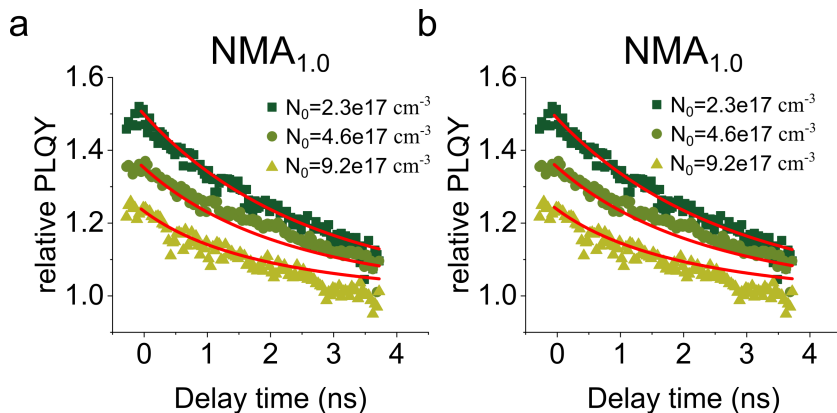
FIGURE 6.10: Relative PLQY curves and global fitting (for comparability) considering a) only free carriers and b) f as a free parameter. As in **Figure 6.8**, only purely radiative exciton decay is assumed. The two fits are similar. The fit in b) leads to a free carrier fraction of 98.4%, the parameters are: $k_{1,c} = (33 \pm 3) \times 10^7 \, \text{s}^{-1}$; $k_{2,c} = (12 \pm 1) \times 10^{-10} \, \text{cm}^3 \, \text{s}^{-1}$; $k_x = (0 \pm 6) \times 10^7 \, \text{s}^{-1}$; $\gamma_{EEA} = (0.0 \pm 0.4) \times 10^{-10} \, \text{cm}^3 \, \text{s}^{-1}$ and $f = 0.016 \pm 0.008$. Therefore, the change in fitting is ascribed to the increased number of free parameters. The reduced χ^2 is on the same order of magnitude being 7.2×10^{-4} for a) and 7.1×10^{-4} for b). As in Figure **Figure 6.8**, it should be noted that these reduced χ^2 values are significantly under unity as the unknown uncertainty for each data point of the relative PLQY was considered to be unity.

variations in these highly disordered quasi-2D perovskites. These experimental data demonstrate that in perovskites in which the dominant species is made up of free charge carriers, the dynamics can be qualitatively and quantitively described and the rate parameters can be well extracted via the double-pulse technique.

6.3.3 Excitons and Free Charge Carrier Excited State Populations

After establishing that the double-pulse technique works well for both excitons and free charge carriers; in this section, the unique situation in which both excited-state species contribute to the PL emission as observed for low BA concentrations in the previous chapter is examined. In this special case, the PL emission is due to two separate independent pools of excited-state species located in locally separated low bandgap QWs. This is described in more detail in the previous chapter. The total emission of the perovskite sample after excitation can be treated as a weighted sum of the emission from excitons and free carriers.

The experimental data of a sample showing emission from both excited species based on $BA_{0.4}$ is depicted in **Figure 6.11**.

This data looks very similar to the exciton-dominated case of the $BA_{1.0}$-based perovskite depicted in **Figure 6.7** and also similar to that case the relative PLQY is lowest at zero delay and approaches unity as the delay is increased. Therefore, it is likely that excitons make up a considerable portion of the excited-state population. There is, however, additional qualitative information not consistent with excitons being the sole excited-state species. The relative PLQY at zero delay is only minorly reduced and increasing excitation fluences do not reduce the relative PLQY to the expected extent compared to an exciton-dominated perovskite. The additional reduction with fluence is significantly lower compared to the $BA_{1.0}$-based perovskites. Doubling the fluence leads to hardly a decrease at zero delay time. Additionally, the two curves cross. The higher fluence curve starts below the other curve at shorter delays and crosses the lower fluence curve as the delay time increases leading to a higher relative PLQY at long delays for the high fluence curve.
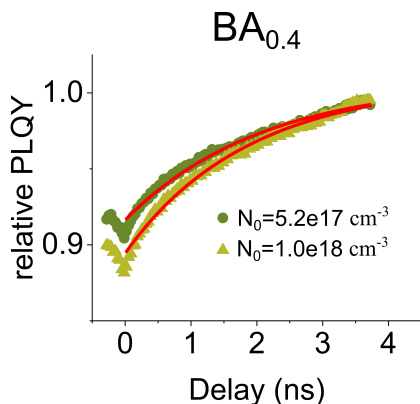
FIGURE 6.11: Relative PLQY over the time delay between the two excitation pulses for the $BA_{0.4}$ perovskite. The extracted parameters are $k_{1,c} = (24 \pm 2) \times 10^7 \, s^{-1}$; $k_{2,c} = (3.0 \pm 0.5) \times 10^{-10} \, cm^3 \, s^{-1}$; $k_x = (39 \pm 2) \times 10^7 \, s^{-1}$; $\gamma_{EEA} = (4.8 \pm 0.4) \times 10^{-10} \, cm^3 \, s^{-1}$ and $f = (70.3 \pm 0.3)\%$

Again these curves cannot be fitted individually as the amounts of parameters are too high for reliable fits leading to unreasonable uncertainties. The fitting is therefore done by sharing the parameters for the curves (global fitting) to extract the rate constants. Constraining the excited-state population so that only free charge carriers are considered is not sensible in this case, as the relative PLQY does not exceed unity at any point and only increases with increasing delay. Similarly constraining the excited-state species to consist only of excitons does not lead to reasonable results as shown in **Figure 6.12**.

The figure considering both excited-state species significantly improves the fit quality compared to the case in which only excitons are considered. The extracted parameters are: $k_{1,c} = (24 \pm 2) \times 10^7 \, s^{-1}$; $k_{2,c} = (3.0 \pm 0.5) \times 10^{-10} \, cm^3 \, s^{-1}$; $k_x = (39 \pm 2) \times 10^7 \, s^{-1}$; $\gamma_{EEA} =$
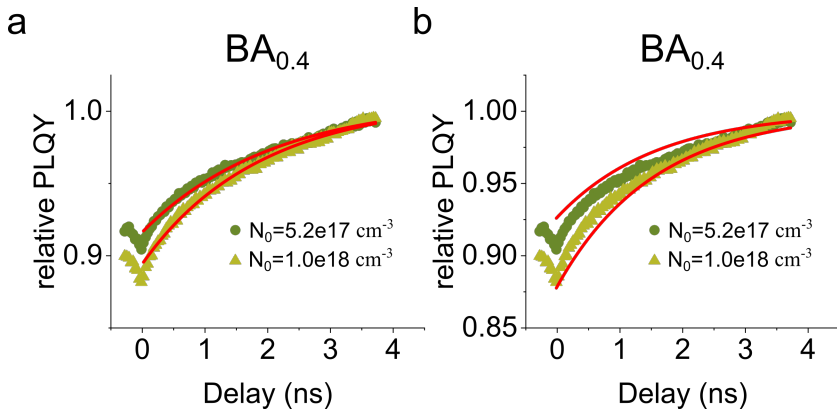
FIGURE 6.12: Relative PLQY curves and global fitting (for comparability) considering a) only free carriers and b) f as a free parameter. As in **Figure 6.8** and **Figure 6.10**, a purely radiative exciton decay is assumed. The fit in b) only works moderately well. The parameters for a) are: $k_{1,c} = (24 \pm 2) \times 10^7 \, \text{s}^{-1}$; $k_{2,c} = (3.0 \pm 0.5) \times 10^{-10} \, \text{cm}^3 \, \text{s}^{-1}$; $k_x = (39 \pm 2) \times 10^7 \, \text{s}^{-1}$; $\gamma_{EEA} = (4.8 \pm 0.4) \times 10^{-10} \, \text{cm}^3 \, \text{s}^{-1}$ and $f = (70.3 \pm 0.3)\%$; and for b) they are: $k_x = (62 \pm 1) \times 10^7 \, \text{s}^{-1}$; $\gamma_{EEA} = (2.2 \pm 0.1) \times 10^{-10} \, \text{cm}^3 \, \text{s}^{-1}$. The qualitative difference between the two fits can also be illustrated by the difference in the reduced χ^2, which is 6.6×10^{-6} for a) and 4.8×10^{-5} for b). The reduced χ^2 is an order of magnitude better for the mixed fit shown in a), indicating that the mixed model is significantly better than the exciton-only model in this case. It should be noted that these reduced χ^2 values are significantly under unity as the unknown uncertainty for each data point of the relative PLQY was considered to be uniform and unity (a significant overestimate chosen to keep the denominator unity). Therefore the relative change in reduced χ^2 can be meaningfully considered but the absolute values are not meaningful. The fact that the absolute value of the reduced χ^2 is not being meaningful can is obvious, as there are significant deviations of the fit from the data in panel b), indicating that with proper knowledge of uncertainties and weighting the reduced χ^2 would significantly exceed one in this case. Irrespective, the minimization routine and the relative comparison of reduced χ^2 are valid.

$(4.8 \pm 0.4) \times 10^{-10}\,\mathrm{cm^3\,s^{-1}}$ and $f = (70.3 \pm 0.3)\%$. It should be noted that as for the previous global fits the uncertainties are not statistical but rather result from the fitting itself and thereby likely underestimate the real uncertainties. In this special case, it is advisable to commit to a fluence-dependent measurement and not to rely on a single curve to extract the rate constants. The fit depends on the ratio of radiative to nonradiative monomolecular exciton recombination, as is derived in **Equation 6.19**. This ratio and the fraction of exciton-dominated QWs, f, are directly dependent while all other parameters are unaffected were this ratio to be changed. In this chapter, all monomolecular excitonic recombination is assumed to be radiative which leads to an underestimation of the fraction of excitonic QWs, f. Compared to the extracted parameters for excitons from the previous chapter, the rate constants found are an order of magnitude higher. This deviation is ascribed to batch-to-batch variations in the perovskite film quality. For the free charge carriers, however, the parameters are similar to the ones determined in the previous chapter and as is the fraction of exciton dominated QWs, f. The technique utilizing two excitation pulses not only allows for the extraction of the rate constants in perovskites supporting only excitons or only free carriers but also for the very special case of both species contributing to the PL.

For the interested reader, the conclusion that the $BA_{0.4}$-based perovskite supports both excited-state species while the other samples only support one is further supported by carefully considering the normalized PL spectra of the samples examined in this chapter as a function of fluence. These data are shown in **Figure 6.13**.

The normalized spectra for both the $BA_{1.0}$ and $NMA_{1.0}$ based perovskites do not change with fluence. For a single excited-state species this is entirely expected and applies to both cases. The PL peak for the $BA_{1.0}$ perovskite is at 2.43 eV and the PL peak of the $NMA_{1.0}$ perovskite
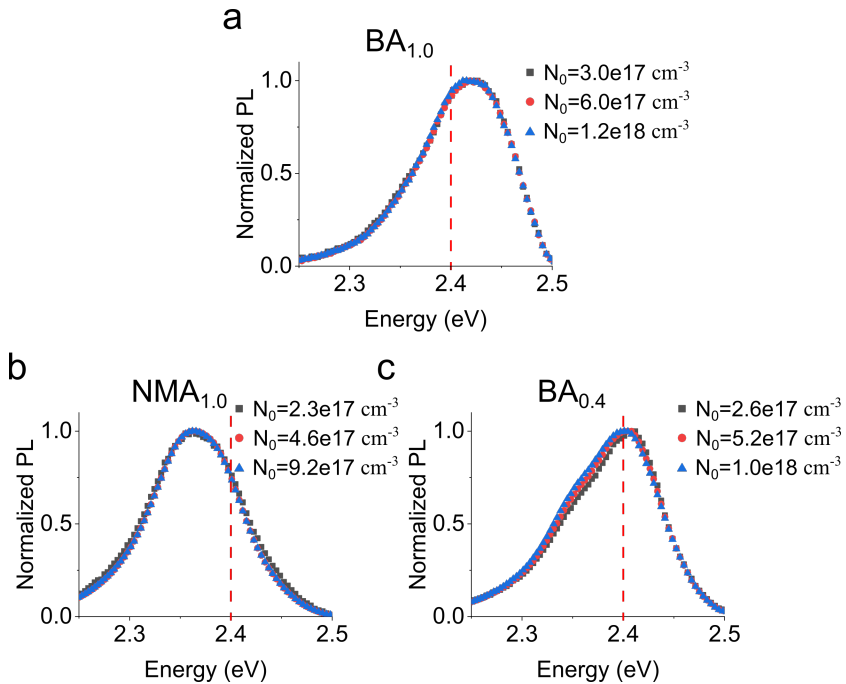
FIGURE 6.13: Normalized time-integrated PL spectra of the a) $BA_{1.0}$, b) $NMA_{1.0}$, and c) $BA_{0.4}$ spacer perovskites. The dotted line at $2.4\,eV$ is a guide to illustrate the different peak positions of the samples. While only minor changes with fluence are observed for most samples, $BA_{0.4}$ shows an emerging shoulder at $2.36\,eV$ to $2.37\,eV$ with an increasing initial density of excited states.

is at $2.36\,eV$. The lower energy emission for free charge carriers again is consistent with the conclusions of the previous chapter whereby lower bandgap QWs are more likely to support free carriers. In the $BA_{0.4}$ based perovskite, however, both excited-state species contribute to the

PL. As the emission efficiencies of the two species depend on the fluence with higher fluences improving the efficiency for free carriers and decreasing it for excitons, the normalized PL spectra are expected to change with fluence as the free carrier emission becomes the more dominant contributor. Looking at **Figure 6.13**, this is indeed the case as the lower energy shoulder becomes more dominant with higher excitation fluences. The energy of the lower energy shoulder is also consistent with the free carrier emission observed in the $NMA_{1.0}$ based perovskite. The behavior of the PL spectra as a function of fluence is consistent and supports the findings of the analysis above utilizing the double-pulse technique.

6.3.4 Application to 3D Perovskite Photovoltaic Layers

In the previous section, it was established that the excited-state dynamics of quasi-2D perovskites can be characterized using the double-pulse method. This characterization is valid in the case of complete dominance by either excited-state species as well as in the uncommon case that both species contribute to the PL emission. In this section, the application for 3D-perovskites with much slower dynamics is highlighted and the potential application of the double pulse technique for in-line characterization of the charge carrier dynamics in photovoltaic layers is discussed as a cheap method potentially only involving LEDs and a spectrometer. The exemplary 3D perovskite used here is $Cs_{0.18}FA_{0.82}PbI_3$, with and without a passivation layer based on adding phenethylammonium chloride (PEACl) to the perovskite precursor, which forms heterogeneous 2D Ruddlesden–Popper (RP) $(PEA)_2(Cs_{1-x}FA_x)_{n-1}Pb_n(I_{1-y}Cl_y)_{3n+1}$ layers where n~1-2 at the grain boundaries and the surface of the film. These passivations have been used in the fabrication of MA-free solar cells reaching power conversion efficiencies exceeding 22% [149]. The much lower recombination rates

in these materials necessitate significantly longer delays and lower pulse fluences. Instead of using a retroreflector and a linear translation stage as done above, a digital delay generator is used with an additional introduced actively Q-switched laser with a 0.6 ns pulse width. This allows for a wide range of possible delays to be set from only a few picoseconds up to milliseconds. For the comparison with the double-pulse technique, the TRPL is measured with a streak camera after the excitation with the Q-switched laser at various fluences. The charge carrier dynamics are then determined via fitting of the individual curves. In these materials, excitons are not considered due to their low exciton binding energies so the excited-state population only consists of free carriers.

The data from the TRPL- and the double-pulse measurements for both the passivated and the unpassivated samples are displayed in **Figure 6.14**. To give an appropriate estimation of the parameter uncertainties the fluence series for each sample was remeasured three times. All measurements were taken in an atmospheric environment. Shown in **Figure 6.14** is the mean and the standard deviation of each data point resulting from the three measurements. To best estimate, the rate constants and their uncertainties each of the nine data sets are fitted individually (three for each fluence). The red lines in **Figure 6.14** show the curves resulting from the mean values from the extracted parameters. The parameters are summarized in **Table 6.1**

In **Figure 6.14** and **Table 6.1**, it should be noted that the uncertainty from the measurement of the unpassivated material and its associated parameters is noticeably higher, which is attributed to the higher instability of the material under prolonged light exposure. This is illustrated in **Figure 6.15** where the curves differ depending on the point in time at which they were taken. This systemic error, based on the light-soaking like effect is observed in the unpassivated sample; not, however, in the repeat measurements of the more stable passivated one. In the current
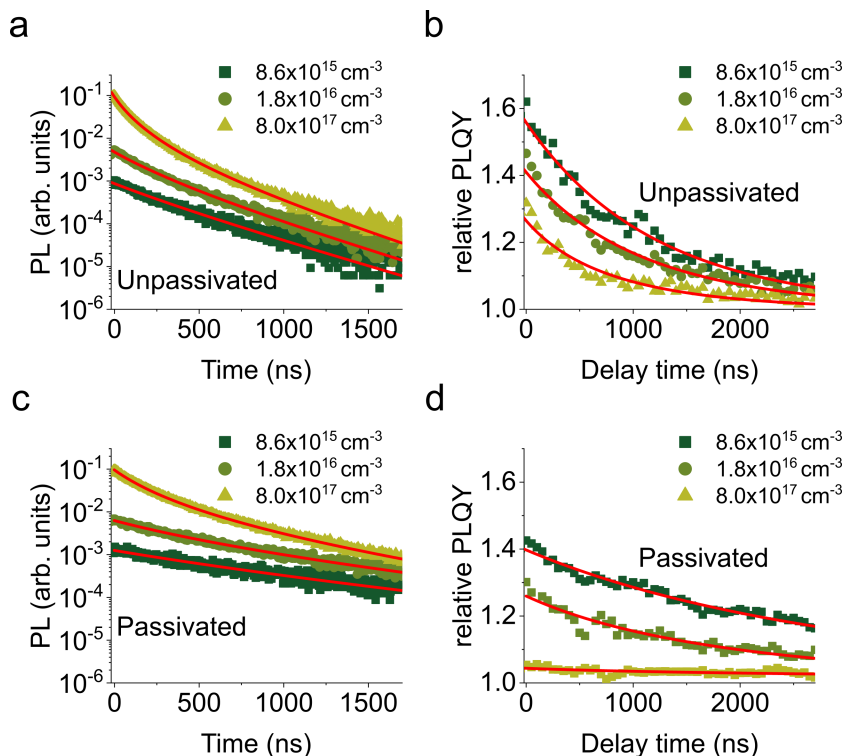
FIGURE 6.14: Comparison of the rates extracted from TRPL measurements utilizing a streak camera and from the relative PLQY for an unpassivated sample (a, b) and a passivated sample (c, d). A single passivated and an unpassivated sample are used. The measurement method is swapped after each series of measurements of three fluences. This whole procedure is repeated three times to get three measurements for each method for each fluence. The nine data sets per sample are individually fitted, giving nine estimates of the extracted parameters from which the mean and uncertainty for each parameter can be estimated. These are shown in **Table 6.1**. The data shown represent the mean and standard deviation at each point based on the three separate measurements for each fluence.

a

b
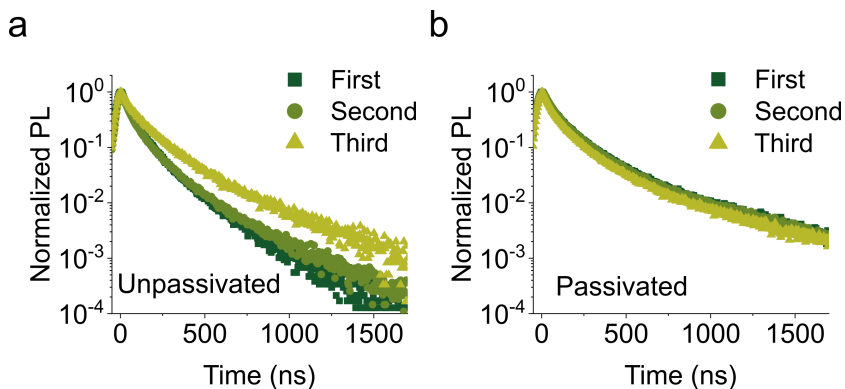
FIGURE 6.15: Normalized TRPL curves at the highest measured excited state density ($N_0 = 1 \times 10^{17}\,\mathrm{cm}^{-3}$) of the three measurements taken at different times for the a) unpassivated and b) passivated 3D perovskites. A noticeable increase in the PL lifetime is observed for the unpassivated perovskite. Although this is a systematic error in the sense that the material responds to prolonged illumination, it can be estimated that, in the worst case, it will be a random variable in an in-line application wherein the total illumination dose may not be carefully controlled as described in the text.

estimation of the uncertainties in the extracted parameters, the achievability in an in-line monitoring system where the exposure to light might not be rigorously controlled is considered. This systematic error based on the light-induced changes is therefore considered as a random error that might occur in an in-line system with poorly controlled light exposure.

The uncertainty of the extracted parameters determined in this fashion is 40% for the unpassivated sample and is similar in both methods, streak, and double-pulse. In the passivated material the uncertainty is below 25%. It is estimated that by controlling systematic errors in an in-line

environment a parameter error of 25% or below can be achieved. For
this work, it is crucial that the relative uncertainties of the used methods
are equivalent to the double-pulse technique and the streak measurement
and the extracted parameters are within their uncertainties.

The monomolecular recombination rate extracted from the passivated
sample, $k_{1,c}$, is significantly lower than the one from the unpassivated
material. Since the purpose of the passivation is the reduction of traps
at the interfaces and grain boundaries, this result is very much ex-
pected [149]. With both methods, only a minor reduction in $k_{2,c}$ is
observed after the passivation. This again is expected, as the passiva-
tion has no significant effect on the carrier transport inside the grains
which maintains the high photovoltaic performance. This analysis gives
a good indication that the double-pulse technique could be a useful tool
in the in-line inspection of solar cell materials giving a rough prediction
of their carrier dynamics.

TABLE 6.1: Fitting parameters obtained from the fits shown in **Figure
6.15**.

Method	$k_{1,c}$ (10^6 s^{-1})		$k_{2,c}$ (10^{-11} cm^3 s^{-1})	
	Unpassivated	Passivated	Unpassivated	Passivated
TRPL	1.1 ± 0.4	0.43 ± 0.09	10 ± 4	8 ± 1
double pulse	1.0 ± 0.4	0.6 ± 0.1	9 ± 2	6 ± 1

In addition, to compare the methods, the results above are useful in the
consideration of which light sources can be used to perform the double-
pulse measurement in an in-line environment for perovskite solar cells.
The rule of thumb selection of appropriate pulse length and excitation
fluence can be gathered from the presented data above. Considering the

fluence to best examine the dynamics of charge carriers, there is no theoretical lower bound for the pulse fluence. The change in the relative PLQY is largest for low-energy pulses as the emission increases with the square of the carrier density. However, it should be considered that weak emission of PL leads to an unfavorable signal to noise ratio so care has to be taken to choose an appropriate fluence. For an optimum compromise between a good signal and a strong response of the relative PLQY, a pulse fluence is suggested for which the trapping rates and the radiative rates are equal at zero time, so that $k_{1,c} \sim k_{2,c}N_0$. The lower fluences in **Figure 6.15b** and **d** corresponds to this estimation with $k_{1,c} \sim 1 \times 10^6 \, \text{s}^{-1} \sim 1 \times 10^{-10} \, \text{cm}^3 \, \text{s}^{-1} \cdot 1 \times 10^{16} \, \text{cm}^{-3} \sim k_{2,c}N_0$. The relative PLQY, in this case, is approximately 1.5 at zero time which is substantial enough for simple fitting. The PL emission is also strong enough to be easily collected. For the excitation to be approximated as impulsive in the fitting, the pulse width should be at least 5 times shorter than the inverse of the total decay rate at zero time. With the estimation above, the total decay rate at zero time is simply $2k_{1,c}$, which for good photovoltaic materials as discussed here is approximately $2 \times 10^6 \, \text{s}^{-1}$. In this case, a pulse as long as 100 ns could be considered as impulsive. It is possible to obtain pulse fluences on the order of 1 µJ from arrays of LEDs with this order of pulse length [150]. A pulse energy of 1 µJ is sufficient to generate a excited-state density of $10^{16} \, \text{cm}^{-3}$ over an illuminated circular area with a radius of approximately 1 mm on a 100 nm thick perovskite film. Recent developments in LED systems based on Li-Fi could be exploited to obtain the desired pulse sequence [151]. Therefore, these estimations based on the results above establish that lower-cost systems based on pulsed LEDs with a controllable time delay between their flashes should be considered for in-line estimation of carrier dynamics in 3D perovskite films for photovoltaics.

6.4 Discussion

This chapter demonstrates that measuring the TIPL after excitation with two temporally separated pulses with controllable delay allows for the facile and precise determination of the dynamics of excitons, free charge carriers, or even a mixture of both in quasi-2D and 3D perovskites.

In previous work, a dependence on the lowering of ASE threshold of quasi-2D perovskites with increased bimolecular free carrier emission has been observed [47]. As the excitation fluence increases, the initial PL emission of free carriers increases with the square of the initial carrier density while at high fluences the emission lifetime decreases. This leads to a high initial photon density which allows for ASE to occur. Promising results in the field of lasing have been achieved with quasi-2D perovskites [31, 152]. Determining the radiative bimolecular rate constant in these materials is an important task to further develop efficient lasing and the presented double-pulse technique could be a great tool for groups with limited access to a streak camera.

Even more relevant is the potential use in the characterization of photovoltaic materials. Determining the free charge carrier recombination pathways and rate constants in the absorption layer of PV devices can reveal the material quality during the cell fabrication process. The device performance is highly dependent on the carrier dynamics which can be measured after the formation of the perovskite active layer before the deposition of the capping charge transport layers. This may provide quality control and feedback to the process parameters in a fabrication line. In terms of measuring the carrier dynamics, the two-pulse method has attractive features in comparison to a method based on a streak camera or time-correlated single photon counting in terms of simplicity and expense of the equipment required, but also in terms of the potential to image the carrier dynamics across the whole area of the sample.

Regarding the simplicity and cost of the equipment, this technique needs two pulses that are short compared to the excited-state lifetime of the sample and arrive with a controllable delay between them. Synchronizing an actively Q-switched laser to a passively Q-switched laser through a delay generator would be a robust and cost-effective solution to generate such a pulse sequence. A simple USB spectrometer is enough to capture the emitted photoluminescence as used above. If the beam size were expanded to cover a large area of the material, the carrier dynamics might be imaged over the whole area using an industrial camera to image the quasi-steady state PL. This would allow for the observation of the change in the emission intensity with the delay time at different positions (camera pixels). These could then be analyzed individually to indicate how uniform the dynamics are. Since these photovoltaic films only need weak excitation fluences to observe significant changes in the emission as the material is dominated by free charge carriers, it should be possible to use LEDs to excite the samples, as discussed above. To apply the double-pulse technique on a larger area, some work needs to be done to develop arrays of synchronously firing LEDs to provide reasonably uniform illumination over the whole sample area (this is likely best achieved as an interweaving of two separate LED arrays with a time delay between them). The possible advantages of this technology in terms of cost, speed, and robust implementation of carrier-dynamic measurements, and the potential to image these, make this an attractive method to further test and develop.

In terms of practical application, the time required to make these measurements is an important aspect for their potential use in-line. In the work presented in this chapter, each measurement consists of 120 measured delay points with each point being exposed to the laser pulse trains for 0.8 s with a background correction of an additional 0.8 s, leading to a total measurement time of slightly over three minutes for the complete

measurement of the relative PLQY as a function of the delay time at a single excitation fluence. The relative PLQY is measured by observing changes in the emission so the PLQY itself does not need to be measured and no integrating sphere is required for this method. Since the relative PLQY curves are unique, a single measurement at a single fluence is enough to estimate the recombination parameters. It should be noted that as a rule of thumb, this fluence should be chosen either through prior knowledge of similar systems or by some initial trial and error, such that the monomolecular and bimolecular decay rates are equal at the excited-state density reached when there is no delay between the pulses. The presented double-pulse technique is thereby favorable in terms of measurement time of a single fluence compared to more traditional methods involving time-resolved detection of the PL. The time required for the measurements can be further improved by investigating faster repetition rates and shorter integration times on the camera, and/or taking fewer data points, and fitting a more sparsely populated curve. In comparison with TRPL techniques that give full time resolution of the excited-state evolution, the more limited information obtained from this time-integrated double-pulse method will never provide as nuanced information on the excited-state dynamics. The method presented is not sufficient to check advanced models in detail that take time dependencies into account and laboratory techniques such as Streak Camera measurements or TCSPC can thereby not be replaced and remain favorable in this case. However, for a rough estimate of the excited-state dynamics with a robust and low-cost system, which is desirable for example in scalable quality control of perovskite photovoltaic layers, distinct advantages and opportunities for further development of the double pulse method are possible.

6.5 Summary

In this chapter, a characterization method is considered to extract the rate constants from the TIPL of different perovskite materials based on the excitation with two laser pulses with a variable temporal delay and the measurement of the relative PLQY changes. The relative PLQY is found to be higher for free carrier dominated PL emission and to decrease with a temporal delay while the relative PLQY for exciton dominated PL emission is found to be lower and to increase with increasing temporal delay. The TIPL of quasi-2D perovskites based on the BA and NMA spacer molecules at different concentrations is analyzed to show the different relative PLQY-curves depending on the dominance of excitons, free charge carriers, or a mixture of the two. The extracted parameters are similar to the ones determined in the previous chapter based on TRPL measurements of the same type of perovskites. Furthermore, the significance of this method for the characterization of photovoltaic materials by considering an unpassivated and a passivated 3D perovskite is demonstrated. To conclude, the simple rate constants of several types of perovskites can be extracted with the double pulse method, which suggests that this technique is attractive for developing "in-line" basic characterization of excited-state lifetimes, especially in perovskite solar cell layers.

7

Conclusion and Outlook

Conclusions

The main purpose of this thesis is to present some insight into the excited states of 2D and quasi-2D perovskites by investigating the photoluminescence (PL) after the excitation with a laser. For the analysis, some fundamental background on the characteristics of excited states is provided with some simple simulations explaining the observed behavior. Furthermore, a new model is introduced to explain the complex proceedings in quasi-2D perovskites. This model is then applied within a measurement technique potentially well suited for fabrication lines or research fields where expensive equipment is not easily accessible. The results from this work give a good indication of which materials best complement which application and how to extract various parameters from the PL emission.

In **Chapter 4** two different phases of widely used 2D perovskites are examined at different temperatures spanning from 5 K up to room temperature. The Ruddlesden-Popper phase of the $(PEA)_2PbI_4$ perovskite and the Dion-Jacobson phase of the $(PDMA)PbI_4$ start to show multiple peaks in the emission spectra as the temperature is decreased. In these materials, excitons make up almost all excited states with the observations being understood in a framework in which an equilibrium is formed between free excitons and bound excitons (excitons bound to

trap sites). At temperatures above $140\,K$, the bound excitons can overcome the binding energy and dissociate into free excitons, resulting in a single emission peak. At lower temperatures, the bound excitons begin to emit themselves. In temperature-dependent measurements, it is found that free excitons are heavily affected by exciton-exciton annihilation decreasing the emission efficiency while the emission from bound excitons slightly benefits. This leads to stronger emission from bound excitons at high excitation fluences in the Ruddlesen-Popper perovskite. This effect is less pronounced in the Dion-Jacobson perovskite but still significant. Additionally, PbI_2 inclusions in both materials are shown to emit at low temperatures with the effect being more pronounced in the Dion-Jacobson phase.

After gaining these insights into the photophysics of purely 2D perovskites and their potential use, **Chapter 5** is focused on the more complex systems of quasi-2D perovskites. These materials are made up of layers of differently sized quantum wells (QW) with the size of these QWs having a strong influence on the exciton binding energy as well as on the band gap energy. A model is introduced explaining the curious time-dependence of the PL emission, whereby excited states funnel towards the lowest energy bandgap QW they can reach and then recombine. Depending on the concentration and type of the spacer molecules used, the low energy QWs either support excitons or free charge carriers which is reflected in the emission characteristics. The spacer molecules used in this work are n-butylamine (BA) and 1-naphthylmethylamine (NMA) which form the quasi-2D perovskite $CsPbBr_3(NMA$ or $BABr)_y$ where y is varied from 0.4 to 1.0. By analyzing the fluence-dependence of the initial emission, the emission efficiency, and the emission lifetime, it is found that the NMA-perovskite emission only consists of radiative free carrier recombination at all examined spacer concentrations while the BA-perovskite emission at high spacer concentrations is fully made

up of radiative exciton recombination. In the special case of low spacer concentrations of BA, the PL can be described by a linear combination of radiative exciton and free carrier recombination. This can be understood as some emitting QWs supporting excitons while others support free carriers which can only occur over a certain spacer concentration range.

Based on these findings in **Chapter 6**, a characterization technique is introduced whereby two excitation pulses with a controllable delay between them are used in combination with a simple USB spectrometer to extract the rate parameters describing the excited-state dynamics from the time-integrated emission spectra. Due to the different PL characteristics of excitons and free carriers, the time-integrated emission either increases (excitons) or decreases (free carriers) with the delay time. The measured data curve consisting of the change in the emission (relative PLQY) dependent on the delay can be fit to extract the rate constants. Again the spacers NMA and BA are used at different concentrations to fabricate quasi-2D perovskites illustrating the clear quantitative and qualitative differences in the relative PLQY curves when only excitons, only free carriers, or a mixture of both make up the emission. The validity of the method is further demonstrated with the characterization of photovoltaic materials by considering an unpassivated and a passivated 3D perovskite. The fast measurement speed and the low cost of this technique are discussed in the context of potential application fields.

To summarize, novel models are introduced describing the dynamics of excited states in 2D and quasi-2D perovskites. Concerning this model, it is discussed how high concentrations of spacer molecules and the choice of that molecule may lead to strong dominance from excitons which can be beneficial for applications regarding light-emitting diodes. Low concentrations and different spacer molecules may lead to the dominance of free charge carriers which, as discussed, may lead to great benefits

in lasing applications. Additionally, an experimental method is introduced to robustly and quickly allow for the assessment of perovskite materials. This promising tool may help in the future to estimate the perovskite film quality and to assess the choice of the used molecules for the regarded application.

Outlook

Perovskites are highly researched nowadays and further research is necessary to advance the understanding and improve on the models presented in this work. While the fitting and the simulations herein work well to describe the observations made in this work, they are vastly simplifying the complexity of the materials. An interesting question that remains unsolved is what the equilibrium between the excited states inside an emitting QW might look like. This work only considers purely excitonic or purely free carrier-based QW, which is a valid simplification but not the true behavior. The equilibrium between excitons and free charge carriers is described by the Saha-equation and is dependent on the temperature. An interesting way to further analyze whether the assumption of exciton and free carrier QWs is valid is by analyzing the time-resolved photoluminescence depending on the temperature. At sufficiently low temperatures excitons should dominate in any QW. This would also allow for the rough estimation of how strong the exciton binding energy needs to be so that either excitons or free carriers dominate. Another way to gain more insight is the observation of highly resolved spectra. As shown in this work the emission wavelength depends on whether a QW is dominated by excitons or by free carriers. As the emission efficiency depends on the excitation fluence, measurement of highly resolved spectra depending on the excitation fluence should allow for similar estimations of the necessary binding energies. Both of these proposed experiments necessitate, however, the knowledge of

the excited-state density inside the emitting QWs. To solve this question, the observation of excited-state dynamics from a single QW crystal with a known thickness might be necessary. The comparison of the time-resolved emission from a single non-layered QW with known absorption with the emission from a layered film might allow for the estimation of the density inside the emitting QWs in a layered film. This would be a remarkable achievement, also creating knowledge about the funneling process as then the amount of funneled excited states could be compared with the expected amount resulting from light absorption. If all these experiments were to be successfully conducted, a complex and advanced model could be created. The now over 100-year-old Saha-equation is very likely correct, however, it only applies if no further states are involved. It is highly unlikely that only two states are enough to fully describe the photophysics of quasi-2D perovskites. In this work the Saha-equation was not considered as the observations made could be described with simplified models. An exact model on the other hand has to consider the equation. From the observations made in this work, this is only possible if additional states, i.e. traps, are involved which requires a more complex and more detailed model solving the differential equations for each state which may only be possible with advanced numerical simulations. Furthermore, the time-resolved photoluminescence only a few picoseconds after the excitation needs to be well analyzed. Three effects seemingly simultaneously affect the dynamics, namely: hot carrier cooling, exciton formation (Saha), and energy funneling. All these effects are very fast relative to the photoluminescence lifetime. These interesting challenges require further work in the future. From this, some fundamental knowledge about the photophysics of these materials could be gained, potentially leading to different approaches in the material composition and application.

References

[1] M. R. Hannah Ritchie and P. Rosado, "Energy," *Our World in Data*, 2020, https://ourworldindata.org/energy.

[2] I. E. Agency, *World Energy Outlook 2021*, 2021. [Online]. Available: https://www.oecd-ilibrary.org/content/publication/14fcb638-en

[3] D. M. Chapin, C. S. Fuller, and G. L. Pearson, "A new silicon p-n junction photocell for converting solar radiation into electrical power," *Journal of Applied Physics*, vol. 25, no. 5, pp. 676–677, 1954. [Online]. Available: https://doi.org/10.1063/1.1721711

[4] A. Kojima, K. Teshima, Y. Shirai, and T. Miyasaka, "Organometal halide perovskites as visible-light sensitizers for photovoltaic cells," *Journal of the American Chemical Society*, vol. 131, no. 17, pp. 6050–6051, 2009, pMID: 19366264. [Online]. Available: https://doi.org/10.1021/ja809598r

[5] D. H. Levi, M. A. Green, Y. Hishikawa, E. D. Dunlop, J. Hohl-Ebinger, and A. W. Y. Ho-Baillie, "Solar cell efficiency tables (version 51)," *Progress in Photovoltaics*, vol. 26, no. 1, 12 2017. [Online]. Available: https://www.osti.gov/biblio/1416522

[6] L. A. Zafoschnig, S. Nold, and J. C. Goldschmidt, "The race for lowest costs of electricity production: Techno-economic analysis of silicon, perovskite and tandem solar cells," *IEEE Journal of Photovoltaics*, vol. 10, no. 6, pp. 1632–1641, 2020.

[7] G. Niu, W. Li, F. Meng, L. Wang, H. Dong, and Y. Qiu, "Study on the stability of $CH_3NH_3PbI_3$ films and the effect of

post-modification by aluminum oxide in all-solid-state hybrid solar cells," *J. Mater. Chem. A*, vol. 2, pp. 705–710, 2014. [Online]. Available: http://dx.doi.org/10.1039/C3TA13606J

[8] J. Yang, B. D. Siempelkamp, D. Liu, and T. L. Kelly, "Investigation of $CH_3NH_3PbI_3$ degradation rates and mechanisms in controlled humidity environments using in situ techniques," *ACS Nano*, vol. 9, no. 2, pp. 1955–1963, 2015, pMID: 25635696. [Online]. Available: https://doi.org/10.1021/nn506864k

[9] S. N. Habisreutinger, T. Leijtens, G. E. Eperon, S. D. Stranks, R. J. Nicholas, and H. J. Snaith, "Carbon nanotube/polymer composites as a highly stable hole collection layer in perovskite solar cells," *Nano Letters*, vol. 14, no. 10, pp. 5561–5568, 2014, pMID: 25226226. [Online]. Available: https://doi.org/10.1021/nl501982b

[10] Z. Xiao, Y. Yuan, Y. Shao, Q. Wang, Q. Dong, C. Bi, P. Sharma, A. Gruverman, and J. Huang, "Giant switchable photovoltaic effect in organometal trihalide perovskite devices," *Nature Materials*, vol. 14, no. 2, pp. 193–198, Feb 2015. [Online]. Available: https://doi.org/10.1038/nmat4150

[11] T. Leijtens, G. E. Eperon, S. Pathak, A. Abate, M. M. Lee, and H. J. Snaith, "Overcoming ultraviolet light instability of sensitized TiO_2 with meso-superstructured organometal tri-halide perovskite solar cells," *Nature Communications*, vol. 4, no. 1, p. 2885, Dec 2013. [Online]. Available: https://doi.org/10.1038/ncomms3885

[12] S.-W. Lee, S. Kim, S. Bae, K. Cho, T. Chung, L. E. Mundt, S. Lee, S. Park, H. Park, M. C. Schubert, S. W. Glunz, Y. Ko, Y. Jun, Y. Kang, H.-S. Lee, and D. Kim, "Uv

degradation and recovery of perovskite solar cells," *Scientific Reports*, vol. 6, no. 1, p. 38150, Dec 2016. [Online]. Available: https://doi.org/10.1038/srep38150

[13] Y. Yan, Q. Wu, Y. Zhao, S. Chen, S. Hu, J. Zhu, J. Huang, and Z. Liang, "Air-stable and self-driven perovskite photodiodes with high on/off ratio and swift photoresponse," *Small*, vol. 14, no. 41, p. 1802764, 2018. [Online]. Available: https://onlinelibrary.wiley.com/doi/abs/10.1002/smll.201802764

[14] C. Bao, Z. Chen, Y. Fang, H. Wei, Y. Deng, X. Xiao, L. Li, and J. Huang, "Low-noise and large-linear-dynamic-range photodetectors based on hybrid-perovskite thin-single-crystals," *Advanced Materials*, vol. 29, no. 39, p. 1703209, 2017. [Online]. Available: https://onlinelibrary.wiley.com/doi/abs/10.1002/adma.201703209

[15] L. Zhang, X. Yang, Q. Jiang, P. Wang, Z. Yin, X. Zhang, H. Tan, Y. M. Yang, M. Wei, B. R. Sutherland, E. H. Sargent, and J. You, "Ultra-bright and highly efficient inorganic based perovskite light-emitting diodes," *Nature Communications*, vol. 8, no. 1, p. 15640, Jun 2017. [Online]. Available: https://doi.org/10.1038/ncomms15640

[16] J. Wang, N. Wang, Y. Jin, J. Si, Z.-K. Tan, H. Du, L. Cheng, X. Dai, S. Bai, H. He, Z. Ye, M. L. Lai, R. H. Friend, and W. Huang, "Interfacial control toward efficient and low-voltage perovskite light-emitting diodes," *Advanced Materials*, vol. 27, no. 14, pp. 2311–2316, 2015. [Online]. Available: https://onlinelibrary.wiley.com/doi/abs/10.1002/adma.201405217

[17] G. Grancini, C. Roldán-Carmona, I. Zimmermann, E. Mosconi, X. Lee, D. Martineau, S. Narbey, F. Oswald, F. De Angelis,

M. Graetzel, and M. K. Nazeeruddin, "One-year stable perovskite solar cells by 2D/3D interface engineering," *Nature Communications*, vol. 8, no. 1, p. 15684, Jun 2017. [Online]. Available: https://doi.org/10.1038/ncomms15684

[18] Y.-W. Jang, S. Lee, K. M. Yeom, K. Jeong, K. Choi, M. Choi, and J. H. Noh, "Intact 2D/3D halide junction perovskite solar cells via solid-phase in-plane growth," *Nature Energy*, vol. 6, no. 1, pp. 63–71, Jan 2021. [Online]. Available: https://doi.org/10.1038/s41560-020-00749-7

[19] I. C. Smith, E. T. Hoke, D. Solis-Ibarra, M. D. McGehee, and H. I. Karunadasa, "A layered hybrid perovskite solar-cell absorber with enhanced moisture stability," *Angewandte Chemie International Edition*, vol. 53, no. 42, pp. 11 232–11 235, 2014. [Online]. Available: https://onlinelibrary.wiley.com/doi/abs/10.1002/anie.201406466

[20] D. H. Cao, C. C. Stoumpos, O. K. Farha, J. T. Hupp, and M. G. Kanatzidis, "2D homologous perovskites as light-absorbing materials for solar cell applications," *Journal of the American Chemical Society*, vol. 137, no. 24, pp. 7843–7850, 2015, pMID: 26020457. [Online]. Available: https://doi.org/10.1021/jacs.5b03796

[21] H. Tsai, W. Nie, J.-C. Blancon, C. C. Stoumpos, R. Asadpour, B. Harutyunyan, A. J. Neukirch, R. Verduzco, J. J. Crochet, S. Tretiak, L. Pedesseau, J. Even, M. A. Alam, G. Gupta, J. Lou, P. M. Ajayan, M. J. Bedzyk, M. G. Kanatzidis, and A. D. Mohite, "High-efficiency two-dimensional Ruddlesden–Popper perovskite solar cells," *Nature*, vol. 536, no. 7616, pp. 312–316, Aug 2016. [Online]. Available: https://doi.org/10.1038/nature18306

[22] T. Ishihara, X. Hong, J. Ding, and A. Nurmikko, "Dielectric confinement effect for exciton and biexciton states in *PbI*$_4$-based two-dimensional semiconductor structures," *Surface Science*, vol. 267, no. 1, pp. 323 – 326, 1992. [Online]. Available: http://www.sciencedirect.com/science/article/pii/0039602892911474

[23] T. Ishihara, "Optical properties of PbI-based perovskite structures," *Journal of Luminescence*, vol. 60-61, pp. 269–274, 1994. [Online]. Available: https://www.sciencedirect.com/science/article/pii/0022231394901457

[24] L. Lei, D. Seyitliyev, S. Stuard, J. Mendes, Q. Dong, X. Fu, Y.-A. Chen, S. He, X. Yi, L. Zhu, C.-H. Chang, H. Ade, K. Gundogdu, and F. So, "Efficient energy funneling in quasi-2D perovskites: From light emission to lasing," *Advanced Materials*, vol. 32, no. 16, p. 1906571, 2020. [Online]. Available: https://onlinelibrary.wiley.com/doi/abs/10.1002/adma.201906571

[25] J. Xing, Y. Zhao, M. Askerka, L. N. Quan, X. Gong, W. Zhao, J. Zhao, H. Tan, G. Long, L. Gao, Z. Yang, O. Voznyy, J. Tang, Z.-H. Lu, Q. Xiong, and E. H. Sargent, "Color-stable highly luminescent sky-blue perovskite light-emitting diodes," *Nature Communications*, vol. 9, no. 1, p. 3541, 2018. [Online]. Available: https://doi.org/10.1038/s41467-018-05909-8

[26] L. Kong, X. Zhang, Y. Li, H. Wang, Y. Jiang, S. Wang, M. You, C. Zhang, T. Zhang, S. V. Kershaw, W. Zheng, Y. Yang, Q. Lin, M. Yuan, A. L. Rogach, and X. Yang, "Smoothing the energy transfer pathway in quasi-2D perovskite films using methanesulfonate leads to highly efficient light-emitting devices," *Nature Communications*, vol. 12, no. 1, p. 1246, Feb 2021. [Online]. Available: https://doi.org/10.1038/s41467-021-21522-8

[27] M. D. Smith and H. I. Karunadasa, "White-light emission from layered halide perovskites," *Accounts of Chemical Research*, vol. 51, no. 3, pp. 619–627, 2018, pMID: 29461806. [Online]. Available: https://doi.org/10.1021/acs.accounts.7b00433

[28] Y. Liu, J. Cui, K. Du, H. Tian, Z. He, Q. Zhou, Z. Yang, Y. Deng, D. Chen, X. Zuo, Y. Ren, L. Wang, H. Zhu, B. Zhao, D. Di, J. Wang, R. H. Friend, and Y. Jin, "Efficient blue light-emitting diodes based on quantum-confined bromide perovskite nanostructures," *Nature Photonics*, vol. 13, no. 11, pp. 760–764, Nov 2019. [Online]. Available: https://doi.org/10.1038/s41566-019-0505-4

[29] X. Yang, X. Zhang, J. Deng, Z. Chu, Q. Jiang, J. Meng, P. Wang, L. Zhang, Z. Yin, and J. You, "Efficient green light-emitting diodes based on quasi-two-dimensional composition and phase engineered perovskite with surface passivation," *Nature Communications*, vol. 9, no. 1, p. 570, Feb 2018. [Online]. Available: https://doi.org/10.1038/s41467-018-02978-7

[30] D. Zhang, Y. Fu, H. Zhan, C. Zhao, X. Gao, C. Qin, and L. Wang, "Suppressing thermal quenching via defect passivation for efficient quasi-2D perovskite light-emitting diodes," *Light: Science & Applications*, vol. 11, no. 1, p. 69, Mar 2022. [Online]. Available: https://doi.org/10.1038/s41377-022-00761-4

[31] C. Qin, A. S. D. Sandanayaka, C. Zhao, T. Matsushima, D. Zhang, T. Fujihara, and C. Adachi, "Stable room-temperature continuous-wave lasing in quasi-2D perovskite films," *Nature*, vol. 585, no. 7823, pp. 53–57, Sep 2020. [Online]. Available: https://doi.org/10.1038/s41586-020-2621-1

[32] J. Byun, H. Cho, C. Wolf, M. Jang, A. Sadhanala, R. H. Friend, H. Yang, and T.-W. Lee, "Efficient visible quasi-2D perovskite light-emitting diodes," *Advanced Materials*, vol. 28, no. 34, pp. 7515–7520, 2016. [Online]. Available: https: //onlinelibrary.wiley.com/doi/abs/10.1002/adma.201601369

[33] Z. Ren, J. Yu, Z. Qin, J. Wang, J. Sun, C. C. S. Chan, S. Ding, K. Wang, R. Chen, K. S. Wong, X. Lu, W.-J. Yin, and W. C. H. Choy, "High-performance blue perovskite light-emitting diodes enabled by efficient energy transfer between coupled quasi-2D perovskite layers," *Advanced Materials*, vol. 33, no. 1, p. 2005570, 2021. [Online]. Available: https: //onlinelibrary.wiley.com/doi/abs/10.1002/adma.202005570

[34] Y. Jiang, J. Wei, and M. Yuan, "Energy-funneling process in quasi-2D perovskite light-emitting diodes," *The Journal of Physical Chemistry Letters*, vol. 12, no. 10, pp. 2593–2606, 2021, pMID: 33689359. [Online]. Available: https: //doi.org/10.1021/acs.jpclett.1c00072

[35] M. Yuan, L. N. Quan, R. Comin, G. Walters, R. Sabatini, O. Voznyy, S. Hoogland, Y. Zhao, E. M. Beauregard, P. Kanjanaboos, Z. Lu, D. H. Kim, and E. H. Sargent, "Perovskite energy funnels for efficient light-emitting diodes," *Nature Nanotechnology*, vol. 11, no. 10, pp. 872–877, Oct 2016. [Online]. Available: https://doi.org/10.1038/nnano.2016.110

[36] W. Bi, Q. Cui, P. Jia, X. Huang, Y. Zhong, D. Wu, Y. Tang, S. Shen, Y. Hu, Z. Lou, F. Teng, X. Liu, and Y. Hou, "Efficient quasi-two-dimensional perovskite light-emitting diodes with improved multiple quantum well structure," *ACS Applied Materials & Interfaces*, vol. 12, no. 1, pp.

1721–1727, 2020, pMID: 31880424. [Online]. Available: https://doi.org/10.1021/acsami.9b10186

[37] L. Cheng, T. Jiang, Y. Cao, C. Yi, N. Wang, W. Huang, and J. Wang, "Multiple-quantum-well perovskites for high-performance light-emitting diodes," *Advanced Materials*, vol. 32, no. 15, p. 1904163, 2020. [Online]. Available: https://onlinelibrary.wiley.com/doi/abs/10.1002/adma.201904163

[38] Y. Han, S. Park, C. Kim, M. Lee, and I. Hwang, "Phase control of quasi-2D perovskites and improved light-emitting performance by excess organic cations and nanoparticle intercalation," *Nanoscale*, vol. 11, pp. 3546–3556, 2019. [Online]. Available: http://dx.doi.org/10.1039/C8NR07361A

[39] N. Wang, L. Cheng, R. Ge, S. Zhang, Y. Miao, W. Zou, C. Yi, Y. Sun, Y. Cao, R. Yang, Y. Wei, Q. Guo, Y. Ke, M. Yu, Y. Jin, Y. Liu, Q. Ding, D. Di, L. Yang, G. Xing, H. Tian, C. Jin, F. Gao, R. H. Friend, J. Wang, and W. Huang, "Perovskite light-emitting diodes based on solution-processed self-organized multiple quantum wells," *Nature Photonics*, vol. 10, no. 11, pp. 699–704, Nov 2016. [Online]. Available: https://doi.org/10.1038/nphoton.2016.185

[40] B. Zhao, S. Bai, V. Kim, R. Lamboll, R. Shivanna, F. Auras, J. M. Richter, L. Yang, L. Dai, M. Alsari, X.-J. She, L. Liang, J. Zhang, S. Lilliu, P. Gao, H. J. Snaith, J. Wang, N. C. Greenham, R. H. Friend, and D. Di, "High-efficiency perovskite–polymer bulk heterostructure light-emitting diodes," *Nature Photonics*, vol. 12, no. 12, pp. 783–789, Dec 2018. [Online]. Available: https://doi.org/10.1038/s41566-018-0283-4

[41] M. Ban, Y. Zou, J. P. H. Rivett, Y. Yang, T. H. Thomas, Y. Tan, T. Song, X. Gao, D. Credgington, F. Deschler, H. Sirringhaus, and B. Sun, "Solution-processed perovskite light emitting diodes with efficiency exceeding 15% through additive-controlled nanostructure tailoring," *Nature Communications*, vol. 9, no. 1, p. 3892, Sep 2018. [Online]. Available: https://doi.org/10.1038/s41467-018-06425-5

[42] Y. Miao, L. Cheng, W. Zou, L. Gu, J. Zhang, Q. Guo, Q. Peng, M. Xu, Y. He, S. Zhang, Y. Cao, R. Li, N. Wang, W. Huang, and J. Wang, "Microcavity top-emission perovskite light-emitting diodes," *Light: Science & Applications*, vol. 9, no. 1, p. 89, May 2020. [Online]. Available: https://doi.org/10.1038/s41377-020-0328-6

[43] A. Kiligaridis, P. A. Frantsuzov, A. Yangui, S. Seth, J. Li, Q. An, Y. Vaynzof, and I. G. Scheblykin, "Are Shockley-Read-Hall and ABC models valid for lead halide perovskites?" *Nature Communications*, vol. 12, no. 1, p. 3329, Jun 2021. [Online]. Available: https://doi.org/10.1038/s41467-021-23275-w

[44] S. D. Stranks, V. M. Burlakov, T. Leijtens, J. M. Ball, A. Goriely, and H. J. Snaith, "Recombination kinetics in organic-inorganic perovskites: Excitons, free charge, and subgap states," *Phys. Rev. Applied*, vol. 2, p. 034007, Sep 2014. [Online]. Available: https://link.aps.org/doi/10.1103/PhysRevApplied.2.034007

[45] V. D'Innocenzo, G. Grancini, M. J. P. Alcocer, A. R. S. Kandada, S. D. Stranks, M. M. Lee, G. Lanzani, H. J. Snaith, and A. Petrozza, "Excitons versus free charges in organo-lead tri-halide perovskites," *Nature Communications*, vol. 5, no. 1, p. 3586, Apr 2014. [Online]. Available: https://doi.org/10.1038/ncomms4586

[46] N. Spitha, D. D. Kohler, M. P. Hautzinger, J. Li, S. Jin, and J. C. Wright, "Discerning between exciton and free-carrier behaviors in Ruddlesden–Popper perovskite quantum wells through kinetic modeling of photoluminescence dynamics," *The Journal of Physical Chemistry C*, vol. 124, no. 31, pp. 17 430–17 439, 2020. [Online]. Available: https://doi.org/10.1021/acs.jpcc.0c06345

[47] Y. Li, I. Allegro, M. Kaiser, A. J. Malla, B. S. Richards, U. Lemmer, U. W. Paetzold, and I. A. Howard, "Exciton versus free carrier emission: Implications for photoluminescence efficiency and amplified spontaneous emission thresholds in quasi-2D and 3D perovskites," *Materials Today*, vol. 49, pp. 35–47, 2021. [Online]. Available: https://www.sciencedirect.com/science/article/pii/S1369702121001619

[48] T. R. Hopper, A. Gorodetsky, A. Jeong, F. Krieg, M. I. Bodnarchuk, M. Maimaris, M. Chaplain, T. J. Macdonald, X. Huang, R. Lovrincic, M. V. Kovalenko, and A. A. Bakulin, "Hot carrier dynamics in perovskite nanocrystal solids: Role of the cold carriers, nanoconfinement, and the surface," *Nano Letters*, vol. 20, no. 4, pp. 2271–2278, 2020, pMID: 32142303. [Online]. Available: https://doi.org/10.1021/acs.nanolett.9b04491

[49] X. Hong, T. Ishihara, and A. V. Nurmikko, "Dielectric confinement effect on excitons in PbI_4-based layered semiconductors," *Phys. Rev. B*, vol. 45, pp. 6961–6964, Mar 1992. [Online]. Available: https://link.aps.org/doi/10.1103/PhysRevB.45.6961

[50] J.-C. Blancon, A. V. Stier, H. Tsai, W. Nie, C. C. Stoumpos, B. Traoré, L. Pedesseau, M. Kepenekian, F. Katsutani, G. T. Noe, J. Kono, S. Tretiak, S. A. Crooker, C. Katan, M. G. Kanatzidis, J. J. Crochet, J. Even, and A. D. Mohite, "Scaling

law for excitons in 2D perovskite quantum wells," *Nature Communications*, vol. 9, no. 1, p. 2254, Jun 2018. [Online]. Available: https://doi.org/10.1038/s41467-018-04659-x

[51] M. Shimizu, J.-I. Fujisawa, and J. Ishi-Hayase, "Influence of dielectric confinement on excitonic nonlinearity in inorganic-organic layered semiconductors," *Phys. Rev. B*, vol. 71, p. 205306, May 2005. [Online]. Available: https://link.aps.org/doi/10.1103/PhysRevB.71.205306

[52] J.-i. Fujisawa and T. Ishihara, "Excitons and biexcitons bound to a positive ion in a bismuth-doped inorganic-organic layered lead iodide semiconductor," *Phys. Rev. B*, vol. 70, p. 205330, Nov 2004. [Online]. Available: https://link.aps.org/doi/10.1103/PhysRevB.70.205330

[53] F. Thouin, S. Neutzner, D. Cortecchia, V. A. Dragomir, C. Soci, T. Salim, Y. M. Lam, R. Leonelli, A. Petrozza, A. R. S. Kandada, and C. Silva, "Stable biexcitons in two-dimensional metal-halide perovskites with strong dynamic lattice disorder," *Phys. Rev. Materials*, vol. 2, p. 034001, 03 2018. [Online]. Available: https://link.aps.org/doi/10.1103/PhysRevMaterials.2.034001

[54] M. Shimizu, J.-I. Fujisawa, and T. Ishihara, "Photoluminescence of the inorganic-organic layered semiconductor $(C_6H_5C_2H_4NH_3)_2PbI_4$: Observation of triexciton formation," *Physical Review B - PHYS REV B*, vol. 74, 10 2006.

[55] M. N. Saha and A. Fowler, "On a physical theory of stellar spectra," *Proceedings of the Royal Society of London. Series A, Containing Papers of a Mathematical and Physical Character*, vol. 99, no. 697, pp. 135–153, 1921. [Online]. Available: https://royalsocietypublishing.org/doi/abs/10.1098/rspa.1921.0029

[56] R. Cingolani, L. Calcagnile, G. Colí, R. Rinaldi, M. Lomoscolo, M. DiDio, A. Franciosi, L. Vanzetti, G. C. LaRocca, and D. Campi, "Radiative recombination processes in wide-band-gap II–VI quantum wells: the interplay between excitons and free carriers," *J. Opt. Soc. Am. B*, vol. 13, no. 6, pp. 1268–1277, Jun 1996. [Online]. Available: http://www.osapublishing.org/josab/abstract.cfm?URI=josab-13-6-1268

[57] D. Chen and X. Chen, "Luminescent perovskite quantum dots: synthesis, microstructures, optical properties and applications," *J. Mater. Chem. C*, vol. 7, pp. 1413–1446, 2019. [Online]. Available: http://dx.doi.org/10.1039/C8TC05545A

[58] Z. Xiao and Y. Yan, "Progress in theoretical study of metal halide perovskite solar cell materials," *Advanced Energy Materials*, vol. 7, no. 22, p. 1701136, 2017. [Online]. Available: https://onlinelibrary.wiley.com/doi/abs/10.1002/aenm.201701136

[59] Y. Li, R. L. Z. Hoye, H.-H. Gao, L. Yan, X. Zhang, Y. Zhou, J. L. MacManus-Driscoll, and J. Gan, "Over 20% efficiency in methylammonium lead iodide perovskite solar cells with enhanced stability via "in situ solidification" of the TiO_2 compact layer," *ACS Applied Materials & Interfaces*, vol. 12, no. 6, pp. 7135–7143, 2020, pMID: 31961122. [Online]. Available: https://doi.org/10.1021/acsami.9b19153

[60] L. A. Frolova, A. I. Davlethanov, N. N. Dremova, I. Zhidkov, A. F. Akbulatov, E. Z. Kurmaev, S. M. Aldoshin, K. J. Stevenson, and P. A. Troshin, "Efficient and stable $MAPbI_3$-based perovskite solar cells using polyvinylcarbazole passivation," *The Journal of Physical Chemistry Letters*, vol. 11, no. 16, pp. 6772–6778, 2020, pMID: 32689804. [Online]. Available: https://doi.org/10.1021/acs.jpclett.0c01776

[61] E. Akman, A. E. Shalan, F. Sadegh, and S. Akin, "Moisture-resistant FAPbI$_3$ perovskite solar cell with 22.25 % power conversion efficiency through pentafluorobenzyl phosphonic acid passivation," *ChemSusChem*, vol. 14, no. 4, pp. 1176–1183, 2021. [Online]. Available: https://chemistry-europe.onlinelibrary.wiley.com/doi/abs/10.1002/cssc.202002707

[62] J. Jeong, M. Kim, J. Seo, H. Lu, P. Ahlawat, A. Mishra, Y. Yang, M. A. Hope, F. T. Eickemeyer, M. Kim, Y. J. Yoon, I. W. Choi, B. P. Darwich, S. J. Choi, Y. Jo, J. H. Lee, B. Walker, S. M. Zakeeruddin, L. Emsley, U. Rothlisberger, A. Hagfeldt, D. S. Kim, M. Grätzel, and J. Y. Kim, "Pseudo-halide anion engineering for α-FAPbI$_3$ perovskite solar cells," *Nature*, vol. 592, no. 7854, pp. 381–385, Apr 2021. [Online]. Available: https://doi.org/10.1038/s41586-021-03406-5

[63] C. Li, Z. Song, C. Chen, C. Xiao, B. Subedi, S. P. Harvey, N. Shrestha, K. K. Subedi, L. Chen, D. Liu, Y. Li, Y.-W. Kim, C.-s. Jiang, M. J. Heben, D. Zhao, R. J. Ellingson, N. J. Podraza, M. Al-Jassim, and Y. Yan, "Low-bandgap mixed tin–lead iodide perovskites with reduced methylammonium for simultaneous enhancement of solar cell efficiency and stability," *Nature Energy*, vol. 5, no. 10, pp. 768–776, Oct 2020. [Online]. Available: https://doi.org/10.1038/s41560-020-00692-7

[64] D. Zhang, J. Yuan, and J. Tian, "All-inorganic perovskite solar cells with efficiency >20%," *Science China Materials*, vol. 64, no. 10, pp. 2624–2626, Oct 2021. [Online]. Available: https://doi.org/10.1007/s40843-021-1726-9

[65] Y. H. Chang, C. H. Park, and K. Matsuishi, "First-principles study of the structural and the electronic properties of the lead-halide-based inorganic-organic perovskites (CH$_3$NH$_3$)PbX$_3$ and

CsPbX$_3$ (X = Cl, Br, I)," *Journal of the Korean Physical Society*, vol. 44, pp. 889–893, 2004.

[66] R. Prasanna, A. Gold-Parker, T. Leijtens, B. Conings, A. Babayigit, H.-G. Boyen, M. F. Toney, and M. D. McGehee, "Band gap tuning via lattice contraction and octahedral tilting in perovskite materials for photovoltaics," *Journal of the American Chemical Society*, vol. 139, no. 32, pp. 11 117–11 124, 2017, pMID: 28704048. [Online]. Available: https://doi.org/10.1021/jacs.7b04981

[67] S. De Wolf, J. Holovsky, S.-J. Moon, P. Löper, B. Niesen, M. Ledinsky, F.-J. Haug, J.-H. Yum, and C. Ballif, "Organometallic halide perovskites: Sharp optical absorption edge and its relation to photovoltaic performance," *The Journal of Physical Chemistry Letters*, vol. 5, no. 6, pp. 1035–1039, 2014, pMID: 26270984. [Online]. Available: https://doi.org/10.1021/jz500279b

[68] S. D. Stranks, G. E. Eperon, G. Grancini, C. Menelaou, M. J. P. Alcocer, T. Leijtens, L. M. Herz, A. Petrozza, and H. J. Snaith, "Electron-hole diffusion lengths exceeding 1 micrometer in an organometal trihalide perovskite absorber," *Science*, vol. 342, no. 6156, pp. 341–344, 2013. [Online]. Available: https://www.science.org/doi/abs/10.1126/science.1243982

[69] C. Wehrenfennig, G. E. Eperon, M. B. Johnston, H. J. Snaith, and L. M. Herz, "High charge carrier mobilities and lifetimes in organolead trihalide perovskites," *Advanced Materials*, vol. 26, no. 10, pp. 1584–1589, 2014. [Online]. Available: https://onlinelibrary.wiley.com/doi/abs/10.1002/adma.201305172

[70] N. L. Chang, A. W. Y. Ho-Baillie, D. Vak, M. Gao, M. A. Green, and R. J. Egan, "Manufacturing cost and market potential analysis of demonstrated roll-to-roll perovskite photovoltaic cell processes," *Solar Energy Materials and Solar Cells*, vol. 174, pp. 314–324, 2018. [Online]. Available: https://www.sciencedirect.com/science/article/pii/S0927024817304865

[71] A. M. A. Leguy, Y. Hu, M. Campoy-Quiles, M. I. Alonso, O. J. Weber, P. Azarhoosh, M. van Schilfgaarde, M. T. Weller, T. Bein, J. Nelson, P. Docampo, and P. R. F. Barnes, "Reversible hydration of $CH_3NH_3PbI_3$ in films, single crystals, and solar cells," *Chemistry of Materials*, vol. 27, no. 9, pp. 3397–3407, 2015. [Online]. Available: https://doi.org/10.1021/acs.chemmater.5b00660

[72] A. M. Askar, G. M. Bernard, B. Wiltshire, K. Shankar, and V. K. Michaelis, "Multinuclear magnetic resonance tracking of hydro, thermal, and hydrothermal decomposition of $CH_3NH_3PbI_3$," *The Journal of Physical Chemistry C*, vol. 121, no. 2, pp. 1013–1024, 2017. [Online]. Available: https://doi.org/10.1021/acs.jpcc.6b10865

[73] J. A. Christians, P. A. Miranda Herrera, and P. V. Kamat, "Transformation of the excited state and photovoltaic efficiency of $CH_3NH_3PbI_3$ perovskite upon controlled exposure to humidified air," *Journal of the American Chemical Society*, vol. 137, no. 4, pp. 1530–1538, 2015, pMID: 25590693. [Online]. Available: https://doi.org/10.1021/ja511132a

[74] X. Ding, M. Cai, X. Liu, Y. Ding, X. Liu, Y. Wu, T. Hayat, A. Alsaedi, and S. Dai, "Enhancing the phase stability of inorganic α-CsPbI$_3$ by the bication-conjugated organic molecule for efficient perovskite solar cells," *ACS*

Applied Materials & Interfaces, vol. 11, no. 41, pp. 37 720–37 725, 2019, pMID: 31588720. [Online]. Available: https://doi.org/10.1021/acsami.9b12579

[75] N. Aristidou, I. Sanchez-Molina, T. Chotchuangchutchaval, M. Brown, L. Martinez, T. Rath, and S. A. Haque, "The role of oxygen in the degradation of methylammonium lead trihalide perovskite photoactive layers," *Angewandte Chemie International Edition*, vol. 54, no. 28, pp. 8208–8212, 2015. [Online]. Available: https://onlinelibrary.wiley.com/doi/abs/10.1002/anie.201503153

[76] A. Hinsch, J. M. Kroon, R. Kern, I. Uhlendorf, J. Holzbock, A. Meyer, and J. Ferber, "Long-term stability of dye-sensitised solar cells," *Progress in Photovoltaics: Research and Applications*, vol. 9, no. 6, pp. 425–438, 2001. [Online]. Available: https://onlinelibrary.wiley.com/doi/abs/10.1002/pip.397

[77] T. Supasai, N. Rujisamphan, K. Ullrich, A. Chemseddine, and T. Dittrich, "Formation of a passivating $CH_3NH_3PbI_3/PbI_2$ interface during moderate heating of $CH_3NH_3PbI_3$ layers," *Applied Physics Letters*, vol. 103, no. 18, p. 183906, 2013. [Online]. Available: https://doi.org/10.1063/1.4826116

[78] H.-S. Kim, J.-Y. Seo, and N.-G. Park, "Material and device stability in perovskite solar cells," *ChemSusChem*, vol. 9, no. 18, pp. 2528–2540, 2016. [Online]. Available: https://chemistry-europe.onlinelibrary.wiley.com/doi/abs/10.1002/cssc.201600915

[79] T. M. Koh, V. Shanmugam, J. Schlipf, L. Oesinghaus, P. Müller-Buschbaum, N. Ramakrishnan, V. Swamy, N. Mathews,

P. P. Boix, and S. G. Mhaisalkar, "Nanostructuring mixed-dimensional perovskites: A route toward tunable, efficient photovoltaics," *Advanced Materials*, vol. 28, no. 19, pp. 3653–3661, 2016. [Online]. Available: https://onlinelibrary.wiley.com/doi/abs/10.1002/adma.201506141

[80] H. Zheng, G. Liu, L. Zhu, J. Ye, X. Zhang, A. Alsaedi, T. Hayat, X. Pan, and S. Dai, "The effect of hydrophobicity of ammonium salts on stability of quasi-2D perovskite materials in moist condition," *Advanced Energy Materials*, vol. 8, no. 21, p. 1800051, 2018. [Online]. Available: https://onlinelibrary.wiley.com/doi/abs/10.1002/aenm.201800051

[81] L. Li, J. Kim, C. Jin, G. J. Ye, D. Y. Qiu, F. H. da Jornada, Z. Shi, L. Chen, Z. Zhang, F. Yang, K. Watanabe, T. Taniguchi, W. Ren, S. G. Louie, X. H. Chen, Y. Zhang, and F. Wang, "Direct observation of the layer-dependent electronic structure in phosphorene," *Nature Nanotechnology*, vol. 12, no. 1, pp. 21–25, Jan 2017. [Online]. Available: https://doi.org/10.1038/nnano.2016.171

[82] L. V. Keldysh, "Coulomb interaction in thin semiconductor and semimetal films," *Soviet Journal of Experimental and Theoretical Physics Letters*, vol. 29, p. 658, Jun. 1979.

[83] L. Pedesseau, D. Sapori, B. Traore, R. Robles, H.-H. Fang, M. A. Loi, H. Tsai, W. Nie, J.-C. Blancon, A. Neukirch, S. Tretiak, A. D. Mohite, C. Katan, J. Even, and M. Kepenekian, "Advances and promises of layered halide hybrid perovskite semiconductors," *ACS Nano*, vol. 10, no. 11, pp. 9776–9786, 2016, pMID: 27775343. [Online]. Available: https://doi.org/10.1021/acsnano.6b05944

[84] C. Katan, N. Mercier, and J. Even, "Quantum and dielectric confinement effects in lower-dimensional hybrid perovskite semiconductors," *Chemical Reviews*, vol. 119, no. 5, pp. 3140–3192, 2019, pMID: 30638375. [Online]. Available: https://doi.org/10.1021/acs.chemrev.8b00417

[85] C. L. Davies, M. R. Filip, J. B. Patel, T. W. Crothers, C. Verdi, A. D. Wright, R. L. Milot, F. Giustino, M. B. Johnston, and L. M. Herz, "Bimolecular recombination in methylammonium lead triiodide perovskite is an inverse absorption process," *Nature Communications*, vol. 9, no. 1, p. 293, Jan 2018. [Online]. Available: https://doi.org/10.1038/s41467-017-02670-2

[86] D. Ghosh, D. Acharya, L. Pedesseau, C. Katan, J. Even, S. Tretiak, and A. J. Neukirch, "Charge carrier dynamics in two-dimensional hybrid perovskites: Dion–jacobson vs. Ruddlesden–Popper phases," *J. Mater. Chem. A*, vol. 8, pp. 22 009–22 022, 2020. [Online]. Available: http://dx.doi.org/10.1039/D0TA07205B

[87] E. S. Vasileiadou, B. Wang, I. Spanopoulos, I. Hadar, A. Navrotsky, and M. G. Kanatzidis, "Insight on the stability of thick layers in 2D Ruddlesden–Popper and Dion–Jacobson lead iodide perovskites," *Journal of the American Chemical Society*, vol. 143, no. 6, pp. 2523–2536, 2021, pMID: 33534580. [Online]. Available: https://doi.org/10.1021/jacs.0c11328

[88] X. Chen, H. Lu, Y. Yang, and M. C. Beard, "Excitonic effects in methylammonium lead halide perovskites," *The Journal of Physical Chemistry Letters*, vol. 9, no. 10, pp. 2595–2603, 2018, pMID: 29714488. [Online]. Available: https://doi.org/10.1021/acs.jpclett.8b00526

[89] J. V. Milić, J.-H. Im, D. J. Kubicki, A. Ummadisingu, J.-Y. Seo, Y. Li, M. A. Ruiz-Preciado, M. I. Dar, S. M. Zakeeruddin, L. Emsley, and M. Grätzel, "Supramolecular engineering for formamidinium-based layered 2D perovskite solar cells: Structural complexity and dynamics revealed by solid-state nmr spectroscopy," *Advanced Energy Materials*, vol. 9, no. 20, p. 1900284, 2019. [Online]. Available: https://onlinelibrary.wiley.com/doi/abs/10.1002/aenm.201900284

[90] Y. Li, J. V. Milić, A. Ummadisingu, J.-Y. Seo, J.-H. Im, H.-S. Kim, Y. Liu, M. I. Dar, S. M. Zakeeruddin, P. Wang, A. Hagfeldt, and M. Grätzel, "Bifunctional organic spacers for formamidinium-based hybrid Dion–Jacobson two-dimensional perovskite solar cells," *Nano Letters*, vol. 19, no. 1, pp. 150–157, 2019. [Online]. Available: https://doi.org/10.1021/acs.nanolett.8b03552

[91] T. Malevu, B. Mwankemwa, K. Tshabalala, and R. Ocaya, "Effect of annealing on the efficiency of ambient-atmosphere fabricated MAPbI$_3$ perovskite solar cells," *Scientific African*, vol. 8, p. e00447, 2020. [Online]. Available: https://www.sciencedirect.com/science/article/pii/S246822762030185X

[92] M. Kaiser, Y. Li, J. Schwenzer, M. Jakoby, I. Allegro, M. Gerhard, M. Koch, A. Ducinskas, B. S. Richards, M. Graetzel, J. V. Milić, U. W. Paetzold, and I. A. Howard, "How free exciton–exciton annihilation lets bound exciton emission dominate the photoluminescence of 2D-perovskites under high-fluence pulsed excitation at cryogenic temperatures," *Journal of Applied Physics*, vol. 129, no. 12, p. 123101, 2021. [Online]. Available: https://doi.org/10.1063/5.0037800

[93] F. Zhang, H. Lu, J. Tong, J. J. Berry, M. C. Beard, and

K. Zhu, "Advances in two-dimensional organic–inorganic hybrid perovskites," *Energy Environ. Sci.*, vol. 13, pp. 1154–1186, 2020. [Online]. Available: http://dx.doi.org/10.1039/C9EE03757H

[94] Y. Zhai, S. Baniya, C. Zhang, J. Li, P. Haney, C.-X. Sheng, E. Ehrenfreund, and Z. V. Vardeny, "Giant rashba splitting in 2D organic-inorganic halide perovskites measured by transient spectroscopies," *Science Advances*, vol. 3, no. 7, 2017. [Online]. Available: https://advances.sciencemag.org/content/3/7/e1700704

[95] J. Yin, P. Maity, L. Xu, A. M. El-Zohry, H. Li, O. M. Bakr, J.-L. Brédas, and O. F. Mohammed, "Layer-dependent rashba band splitting in 2D hybrid perovskites," *Chemistry of Materials*, vol. 30, no. 23, pp. 8538–8545, 12 2018. [Online]. Available: https://doi.org/10.1021/acs.chemmater.8b03436

[96] D. Giovanni, W. K. Chong, H. A. Dewi, K. Thirumal, I. Neogi, R. Ramesh, S. Mhaisalkar, N. Mathews, and T. C. Sum, "Tunable room-temperature spin-selective optical stark effect in solution-processed layered halide perovskites," *Science Advances*, vol. 2, no. 6, 2016. [Online]. Available: https://advances.sciencemag.org/content/2/6/e1600477

[97] J. Even, L. Pedesseau, M.-A. Dupertuis, J.-M. Jancu, and C. Katan, "Electronic model for self-assembled hybrid organic/perovskite semiconductors: Reverse band edge electronic states ordering and spin-orbit coupling," *Phys. Rev. B*, vol. 86, p. 205301, 11 2012. [Online]. Available: https://link.aps.org/doi/10.1103/PhysRevB.86.205301

[98] D. Giovanni, W. K. Chong, Y. Y. F. Liu, H. A. Dewi, T. Yin, Y. Lekina, Z. X. Shen, N. Mathews, C. K. Gan, and T. C.

Sum, "Coherent spin and quasiparticle dynamics in solution-processed layered 2D lead halide perovskites," *Advanced Science*, vol. 5, no. 10, p. 1800664, 2018. [Online]. Available: https://onlinelibrary.wiley.com/doi/abs/10.1002/advs.201800664

[99] J. Yu, J. Kong, W. Hao, X. Guo, H. He, W. R. Leow, Z. Liu, P. Cai, G. Qian, S. Li, X. Chen, and X. Chen, "Broadband extrinsic self-trapped exciton emission in Sn-doped 2D lead-halide perovskites," *Advanced Materials*, vol. 31, no. 7, p. 1806385, 2019. [Online]. Available: https://onlinelibrary.wiley.com/doi/abs/10.1002/adma.201806385

[100] S. Li, J. Luo, J. Liu, and J. Tang, "Self-trapped excitons in all-inorganic halide perovskites: Fundamentals, status, and potential applications," *The Journal of Physical Chemistry Letters*, vol. 10, no. 8, pp. 1999–2007, 04 2019. [Online]. Available: https://doi.org/10.1021/acs.jpclett.8b03604

[101] Z.-G. Yu, "Optical deformation potential and self-trapped excitons in 2D hybrid perovskites," *Phys. Chem. Chem. Phys.*, vol. 21, pp. 22 293–22 301, 2019. [Online]. Available: http://dx.doi.org/10.1039/C9CP03080H

[102] D. Cortecchia, J. Yin, A. Bruno, S.-Z. A. Lo, G. G. Gurzadyan, S. Mhaisalkar, J.-L. Brédas, and C. Soci, "Polaron self-localization in white-light emitting hybrid perovskites," *J. Mater. Chem. C*, vol. 5, pp. 2771–2780, 2017. [Online]. Available: http://dx.doi.org/10.1039/C7TC00366H

[103] J. Yin, H. Li, D. Cortecchia, C. Soci, and J.-L. Brédas, "Excitonic and polaronic properties of 2D hybrid organic–inorganic perovskites," *ACS Energy Letters*, vol. 2, no. 2, pp. 417–423,

2017. [Online]. Available: https://doi.org/10.1021/acsenergylett. 6b00659

[104] J. Li, J. Ma, X. Cheng, Z. Liu, Y. Chen, and D. Li, "Anisotropy of excitons in two-dimensional perovskite crystals," *ACS Nano*, vol. 14, no. 2, pp. 2156–2161, 2020, pMID: 31968166. [Online]. Available: https://doi.org/10.1021/acsnano.9b08975

[105] K. Thirumal, W. K. Chong, W. Xie, R. Ganguly, S. K. Muduli, M. Sherburne, M. Asta, S. Mhaisalkar, T. C. Sum, H. S. Soo, and N. Mathews, "Morphology-independent stable white-light emission from self-assembled two-dimensional perovskites driven by strong exciton–phonon coupling to the organic framework," *Chemistry of Materials*, vol. 29, no. 9, pp. 3947–3953, 2017. [Online]. Available: https://doi.org/10.1021/acs.chemmater.7b00073

[106] J.-C. Blancon, H. Tsai, W. Nie, C. C. Stoumpos, L. Pedesseau, C. Katan, M. Kepenekian, C. M. M. Soe, K. Appavoo, M. Y. Sfeir, S. Tretiak, P. M. Ajayan, M. G. Kanatzidis, J. Even, J. J. Crochet, and A. D. Mohite, "Extremely efficient internal exciton dissociation through edge states in layered 2D perovskites," *Science*, vol. 355, no. 6331, pp. 1288–1292, 2017. [Online]. Available: https://science.sciencemag.org/content/355/6331/1288

[107] K. Wang, C. Wu, Y. Jiang, D. Yang, K. Wang, and S. Priya, "Distinct conducting layer edge states in two-dimensional (2D) halide perovskite," *Science Advances*, vol. 5, no. 7, 2019. [Online]. Available: https://advances.sciencemag.org/content/5/7/eaau3241

[108] Z. Zhang, W.-H. Fang, R. Long, and O. V. Prezhdo, "Exciton dissociation and suppressed charge recombination at 2D perovskite edges: Key roles of unsaturated halide bonds and thermal disorder," *Journal of the American Chemical Society*, vol. 141, no. 39, pp. 15 557–15 566, 2019, pMID: 31525977. [Online]. Available: https://doi.org/10.1021/jacs.9b06046

[109] G. Delport, G. Chehade, F. Lédée, H. Diab, C. Milesi-Brault, G. Trippé-Allard, J. Even, J.-S. Lauret, E. Deleporte, and D. Garrot, "Exciton–exciton annihilation in two-dimensional halide perovskites at room temperature," *The Journal of Physical Chemistry Letters*, vol. 10, no. 17, pp. 5153–5159, Sep 2019. [Online]. Available: https://doi.org/10.1021/acs.jpclett.9b01595

[110] K. Gauthron, J.-S. Lauret, L. Doyennette, G. Lanty, A. A. Choueiry, S. Zhang, A. Brehier, L. Largeau, O. Mauguin, J. Bloch, and E. Deleporte, "Optical spectroscopy of two-dimensional layered $(C_6H_5C_2H_4 - NH_3)_2 - PbI_4$ perovskite," *Opt. Express*, vol. 18, no. 6, pp. 5912–5919, Mar 2010.

[111] D. B. Straus, S. Hurtado Parra, N. Iotov, Q. Zhao, M. R. Gau, P. J. Carroll, J. M. Kikkawa, and C. R. Kagan, "Tailoring hot exciton dynamics in 2D hybrid perovskites through cation modification," *ACS Nano*, vol. 14, no. 3, pp. 3621–3629, 03 2020. [Online]. Available: https://doi.org/10.1021/acsnano.0c00037

[112] T. T. H. Do, A. Granados del Águila, D. Zhang, J. Xing, S. Liu, M. A. Prosnikov, W. Gao, K. Chang, P. C. M. Christianen, and Q. Xiong, "Bright exciton fine-structure in two-dimensional lead halide perovskites," *Nano Letters*, 05 2020. [Online]. Available: https://doi.org/10.1021/acs.nanolett.0c01364

[113] N. Kitazawa, M. Aono, and Y. Watanabe, "Temperature-dependent time-resolved photoluminescence of $(C_6H_5C_2H_4NH_3)_2PbX_4$ (X=Br and I)," *Materials Chemistry and Physics*, vol. 134, no. 2, pp. 875 – 880, 2012. [Online]. Available: http://www.sciencedirect.com/science/article/pii/S0254058412003331

[114] W. K. Chong, K. Thirumal, D. Giovanni, T. W. Goh, X. Liu, N. Mathews, S. Mhaisalkar, and T. C. Sum, "Dominant factors limiting the optical gain in layered two-dimensional halide perovskite thin films," *Phys. Chem. Chem. Phys.*, vol. 18, pp. 14 701–14 708, 2016. [Online]. Available: http://dx.doi.org/10.1039/C6CP01955B

[115] L. Gan, H. He, S. Li, J. Li, and Z. Ye, "Distinctive excitonic recombination in solution-processed layered organic–inorganic hybrid two-dimensional perovskites," *J. Mater. Chem. C*, vol. 4, pp. 10 198–10 204, 2016. [Online]. Available: http://dx.doi.org/10.1039/C6TC03408J

[116] T. Dammak, M. Koubaa, K. Boukheddaden, H. Bougzhala, A. Mlayah, and Y. Abid, "Two-dimensional excitons and photoluminescence properties of the organic/inorganic $(4 - FC_6H_4C_2H_4NH_3)_2[PbI_4]$ nanomaterial," *The Journal of Physical Chemistry C*, vol. 113, no. 44, pp. 19 305–19 309, 2009. [Online]. Available: https://doi.org/10.1021/jp9057934

[117] E. F. Schubert, E. O. Göbel, Y. Horikoshi, K. Ploog, and H. J. Queisser, "Alloy broadening in photoluminescence spectra of $Al_xGa_{1-x}As$," *Phys. Rev. B*, vol. 30, pp. 813–820, Jul 1984. [Online]. Available: https://link.aps.org/doi/10.1103/PhysRevB.30.813

[118] S. M. Lee and K. K. Bajaj, "A quantum statistical theory of linewidths of radiative transitions due to compositional disordering in semiconductor alloys," *Journal of Applied Physics*, vol. 73, no. 4, pp. 1788–1796, 1993. [Online]. Available: https://doi.org/10.1063/1.353215

[119] Q. Zhang, L. Chu, F. Zhou, W. Ji, and G. Eda, "Excitonic properties of chemically synthesized 2D organic–inorganic hybrid perovskite nanosheets," *Advanced Materials*, vol. 30, no. 18, p. 1704055, 2018. [Online]. Available: https://onlinelibrary.wiley.com/doi/abs/10.1002/adma.201704055

[120] C. Yu, Z. Chen, J. J. Wang, W. Pfenninger, N. Vockic, J. T. Kenney, and K. Shum, "Temperature dependence of the band gap of perovskite semiconductor compound $CsSnI_3$," *Journal of Applied Physics*, vol. 110, no. 6, p. 063526, 2011. [Online]. Available: https://doi.org/10.1063/1.3638699

[121] S. Wang, J. Ma, W. Li, J. Wang, H. Wang, H. Shen, J. Li, J. Wang, H. Luo, and D. Li, "Temperature-dependent band gap in two-dimensional perovskites: Thermal expansion interaction and electron–phonon interaction," *The Journal of Physical Chemistry Letters*, vol. 10, no. 10, pp. 2546–2553, 05 2019. [Online]. Available: https://doi.org/10.1021/acs.jpclett.9b01011

[122] K. Wei, Z. Xu, R. Chen, X. Zheng, X. Cheng, and T. Jiang, "Temperature-dependent excitonic photoluminescence excited by two-photon absorption in perovskite $CsPbBr_3$ quantum dots," *Opt. Lett.*, vol. 41, no. 16, pp. 3821–3824, 08 2016. [Online]. Available: http://ol.osa.org/abstract.cfm?URI=ol-41-16-3821

[123] J. Bhosale, A. K. Ramdas, A. Burger, A. Muñoz, A. H. Romero, M. Cardona, R. Lauck, and R. K. Kremer, "Temperature

dependence of band gaps in semiconductors: Electron-phonon interaction," *Phys. Rev. B*, vol. 86, p. 195208, 11 2012. [Online]. Available: https://link.aps.org/doi/10.1103/PhysRevB.86.195208

[124] K. Schötz, A. M. Askar, W. Peng, D. Seeberger, T. P. Gujar, M. Thelakkat, A. Köhler, S. Huettner, O. M. Bakr, K. Shankar, and F. Panzer, "Double peak emission in lead halide perovskites by self-absorption," *J. Mater. Chem. C*, vol. 8, pp. 2289–2300, 2020. [Online]. Available: http://dx.doi.org/10.1039/C9TC06251C

[125] H. Diab, C. Arnold, F. Lédée, G. Trippé-Allard, G. Delport, C. Vilar, F. Bretenaker, J. Barjon, J.-S. Lauret, E. Deleporte, and D. Garrot, "Impact of reabsorption on the emission spectra and recombination dynamics of hybrid perovskite single crystals," *The Journal of Physical Chemistry Letters*, vol. 8, no. 13, pp. 2977–2983, 2017, pMID: 28608691. [Online]. Available: https://doi.org/10.1021/acs.jpclett.7b00998

[126] R. Prasanna, A. Gold-Parker, T. Leijtens, B. Conings, A. Babayigit, H.-G. Boyen, M. F. Toney, and M. D. McGehee, "Band gap tuning via lattice contraction and octahedral tilting in perovskite materials for photovoltaics," *Journal of the American Chemical Society*, vol. 139, no. 32, pp. 11 117–11 124, 08 2017. [Online]. Available: https://doi.org/10.1021/jacs.7b04981

[127] Y. Zhang, R. Wang, Y. Li, Z. Wang, S. Hu, X. Yan, Y. Zhai, C. Zhang, and C. Sheng, "Optical properties of two-dimensional perovskite films of $(C_6H_5C_2H_4NH_3)_2[PbI_4]$ and $(C_6H_5C_2H_4NH_3)_2(CH_3NH_3)_2[Pb_3I_{10}]$," *The Journal of Physical Chemistry Letters*, vol. 10, no. 1, pp. 13–19, 2019. [Online]. Available: https://doi.org/10.1021/acs.jpclett.8b03458

[128] M. Baibarac, I. Smaranda, M. Scocioreanu, R. Mitran, M. Enculescu, M. Galatanu, and I. Baltog, "Exciton-phonon interaction in PbI_2 revealed by raman and photoluminescence studies using excitation light overlapping the fundamental absorption edge," *Materials Research Bulletin*, vol. 70, pp. 762–772, 2015. [Online]. Available: https://www.sciencedirect.com/science/article/pii/S0025540815003827

[129] M. A. Stevens, C. Silva, D. M. Russell, and R. H. Friend, "Exciton dissociation mechanisms in the polymeric semiconductors poly(9,9-dioctylfluorene) and poly(9,9-dioctylfluorene-co-benzothiadiazole)," *Phys. Rev. B*, vol. 63, p. 165213, Apr 2001. [Online]. Available: https://link.aps.org/doi/10.1103/PhysRevB.63.165213

[130] G. Delport, G. Chehade, F. Lédée, H. Diab, C. Milesi-Brault, G. Trippé-Allard, J. Even, J.-S. Lauret, E. Deleporte, and D. Garrot, "Exciton–exciton annihilation in two-dimensional halide perovskites at room temperature," *The Journal of Physical Chemistry Letters*, vol. 10, no. 17, pp. 5153–5159, 2019, pMID: 31415177. [Online]. Available: https://doi.org/10.1021/acs.jpclett.9b01595

[131] M. Gramlich, B. J. Bohn, Y. Tong, L. Polavarapu, J. Feldmann, and A. S. Urban, "Thickness-dependence of exciton–exciton annihilation in halide perovskite nanoplatelets," *The Journal of Physical Chemistry Letters*, vol. 11, no. 13, pp. 5361–5366, 2020, pMID: 32536167. [Online]. Available: https://doi.org/10.1021/acs.jpclett.0c01291

[132] A. Yangui, S. Pillet, A. Mlayah, A. Lusson, G. Bouchez, S. Triki, Y. Abid, and K. Boukheddaden, "Structural phase transition causing anomalous photoluminescence behavior in

perovskite $(C_6H_{11}NH_3)_2[PbI_4]$," *The Journal of Chemical Physics*, vol. 143, no. 22, p. 224201, 2015. [Online]. Available: https://doi.org/10.1063/1.4936776

[133] M. Kaiser, Y. Li, I. Allegro, B. S. Richards, U. W. Paetzold, and I. A. Howard, "Interpreting the time-resolved photoluminescence of quasi-2D perovskites," *Advanced Materials Interfaces*, vol. 8, no. 24, p. 2101326, 2021. [Online]. Available: https://onlinelibrary.wiley.com/doi/abs/10.1002/admi.202101326

[134] C. C. Stoumpos, D. H. Cao, D. J. Clark, J. Young, J. M. Rondinelli, J. I. Jang, J. T. Hupp, and M. G. Kanatzidis, "Ruddlesden–Popper hybrid lead iodide perovskite 2D homologous semiconductors," *Chemistry of Materials*, vol. 28, no. 8, pp. 2852–2867, 2016. [Online]. Available: https://doi.org/10.1021/acs.chemmater.6b00847

[135] J. Cho, J. T. DuBose, and P. V. Kamat, "Charge carrier recombination dynamics of two-dimensional lead halide perovskites," *The Journal of Physical Chemistry Letters*, vol. 11, no. 7, pp. 2570–2576, 2020, pMID: 32160471. [Online]. Available: https://doi.org/10.1021/acs.jpclett.0c00392

[136] P. Vashishtha, M. Ng, S. B. Shivarudraiah, and J. E. Halpert, "High efficiency blue and green light-emitting diodes using Ruddlesden–Popper inorganic mixed halide perovskites with butylammonium interlayers," *Chemistry of Materials*, vol. 31, no. 1, pp. 83–89, 2019. [Online]. Available: https://doi.org/10.1021/acs.chemmater.8b02999

[137] L. Xu, Y. Qiang, H. Hu, P. Lin, P. Wang, S. Che, H. Sun, Z. Nie, C. Cui, F. Wu, D. Yang, and X. Yu, "Effects of n-butyl amine incorporation on the performance of perovskite light emitting

diodes," *Nanotechnology*, vol. 30, no. 10, p. 105703, jan 2019. [Online]. Available: https://doi.org/10.1088/1361-6528/aaf68c

[138] Z. Xiao, R. A. Kerner, L. Zhao, N. L. Tran, K. M. Lee, T.-W. Koh, G. D. Scholes, and B. P. Rand, "Efficient perovskite light-emitting diodes featuring nanometre-sized crystallites," *Nature Photonics*, vol. 11, no. 2, pp. 108–115, Feb 2017. [Online]. Available: https://doi.org/10.1038/nphoton.2016.269

[139] F. Li, L. Yang, Z. Cai, K. Wei, F. Lin, J. You, T. Jiang, Y. Wang, and X. Chen, "Enhancing exciton binding energy and photoluminescence of formamidinium lead bromide by reducing its dimensions to 2D nanoplates for producing efficient light emitting diodes," *Nanoscale*, vol. 10, pp. 20611–20617, 2018. [Online]. Available: http://dx.doi.org/10.1039/C8NR04986F

[140] B. Chaudhary, T. M. Koh, B. Febriansyah, A. Bruno, N. Mathews, S. G. Mhaisalkar, and C. Soci, "Mixed-dimensional naphthylmethylammonium-methylammonium lead iodide perovskites with improved thermal stability," *Scientific Reports*, vol. 10, no. 1, p. 429, Jan 2020. [Online]. Available: https://doi.org/10.1038/s41598-019-57015-4

[141] C.-T. Lin, J. Lee, J. Kim, T. J. Macdonald, J. Ngiam, B. Xu, M. Daboczi, W. Xu, S. Pont, B. Park, H. Kang, J.-S. Kim, D. J. Payne, K. Lee, J. R. Durrant, and M. A. McLachlan, "Origin of open-circuit voltage enhancements in planar perovskite solar cells induced by addition of bulky organic cations," *Advanced Functional Materials*, vol. 30, no. 7, p. 1906763, 2020. [Online]. Available: https://onlinelibrary.wiley.com/doi/abs/10.1002/adfm.201906763

[142] J. Chang, S. Zhang, N. Wang, Y. Sun, Y. Wei, R. Li, C. Yi, J. Wang, and W. Huang, "Enhanced performance of red perovskite light-emitting diodes through the dimensional tailoring of perovskite multiple quantum wells," *The Journal of Physical Chemistry Letters*, vol. 9, no. 4, pp. 881–886, 2018, pMID: 29392948. [Online]. Available: https://doi.org/10.1021/acs.jpclett.7b03417

[143] I. Allegro, Y. Li, B. S. Richards, U. W. Paetzold, U. Lemmer, and I. A. Howard, "Bimolecular and auger recombination in phase-stable perovskite thin films from cryogenic to room temperature and their effect on the amplified spontaneous emission threshold," *The Journal of Physical Chemistry Letters*, vol. 12, no. 9, pp. 2293–2298, 2021, pMID: 33651626. [Online]. Available: https://doi.org/10.1021/acs.jpclett.1c00099

[144] V. Gulbinas, R. Jakubenas, S. Pakalnis, and A. Undzenas, "Dynamics of charge carrier precursor photogeneration in titanyl phthalocyanine," *The Journal of Chemical Physics*, vol. 107, no. 13, pp. 4927–4933, 1997. [Online]. Available: https://doi.org/10.1063/1.474856

[145] C. H. Lui, K. F. Mak, J. Shan, and T. F. Heinz, "Ultrafast photoluminescence from graphene," *Phys. Rev. Lett.*, vol. 105, p. 127404, Sep 2010. [Online]. Available: https://link.aps.org/doi/10.1103/PhysRevLett.105.127404

[146] D. Sun, G. Aivazian, A. M. Jones, J. S. Ross, W. Yao, D. Cobden, and X. Xu, "Ultrafast hot-carrier-dominated photocurrent in graphene," *Nature Nanotechnology*, vol. 7, no. 2, pp. 114–118, Feb 2012. [Online]. Available: https://doi.org/10.1038/nnano.2011.243

[147] R. Röder, T. P. H. Sidiropoulos, C. Tessarek, S. Christiansen, R. F. Oulton, and C. Ronning, "Ultrafast dynamics of lasing semiconductor nanowires," *Nano Letters*, vol. 15, no. 7, pp. 4637–4643, 2015, pMID: 26086355. [Online]. Available: https://doi.org/10.1021/acs.nanolett.5b01271

[148] S. Yu, Y. Yan, M. Abdellah, T. Pullerits, K. Zheng, and Z. Liang, "Nonconfinement structure revealed in Dion–Jacobson type quasi-2D perovskite expedites interlayer charge transport," *Small*, vol. 15, no. 49, p. 1905081, 2019. [Online]. Available: https://onlinelibrary.wiley.com/doi/abs/10.1002/smll.201905081

[149] S. Gharibzadeh, P. Fassl, I. M. Hossain, P. Rohrbeck, M. Frericks, M. Schmidt, T. Duong, M. R. Khan, T. Abzieher, B. A. Nejand, F. Schackmar, O. Almora, T. Feeney, R. Singh, D. Fuchs, U. Lemmer, J. P. Hofmann, S. A. L. Weber, and U. W. Paetzold, "Two birds with one stone: dual grain-boundary and interface passivation enables >22% efficient inverted methylammonium-free perovskite solar cells," *Energy Environ. Sci.*, vol. 14, pp. 5875–5893, 2021. [Online]. Available: http://dx.doi.org/10.1039/D1EE01508G

[150] A. Kaukher, "LED pulser: A light-emitting diode–based light source for 2D detectors," Tech. Rep., 2017.

[151] N. B. Hassan, F. Dehkhoda, E. Xie, J. Herrnsdorf, M. J. Strain, R. Henderson, and M. D. Dawson, "Ultra-high frame rate digital light projector using chipscale LED-on-CMOS technology," 2021. [Online]. Available: https://arxiv.org/abs/2111.13586http://dx.doi.org/10.48550/ARXIV.2111.13586

[152] M. R. Leyden, S. Terakawa, T. Matsushima, S. Ruan, K. Goushi, M. Auffray, A. S. D. Sandanayaka, C. Qin, F. Bencheikh, and

C. Adachi, "Distributed feedback lasers and light-emitting diodes using 1-naphthylmethylamnonium low-dimensional perovskite," *ACS Photonics*, vol. 6, no. 2, pp. 460–466, 2019. [Online]. Available: https://doi.org/10.1021/acsphotonics.8b01413